Development of an Apparatus for the Study of Electron Impact Fragmentation of Molecular Clusters

Gerard Thomas Barrett

A thesis submitted for the Degree of Masters of Science

NUI MAYNOOTH

Ollscoil na hÉireann Má Nuad

Department of Experimental Physics,
NUI Maynooth,
Maynooth,
Co. Kildare.

October 2008

Head of Department
Professor J. Anthony Murphy

Research Supervisor
Dr. Peter J. M van der Burgt

Contents

Abstract **i**

Acknowledgments **ii**

Chapter 1: Introduction and Background **1**

1.1 What are clusters, and why are they relevant? 1
1.2 Cluster research in general, a brief history 7
1.3 Rare Gas Clusters 8
1.4 Metal Clusters 10
1.5 Fullerenes 11
1.6 Methanol and Methanol Clusters 12
1.6.1 Introduction 12
1.6.2 Methanol Molecule 13
1.6.3 Methanol Clusters 16
1.7 Water and Water Clusters 20
1.7.1 Introduction 20
1.7.2 H_2O and Electron Impact 22
1.7.3 Water Clusters 27
1.8 DNA and Low Energy Electron (LEE) Interactions 32
1.8.1 Introduction 32
1.8.2 DNA 32
1.8.3 DNA Damage 35
1.8.4 Low Energy Electron studies involving DNA and its Bases 36
1.8.5 Water and Nucleic Acids 41
1.9 Research at Maynooth 44
1.10 References 46

Chapter 2: Clusters - Sources and Detection **52**

2.1 Generating Clusters 52

2.2 Supersonic Expansion 54
2.3 Fragmentation Products - Ions and Metastables 57
2.4 Ion Detection – Time-of-Flight Mass Spectrometry 58
2.5 Time-of-flight Detection of Neutral Metastable Fragments 60
2.6 References 62

Chapter 3: Experimental Apparatus 64

3.1 Overview of Setup 64
3.2 Expansion Chamber 66
3.3 Collision Chamber 68
3.4 Electron Gun and Deflection System 71
3.4.1 Electron Gun 71
3.4.2 Deflection System 72
3.5 Reflectron Time-of-Flight Region 74
3.5.1 Microchannel Plate Detection Efficiency 76
3.6 Neutral Metastable Detector 77
3.7 Amplification and Discrimination of Detection Signals 80
3.8 Modifications 81
3.9 References 83

Chapter 4: Interfacing, Data Acquisition and Analysis 84

4.1 Overview 84
4.2 Pulsing and Timing 86
4.3 Acquisition 88
4.4 Programmable Power Supply and DAQ Device 89
4.5 LabVIEW Data Acquisition Software 90
4.5.1 V_Inc_Cont.vi 92
4.5.2 Scan_Acq.vi - Page 2 94
4.5.3 Scan_Acq.vi - Page 1 96
4.6 Matlab Analysis 103

Chapter 5: Experimental Results **106**

5.1 Overview 106
5.2 Calibration of Multichannel Scaler 107
5.3 Multichannel Scaler Coincidence Test 108
5.4 Deflection Voltage Optimisation 109
5.5 Microchannel Plate Detection Rate Test 110
5.6 Electron Gun Tests 111
5.7 Deflection System Test 113
5.8 TOF Mass Spectrometer Calibration 114
5.9 Pulsed Valve Tests 116
5.10 Clustering vs. Pressure 121
5.11 Argon Mass Spectra and Excitation Functions 123
5.11.1 Mass Spectra 123
5.11.2 Excitation Functions 126
5.12 Argon Metastable TOF Spectra 129
5.13 Methanol Mass Spectra and Excitation Functions 132
5.13.1 Mass Spectra 132
5.13.2 Excitation Functions 135
5.14 References 137

Chapter 6: Conclusion **138**

APPENDIX A: Library Code for MCS **141**

APPENDIX B: LabVIEW Block Diagram "Scan_Acq.vi" **146**

APPENDIX C: LabVIEW Block Diagram "Binning.vi" **150**

APPENDIX D: Matlab Code **151**

Abstract

The aim of the experiment described in this thesis was to generate a beam of molecular clusters and to look at fragmentation processes induced by low-energy electron impact. These processes are studies by time-of-flight detection of ionised and neutral metastable fragments. A beam of molecular clusters is generated using a pulsed supersonic expansion, and this beam is crossed with a pulsed beam of electrons. The electron pulse is 1 μs to provide the necessary time-of-flight resolution. Ionised fragments are detected using a reflectron time-of-flight mass spectrometer with a microchannel plate detector. Neutral metastable fragments are detected using a channeltron with appropriately biased meshes in front to avoid the detection of charged particles. For both types of fragment data acquisition takes place using a multichannel scaler. Detection of the ions is mass resolved, whereas the flight time of the neutral metastable fragments provides information about the kinetic energy these fragments have acquired in the fragmentation process. The ultimate goal of this experiment is to study low-energy electron impact on biomolecules solvated in water clusters. This is relevant in the context of radiation damage studies. Recent research on radiation damage in biological organisms has demonstrated the relevance of low-energy secondary electrons produced by the radiation.

The work described in this thesis involved the development of a working cluster source, which produces excellent methanol and argon mass spectra, via supersonic expansion from a nozzle. A neutral metastable detector has been designed, constructed, and implemented; time-of-flight spectra have been gathered for electron impact on argon clusters, and are in agreement with previous work, indicating the detector is operating well. The electron gun has been adapted to incorporate a deflection system for steering of the electron beam, and now operates well with stability down to 20 eV. Programs have been written using LabVIEW for control of the electron impact energy, and for the acquisition of data and excitation functions, as well as providing quick analysis of mass spectra. Further minor modifications and implementations have been conducted to optimise the overall operation of the system. This developmental work has moved the apparatus at Maynooth closer to its ultimate goal, the study of electron impact fragmentation of molecular clusters.

Acknowledgements

My thanks goes to the members of the N.U.I.M experimental physics department who have all been so helpful to me over the course of my research, particularly; Professor Anthony Murphy, for use of the department's facilities, Grainne Roche, the red cross of the department, for providing help on everything from pay to home furnishing and lighting, John Kelly, for all things computer related, and for reminding me one time that my internet connection problem might be directly related to the cable being disconnected from the socket!, Pat Seery, for his electronics expertise, and for having to endure any singin… wailing from our office that could be heard from his (perhaps linked to his relocation to another floor), Marçin Gradziel, for his interfacing assistance, particular with regard to LabVIEW, and Dave Watson, for the enormous amount of work and engineering expertise he has put into helping develop the present cluster apparatus, without which little research would be possible. Also, a quick word of recognition to the many other postgrads I have known over these few years, they come and go, but undoubtedly they are the air that helps keep the department breathing; it has been great fun spending time and working with such a great and interesting bunch of people.

A special word of thanks goes to my supervisor Dr. Peter van der Burgt, for always being so helpful, insightful, and considerate to work with, for providing me with the opportunity to carry out this research in the first place, and for enduring and wading through, with great patience, endless sentences, which appeared infinite, meandering, and Joycean, particularly in the early drafts of this thesis, with some still to be found lurking about. I would also like to thank both him and the department for the opportunity to obtain a certificate in vacuum physics and techniques from the Université Catholique de Louvain.

I wish to thank Dr. Sean McCaffrey, of the chemistry department at Maynooth, and Prof. Andrew Murray, of the University of Manchester, for the loan and use of their equipment. I thank also the European Project HPRI-CT-2005-026015, in particular Dr. Bernd Huber (ITS-LEIF), for granting me transnational access and experience at the CEA-CIRIL ARIBE research facility. Finally, I thank Mayo County Council for providing me the financial support of a Higher Education Grant for the duration of my studies.

Special acknowledgement goes to my family; to my mother and father, Theresa and Michael, for always being so supportive, encouraging, and for reminding me that, no matter what the real or philosophical dilemma is, home is always there, with Tootsie and Willow waiting to be walked, flowers to be watered, or ducks to be fed, to my brother Michael, for being so frustratingly good at winding me up and keeping me grounded at times, to my sister Anita and her husband Brian, for being such a lovely couple and for always having an open door in their wonderful home (including the wonderful Benny and Georgie) whenever a break was required.

The penultimate acknowledgments are saved for my co-inhabitants of that little magical office crouched at the end of a corridor long. Working is a term that has to be applied loosely, especially under circumstances as enjoyable as when it is in the company of those whom I have shared that office with; Aoife, Chris and Jason (quake!). My time spent there is full of great memories, memories of debates, problem solving, fun, and momentous bouts of melodies being bandied and belted about spontaneously. In particular I wish to thank Chris for being a great friend and gentleman to work with, for always willingly giving his time up to help others, for his much appreciated sincerity and honesty on all issues, and of course for introducing me to breakfalls (turn your head).

Finally, I wish to thank my love Aoife, for bringing to me true happiness and the foresight that comes with it, foresight of a time when nostalgia will be but a memory itself, and memories an abundant pleasure.

CHAPTER 1

Introduction and Background

1.1 What are clusters, and why are they relevant?

A *cluster* is a particle unto itself that is formed from an assemblage of atoms, or molecules, or a composite such that the resultant is a stable entity; a cluster can be thought of as made of *n* building blocks of atoms and molecules with the size somewhere in the limits of $2 < n < 10^n$, where *n* can be as high as 6 or 7.[1] The size of a cluster is not specific but should be such that it is distinguishable from the upper (bulk) and lower (atomic/molecular) limits of existence. Two basic categories of cluster are defined by the terms *homo* and *hetero.* If we have a cluster X_n, such that $X_n = A_{n-m} + B_m$, and the atom/molecule type A = B, then the cluster is considered a homocluster i.e. Ar_n. Otherwise if A ≠ B then the cluster can be described as a heterocluster, as in the case of sodium chloride clusters Na_nCl_m. An example of each is shown in figure 1.[2,3]

HOMO

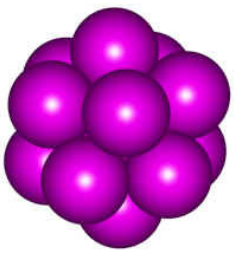

HETERO

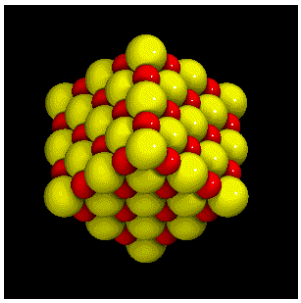

Figure 1: Homocluster Ar_{13} (left),[2] and heterocluster sodium chloride formation of salt (right).[3]

Clusters can be formed by almost every element available to us, from the strong ionic bonding elements (NaCl), to the inert rare gas elements (He, Ar). Because of the variety of elements we can classify the clusters in large part according to their bonding type. Table 1 shows a general classification.[4]

Type	Binding force	Example	Average Binding Energy
Ionic Clusters	Ionic Bonds Coulomb force Shell effects	$(NaCl)_n$ $(CaF_2)_n$	**2- 4 eV**
Metal clusters	Metallic bonds	$(Al)_n$ $(Cu)_n$	**0.5 – 3 eV**
Semiconductor clusters	Covalent bonds	$(GaAs)_n$ C_n	**1 – 4 eV**
Molecular clusters	Dispersive electrostatic(weak valence)	Organics $(I_2)_n$	**0.3 – 1 eV**
Hydrogen bonded clusters	H-bonded electrostatic charge transfer	$(H_2O)_n$ $(HF)_n$	**.3-0.5 eV**
Van der Waals Clusters	Dispersive plus weak electrostatic	Rare gases $(CO_2)_n$	**< 0.3 eV**

Table 1: Classification of cluster types and relevant bonds.[4]

In general the forces that occur in the corresponding bulk are similar to those exhibited in the smaller scale clusters. Ionic clusters are held by the strong coulomb interactions between oppositely charged ions. Semiconductor, metal, or valence-bonded clusters are bound as their constituents are in bulk, but display unique characteristics; valence electrons are free to roam about on the cluster as a whole and can contribute substantially to the properties of a cluster. Because clusters are in fact mostly surface, a closely packed cluster of 20 atoms may have only one atom in its interior.[5] It is covalent bonding that is responsible for the carbon based cluster known as a fullerene, a spherically shaped structure of 60 atoms. Hydrogen bonded clusters are relatively weakly bound compared with the above cluster types, however it is a critical force; the hydrogen bond sustains life in its gelling together of water into clusters or liquid. This in turn plays a critical role in the arrangement and behaviour of DNA within biological systems like the human body. The weakest bonding occurs in forming rare gas clusters such as Ar_n via the Van der Waals force. The effect of this force has also been noticed in small metal clusters before metallic binding becomes dominant.[6] In rare gas atoms the shell structure is complete; forces arise due to time averaged vibrations of the centre of the electron shell charge density with respect to the nucleus, creating a dipole moment that can be attracted to a neighbouring one, hence the presence and weakness of Van der Waals interactions.

Understanding the nature of what a cluster is, what makes it so unique and so varied at the same time, is best understood by a simple analogy that exhibits the importance of size dependence on physical characteristics, and hence highlights why clusters are a relevant topic of research.

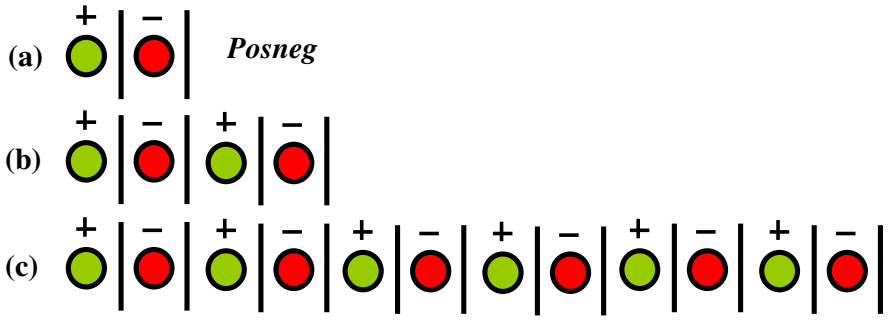

Figure 2: Posneg model exhibiting size dependence characteristics in analogy to cluster size dependence.

Imagine the system in figure 2 (a), which shows the basic building block: two identical particles of opposite charge that are held apart by some repulsive barrier, which we call a "Posneg". The energy required to remove a charge from either side is that of the Coulomb potential for two oppositely charged particles. If we add another Posneg such that it is constrained to exist in the same line as the existing Posneg and again try to remove a positive charge from the left side of (b) we will find it slightly easier due to an added coulomb repulsion (second positive charge) that is stronger than an added attractive negative charge, both to the right. Now what if we continue adding Posnegs and building our Posneg cluster past (c) until it is 10^5 blocks long? At that point, by adding another Posneg, the energy required to remove an end charge will indeed reduce but it will be so small a reduction that it is beyond the realms of detection, and hence we have moved into a bulk material state where the characteristics are size independent. This analogy outlines how the characteristics of a real cluster (i.e. ionic) could vary and progress from atom to bulk. It is often a goal in cluster physic research to find where it is appropriate to use solid-state theory and not some intermediary theory. Imagine we needed a Posneg based material that we can only ionise by laser at some energy above the ionisation potential of bulk Posneg: we could layer clusters of Posneg of the right size into a latticed structure and our problem would be solved. If only experiment were so straightforward. However, as a practical example of how substitution of clusters, rather than their atomic equivalent, can be used to astounding effect we can look at some modern research on magnetic clusters.[7] By applying a magnetic field to bulk magnetic metals such as iron or nickel the resistance can be changed by ~1%. Research has shown that by embedding Co clusters in Ag or Fe/Cr multilayers this effect, known as Giant Magnetoresistance (GMR), can be as high as 20% for Co in Ag, and 50% for Co in Fe/Cr. This is an incredible result considering it all comes down to the size of the clusters embedded, and can be attributed to the magnetic moment of clusters used being size dependant.

Clusters are relevant both because of their own intrinsic properties and because of their position as the link between solid-state physics and gas-phase atomic physics, or between condensed matter science and molecular science. They cover a wide range of sizes, from atomic to the crystalline, and indeed constitute a new type of particle - the nanoparticle (as when dealing with carbon clusters). They can exhibit unique characteristics, distinct from those found in bulk or discrete matter, characteristics that are as wide and varied as the size and mixture of clusters we can produce. It has become so vast a research field that cluster physics is now thought of as a subject itself within atomic and molecular physics research. Here is a brief outline of some of the merits it has as a research field:

1. It can aid us discover to what extent cluster properties resemble those of infinite solids, because clusters are systems in which many-body effects, forces and behaviour, can be observed and tested.

2. Clusters can be used to observe and study thermodynamic laws and phase transitions in nanoscale systems, teaching us whether or not they are the same as those observed in bulk.

3. Clusters can be easily produced in laboratories using wide variety of methods, see chapter 2, with cluster size, type and even shape in certain cases often controllable.[8,9,10,11] This implies more creative freedom for researchers in producing very specific, even exotic particles to study.

4. For theoreticians the use of clusters as an aid in understanding nucleation at an atomistic level has been a driving force.[12,13] This task has proved more complex than initially expected, yet with processing capabilities ever increasing the work continues, although now the clusters are treated not as the critical nucleus, but instead as an environment in which nucleation can occur on fast time scales.[14]

5. In the chemical industry the potential for developing better and indeed superior catalysts has provided the impetus for cluster research. Small metal particles and clusters can provide a large surface to volume ratio along with selectivity and activity properties that have been tailored to catalyse a specific reaction.[15,16]

6. Finally, with advancements in nano-technology, semiconductor cluster devices fabricated on the same scale could be the dream materials for altering the optical and electronic behaviour of the device to have very specific properties.

For all the above merits cluster physics more than justifies its existence as a worthwhile and beneficial research field by atomic and molecular physicists, chemists, molecular biologists, nuclear physicists, theoreticians, plasma physicists and astrophysicists.

In the remainder of this chapter I will first present a brief history of cluster research in section 1.2, followed by short sections on each of the following area's where there have been prominent findings: section 1.3 - rare gas clusters, section 1.4 - metal clusters, and section 1.5 - fullerenes. Then there will be a more substantial section involving work conduct on methanol and methanol clusters, section 1.6. In section 1.7 water and water clusters will be discussed, followed by a section describing DNA and low energy electron interactions, including nucleobase clusters and nucleobases embedded in water clusters, section 1.8. I will conclude the chapter with a brief description of the work conducted as part of this thesis, as well as an overview of the remaining content within the thesis itself.

1.2 Cluster research in general, a brief history

Perhaps the earliest reference to clusters was made as far back as 1661, "*minute masses or clusters…as were not easily dissipable into such particles as composed them*", by the great Irish scientist Robert Boyle.[17] Actual research and study on the topic itself began a couple of hundred years later in colloidal chemistry during the 1850's. Clusters produced in these experimental methods were suspended on layers of other materials, as opposed to many modern studies of isolated clusters produced in molecular beams. Famously, Faraday investigated the optical properties of gold colloids back in 1856 "*In this manner the leaf [gold] may be obtained so thin, that I think 50 or even 100 [atomic layers] might be included in a single progressive undulation of light*".[18] The influence of cluster size on physical characteristics was unclear at the time. Lord Kelvin posed the following question in 1871 "*Does the melting temperature of a small particle depend on it size?*". Verification did not come until 1976, when Buffat and Borel used a transmission electron microscope, to study gold clusters, and discovered, as was theoretically predicted, that melting temperature reduced with cluster size (figure 3).[1]

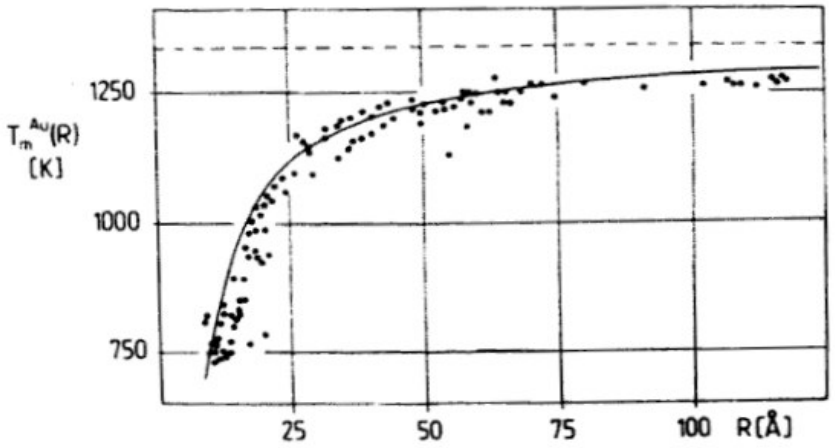

Figure 3: Melting point of gold clusters as function of temperature.[1]

Evidence of cluster formation first came in 1953 through work conducted on alkali halide beams by Ochs *et al*,[19] which reported dimmers forming in the beam generated from an effusive source. Even at this point clusters were not being generated solely for their own value. Two years previously Kantrowitz and Grey[20] proposed the use of a supersonic expansion technique, also used in this work, to improve molecular beam

intensities over the effusive method. Another five years would pass before Becker *et al*[21] discovered that this method was unfortunately leading to condensation in the beam jets formed - this condensation of course being cluster formation. This was to prove an immense leap for cluster science, an advent, as now intense sources for cluster beams were available to allow the study of all manner of clusters. From the 1960's onward to the present the field has grown continuously, such that a general review from this point on is beyond scope, and only several more prominent findings are discussed in the following sections.

1.3 Rare Gas Clusters

Work on rare gas clusters in the 1980's has led to the concept of magic numbers. For rare gas clusters of particular size *n*, as can be observed from the spectra in figure 4,[1] a magic number indicates higher stability of the cluster, evident in a greater ion yield in the mass spectrum. The strongest magic numbers generally exist at n = 13, 19, 25, 55, 71, 87, 147.

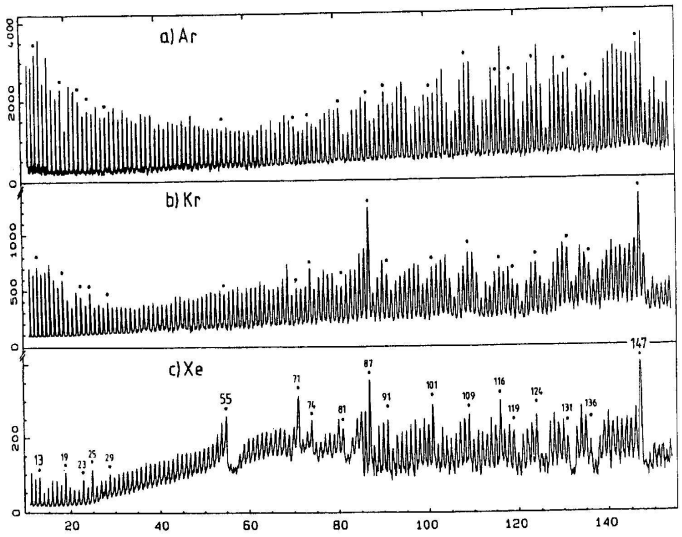

Figure 4: Mass spectra of Ar, Kr, and Xe, displaying the rare gas cluster magic numbers.[1]

It was Echt and co-workers (1981)[22] who first successfully applied a mass analysis technique to Xenon revealing magic number structures. Subsequently, similar work carried out by Miehle *et al*,[23] revealed the magic numbers of Ar and Kr also. Theory and simulation have shown best agreement to be found for rare gas cluster structures composed of icosahedral shells as in figure 1.[1]

Photon impact studies have been carried out on rare gas clusters revealing the excitation levels in argon clusters,[24] as well as photoionisation thresholds for Ar, Kr, and Xe clusters for a range of sizes.[25] These studies highlight the approach to bulk properties with increasing cluster size.

Electron impact studies have been used to observe the excitation of atoms on the surface and inside Ar and Kr clusters, using electron energy-loss spectroscopy.[26] Excitation processes have been identified via electron impact induced fluorescence for Ar and Kr clusters.[27,28] Neutral metastable fragments have also been examined for both Ar, Xe and Xe clusters[29,30] providing information on the electron impact fragmentation processes involved.

1.4 Metal Clusters

Knight and colleagues,[31] on work conducted on alkali clusters in the 1980's, discovered periodic patterns in their mass spectra. The nuclearities corresponding to these peaks were similarly termed "magic numbers" however their existence at n = 2, 8, 20, 40, 58 (figure 5) led to the necessity for a different model to describe them, called the Jellium model. Many variations on the model have since developed, spherical, ab initio, and empirical. In essence one assumes that the outer electrons of the metal atoms are loosely bound so that when a cluster is formed, they can move around everywhere within it, and are not bound to a particular atom. The atoms without their outer electrons are positively charged ions and form the attractive ionic core of the cluster. The free electrons "see" a jellium of positive ions in the cluster and form electronic shells. It is closed shell configurations that are responsible for the magic numbers observed in the mass spectra.

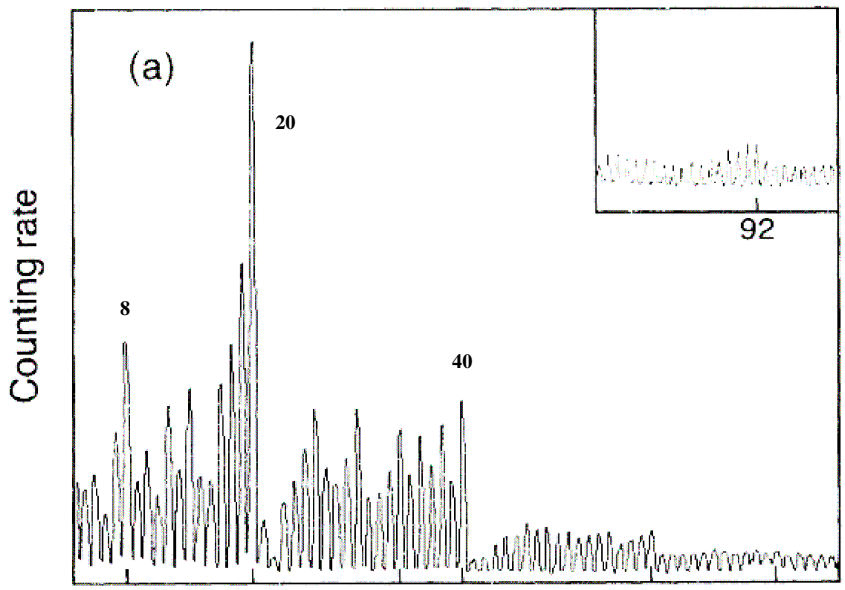

Figure 5: Magic numbers observed by Knight *et al* for sodium clusters.[31]

1.5 Fullerenes

The term fullerene is used to refer to a family of molecular structures made entirely of carbon, including spheres, tubes and planar sheets. In 1985 Kroto and his colleagues discovered buckminsterfullerene, $C_{60,}$ and continued by generating a whole series of "magically" stable clusters.[32] C_{60} is ultra-stable and composed of 60 carbon atoms arranged in pentagons and hexagons-like a football. Its name came from its form appearing like a geodesic dome, figure 6,[33] resembling the architecture of R. Buckminster Fuller.

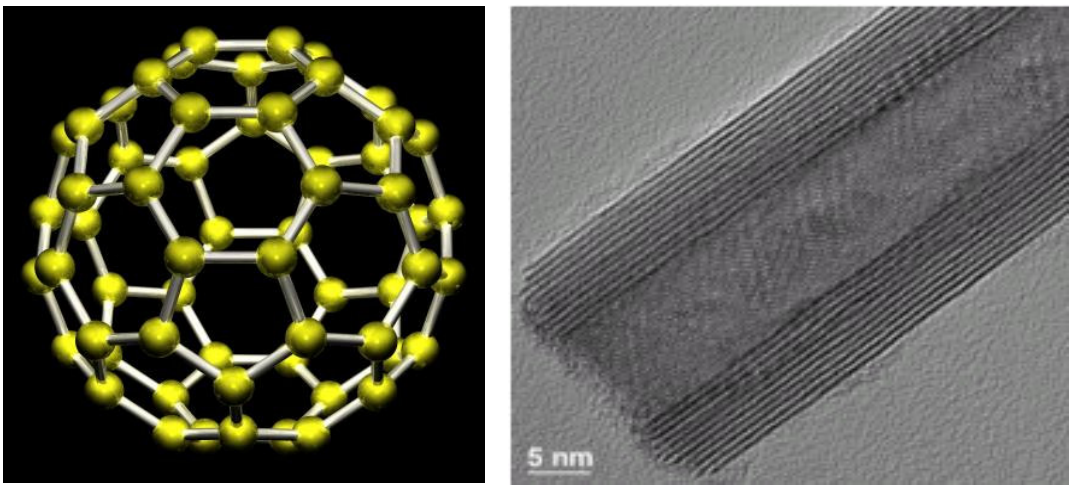

Figure 6: Left - Buckminsterfullerene illustration.[33] Right – High resolution TEM image of a fabricated nanotube.[35]

In 1991 Iijima[34] accidentally fabricated nanotubes that are composed of nested cylindrical carbon tubular structures with a hollow inside, capped at both ends by hemi-fullerenes. They were between 100 nm and several microns. Because of the great stability of these nanotubes, figure 6 (right),[35] the potential uses are enormous - tips for scanning probe microscopes, molecular wires by incorporation of silver or gold atoms, a replacement for conventional carbon fibre materials being more lightweight and flexible, and even in the biomedical industry as potential time release capsules for biomolecules.

1.6 Methanol and Methanol Clusters

1.6.1 Introduction

Methanol is an alcohol sometimes referred to as methyl alcohol. It is widely used in industry and science as a solvent and also as a fuel type.

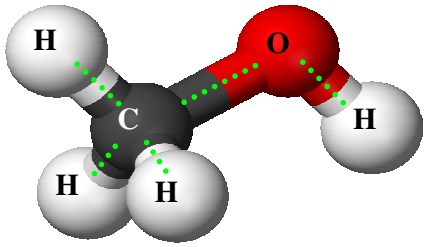

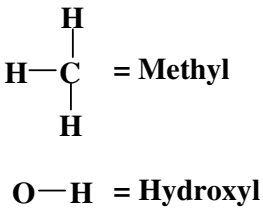

Figure 7: Methanol molecule and arrangement.

Alcohol is a chemical term used to refer to any organic molecule, in which a carbon atom, of one base group mixture of hydrogen/carbon atoms, is bonded to another group, a Hydroxyl group (-OH). Organic compounds satisfying this criterion obey a general molecular formula $C_nH_{2n+1}OH$. Methanol, CH_3OH, is the alcohol with the simplest molecular structure (figure 7), making it also the simplest "primary" alcohol, (primary denoting the number of carbon bonds, existent in the molecule). For this reason it is a suitable and elementary, if not ideal, substitute molecule in the study of how high-energy and low-energy electrons and photons might interact with more complex organic compounds, for example DNA, in the human body or other biological systems, by extension.

Methanol is also one of the smallest molecules to display amphiphillic behaviour. This means it comprises both hydrophobic and hydrophilic groups within the same molecule, respectively CH_3 and OH. The effect of this becomes evident when it is placed in solution; it self-organises inhomogeneously in order to minimise hydrophobic group contact with water where possible.[36] Methanol molecules will group together with the hydroxyl groups at the exterior of the arrangement, in essence shielding the inner hydrophobic groups. Protein folding is believed to have a strong dependency on the hydrophobic nature of DNA in water, and again in this sense studies and simulations involving methanol provide a starting point for treating the more complex helix.

1.6.2 Methanol Molecule

In a large number of experiments methanol has been studied as extensively as any other organic molecules by looking at a wide range of physical properties. Work had been carried out on measuring appearance potentials for ionic fragments as early as 1940, and by building upon this over the next half century we now have total and partial ionisation cross sections (figure 8) for electron impact ionisation of methanol in the region from threshold to 200eV.[37,38,39]

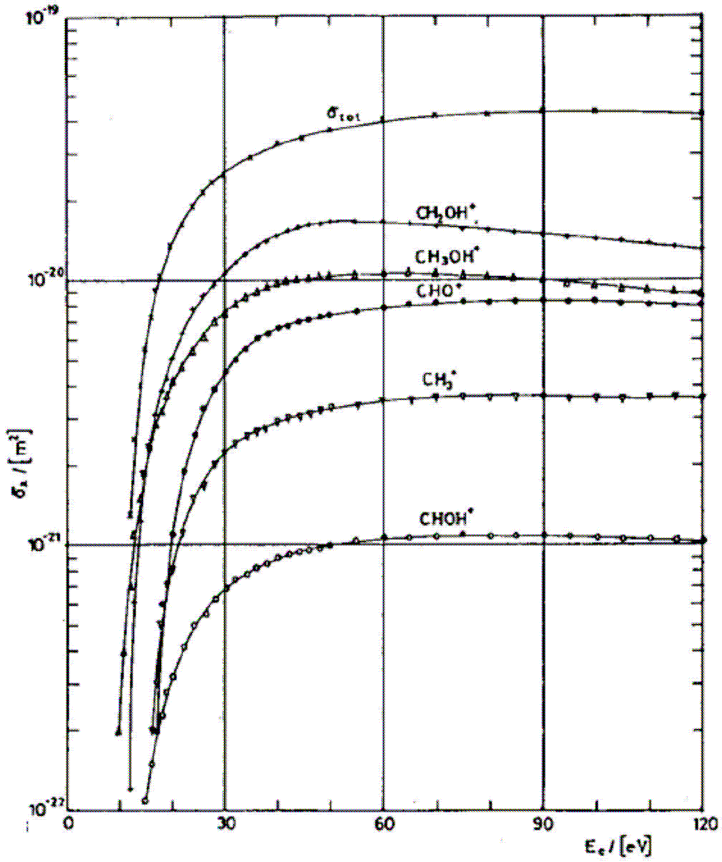

Figure 8: Total and partial electron impact ionisation curves for methanol producing the relevant ionic species.[37]

Some early work from the 1970s relied on electron impact as the interaction process with the molecule.[40,41,42,43] These studies on organic molecules and alcohols, including methanol and closely related methane CH_4, provide detailed information on the dissociative thresholds, pathways and processes of the molecule, following excitation/ionisation from low to middle energy electron (2000eV) impact. During this

period the binding energies of the electrons in various molecular orbits were being determined using photoelectron spectroscopic methods by numerous authors and can be found reviewed by von Niessen *et al.*[44] Accepted values for these binding energies are provided in table 2 below.

Binding energy in eV	Molecular orbital		
10.846 ±0.002	O	(p)	nonbonding
12.7	O–H	(p–s)	nonbonding
15.1	C–O	(p–p)	σ bonding
15.6	CH_3	(p)	π bonding
17.,6	CH_3	(p)	π' bonding
22.7	CH_3	(p)	σ bonding
32.2	O–H	C–O	σ

Table 2: Molecular orbits and binding energies for methanol.[37]

The process known as dissociative electron attachment (DEA) is another focal point of much molecular physics research. DEA is a process whereby a low energy electron is captured forming a *shape* or a *Feshbach* resonance. A resonance is a short-lived negative ion state that exists for longer than it would take the incident electron to pass through a particular target. A shape resonance occurs when an electron is captured into an intermediate state that lies energetically just above that of the original target atom or molecule, without any change to the original target configuration. Shape refers to the potential that traps the electron being dependent on the incident electron's angular momentum (*p*, *d*, *f*, etc). This penetrable barrier holds the electron near the target, yet allows the resonance to decay back to the initial target state plus a free electron, in general a quicker decay channel than is allowed for a Feshbach resonance. A Feshbach resonance occurs when an incident electron, in becoming captured, distorts the original target configuration, creating a potential well deep enough for that temporary capture. This bound state lies below that of the parent, and lasts longer than a shape resonance by virtue of the direct decay channel to the parent being closed.

The study of DEA to methanol has demonstrated three low-energy attachment processes that peak around 6.5, 8.0 and 10.5 eV.[45] These maxima can be attributed to Feshbach resonances with a double occupation of a *3s* Rydberg-like orbital, and they lead to

fragmentation of the molecule into a variety of possible ions. This was shown (figure 9) by comparison of the DEA spectrum with the photoelectron spectrum of methanol.[45] Modelling using R-matrix methods to calculate elastic collision and inelastic electronic excitation cross sections show close agreement.[46] More recently lower energy resonances have been observed around 3eV and are believed to be shape resonances.[47]

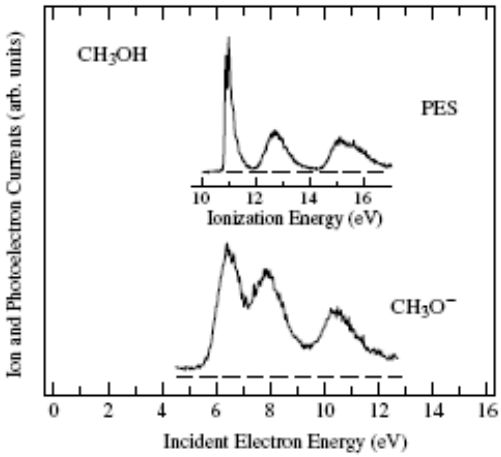

Figure 9: Comparison of the photoelectron spectrum and the DEA spectrum in methanol.[45]

Interesting work involving DEA by Prabhudesai *et al*[48] on organic molecules, including methanol, has shown that by fine-tuning the electron impact energy to respective resonant attachment energies it is possible to split the molecule at selective locations. In other words the resonance energies are group, not molecule, dependent. If we have a DEA peak, corresponding to a hydroxyl group, and evident by the formation of H^-, this peak should be apparent at very similar energy for any alcohol independent of the other groups attached. The extent to which this is true remains to be tested.

1.6.3 Methanol Clusters

Generation of methanol clusters has largely been performed via supersonic expansion from a nozzle, although other newer novel methods are being explored, such as evaporation of clusters from a frozen aqueous solution by infrared optical resonant desorption.[49] Often the target molecule is seeded in a carrier gas, helium or argon, which provides an aid to cluster formation (chapter 2). This technique has been used to form both neat, $(CH_3OH)_n$,[50,51,52,53,54] and mixed, $Ar_m(CH_3OH)_n$,[55,56] clusters. In order to study the clusters formed, or the clustering process, we require a method of detecting those clusters and distinguishing them from each other, perhaps by size, kinetic energy or structure. The most common methods for doing this involve ionising the cluster, either through electron impact ionisation (EI),[53,55] or photo-ionisation (PI),[50,51,52,56] (multi or single photon). These studies have shown that protonated methanol clusters, $(CH_3OH)H^+_n$ dominate the mass spectra. Unprotonated methanol clusters, ($n \leq 7$), have only been observed in an argon/methanol mixed cluster expansion.[49]

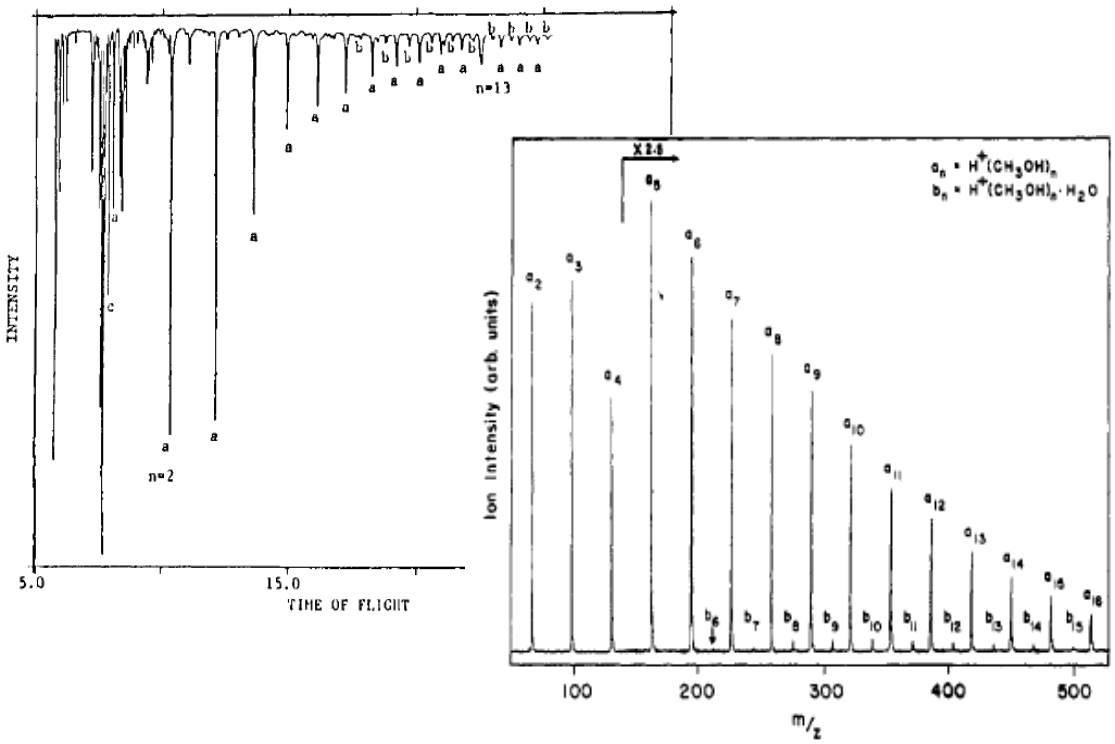

Figure 10: Methanol cluster spectra obtained by multi-photon ionisation (left),[51] and electron impact ionisation (right).[53]

Figure 10 displays mass spectra taken by multiphoton ionisation (*left*), and electron impact ionisation (*right*). Two series of peaks are evident conveniently labelled *a* and *b* in both. The more dominant **a** series is that of protonated methanol, $(CH_3OH)H^+_n$, while the less dominant **b** series, ($n \geq 7$), is attributed to $(H_2O)(CH_3OH)H^+_n$,. Daughter protonated methanol clusters are also produced and evident upon choosing suitable reflectron settings.[51] The reactions involved are the following:

$$(CH_3OH)_n + e^- \rightarrow [(CH_3OH)^+_n]^* + e^-$$
$$[(CH_3OH)^+_n]^* \rightarrow (CH_3OH)_{n-1}\ H^+ + CH_3O$$

This is the rapid internal ion-molecule reaction that produces the protonated clusters.[51] Subsequent daughter ions are produced later by,

$$(CH_3OH)_{n-1}\ H^+ \rightarrow (CH_3OH)_{n-2}\ H^+ + CH_3OH$$

The mechanism for protonated hydrated methanol is believed to be,[51]

$$(CH_3OH)_nH^+ \rightarrow (CH_3OH)_{n-2}(H_2O)H^+ + (CH_3)_2O$$

The above reaction does not occur in the photo-ionisation study,[52] possibly because the 26.5eV photons used, upon ionisation, impart any excess energy to the released electron, and not to the cluster where it is needed for the above reaction to occur. Other weaker dissociation pathways found for neat methanol have been listed by Morgan *et al*.[51]

The only evidence for unprotonated methanol clusters, ($n \leq 7$), has been observed for mixed argon/methanol clusters, wherein the electron impact energy is sufficiently low (17eV).[55] Vaidyanathan *et al* credit this behaviour to intra-cluster Penning ionisation wherein an excited state of the component with higher ionisation potential mediates the ionisation of the other component of lower ionisation potential. This can then be followed by further dissociation,

$$Ar_m(CH_3OH)_n + e^- \rightarrow Ar_m^*(CH_3OH)_n + e^-$$

$$Ar_m^*(CH_3OH)_n \rightarrow Ar_m(CH_3OH)_n^+ + e^-$$

$$Ar_m(CH_3OH)_n^+ \rightarrow Ar_m + (CH_3OH)_n^+$$

Mixed methanol and water clusters have been studied using femtosecond laser pump-probe techniques. Wisniewski *et al*[56] present evidence for the transient formation of H_3O-methanol clusters succeeding excitation of the parent cluster. This equates to hydrogen transfer within the cluster.

Finally, while the above studies provide information regarding, size, electronic structure, formation and reactions, they do not provide any direct method for understanding the geometric structures involved. Recently, suitable molecular dynamics simulations, coupled with C1*s* photoelectron spectroscopy of methanol clusters produced in a supersonic expansion, have provided information on the structures involved.[54,57,58] This technique has demonstrated how two regimes of methanol clusters are produced dependent on the backing pressure: the smaller size regime corresponds to oligomers, predominantly of cyclic structure (figure 11 *(left)*), the larger size regime is the result of clusters consisting of hundreds of molecules. Further use of this technique has revealed the ability to distinguish between hydrogen bonding and weaker electrostatic interactions as well as revealing information about the surface structure of methanol clusters.[54]

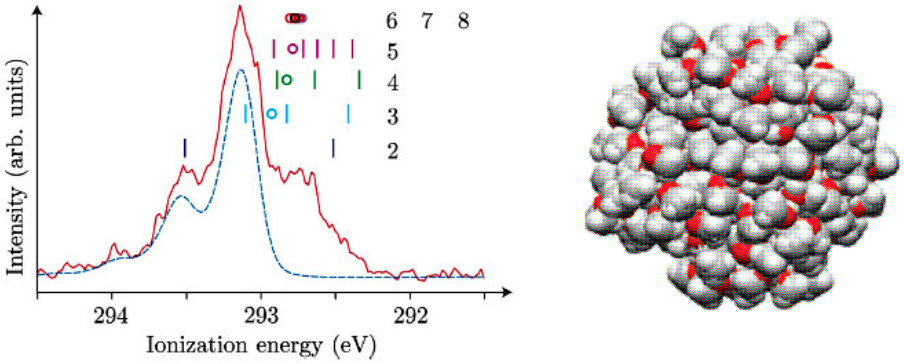

Figure 11: Left - C 1s X-ray photoelectron spectroscopy of methanol clusters. The dashed line shows the intensity that relates to ionization of free monomers. The difference between the experimental data points, solid line, and the dashed line corresponds to ionization of monomers in a cluster. The bars represent the ionization potential of linear oligomers and rings represent the ionization potential of cyclic oligomers. The number to the right indicates the number of monomers in each oligomer.[54] Right: Snapshot of the molecular dynamics simulation[57] of a methanol cluster n=20.

Recent progress in computation has made it possible to successfully model the behaviour of liquid methanol with regard to its electronic and structural properties.[59,60,61,62] A consequence of this is the suggestion, by comparison of experimental results with DFT (density functional theory) calculations, that liquid methanol comprises combinations of rings and chains of methanol molecules linked via hydrogen bonds. Sizes are believed to be dominated by n = 6 - 8 molecules.[60,61,62]

Research conducted on methanol by Baratta *et al*[63] has also examined how methanol, and other frozen species found in space, can be affected differently by similar energy doses from fast ions (30 keV) or UV photons (10.2 eV). They show how the optical property of the ice plays an active role in how it reacts to being irradiated. Initially when irradiated both optical and ion processes have similar effects, however as the ice begins to melt locally its optical properties change and hence the differences grow between the damage caused by fast ions and UV photons.

1.7 Water and Water Clusters

1.7.1 Introduction

Water certainly sustains almost every form of life we can observe. In the human body water cradles the helix of DNA that provides the blueprint for our form and function. For these reasons, of all the elements water holds a particular interest to humans, with the range of work by scientist over the centuries broad beyond recount in this thesis. A substantial and insightful introductory account can be found in "*H_2O: The biography of water*" by Phillip Ball. [64]

The building block of water is H_2O. It comprises of two hydrogen atoms bound to a single oxygen atom almost 16 times heavier, by covalent bonding (figure 12). In liquid water hydrogen bonds though much weaker than ionic or covalent bonds are responsible for holding the water molecules to each other, and though considered stable in water, on shorter time scales (< millisecond), the molecules are continuously fragmenting; the hydrogen atom breaking its bond and being exchanged between other H_2O molecules due to endothermic (energy absorbing) processes (protonation).[65]

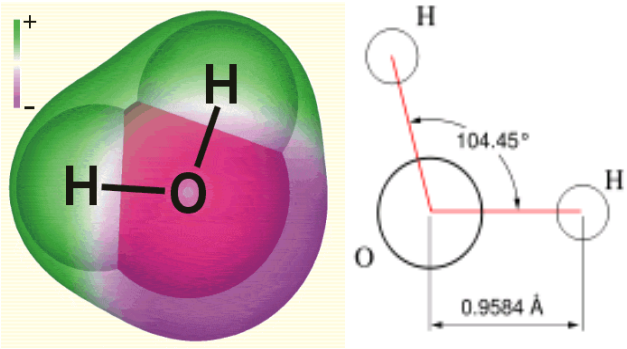

Figure 12: Shape and charge distribution of H_2O.[65]

The molecule has five electron pairs: the 1s pair, which stays tight to the oxygen, two pairs which form outer orbits of the oxygen, and the remaining two pairs that form the covalent bonding with hydrogen. This bonding is commonly represented as a tetrahedral arrangement of these outer pairs and it is the charge density of this arrangement that is generally believed to lead to its bent shape. Experimental values

commonly applied to water molecule are O-H length between 0.95718 Å and 1.0 Å, and H-O-H angle 104-109° as these factors are subject to environment.[65]

The subsequent sections will, because the subject scope is so large, only look at areas of particular relevance to this thesis, water and electron impact, and water clusters, without mention of liquid water. By liquid water I mean everyday bulk flowing water, filtered down to nothing but a sea of H_2O molecules in interaction with one another. There are extensive reviews on the subject, the most recent to my knowledge that of Phillip Ball,[66] which provides a good overview of our current understanding of water, with particular emphasis on its function in cell biology. Another all encompassing library of water related data and interpretation can be found on Martin Chaplin's website *www.lsbu.ac.uk/water/.html*. It is quite broad in content, but comprehensive, extremely well sourced and regularly updated.

1.7.2 H_2O and Electron Impact

Understanding the effect of electron collisions with water is of biological importance from the aspect of radiation damage to biological tissues. When water is irradiated and consequently ionised, the electrons ejected can have enough kinetic energy to ionise other water molecules creating stable molecules (H_2, O_2), free radicals (H, OH) and ion species, including further low energy electrons. To understand the damage that radiation can inflict on cells, and even DNA, we must recognise that water is undoubtedly a prime factor, and the influence of secondary electrons on water molecules needs to be comprehended. Itikawa and Mason[67] have provided a compilation of cross sections for electron collisions with water, along with recommendation on which of the studies conducted should be used. Of particular interest to us are the processes of ionisation and dissociative attachment upon electron impact.

The ionisation energy of H_2O is,[67]

$$E_i = 12.621\ (\pm 0.002)\ eV$$

The dissociative energy is,[67]

$$E_d = 5.099\ (\pm 0.003)\ eV$$

The various possibilities upon collision of an electron with H_2O are as follows:

(A) The electron has not enough energy to ionise the molecule (< 12.6 eV) and is scattered elastically or in-elastically (rotational energy absorption) from it. In 2003 Cho *et al*[68] performed experiments and calculated the differential cross section (DCS) at four electron impact energies 4, 15, 40 and 50 eV, and over a range of scattering angles 10^O-180^O. Faure *et al*[69] found good comparison with theoretical calculations of the DCS they performed at 4eV (figure 15). They did not calculate the DCS for 15eV because of ionisation effects, however they have calculated DCS for < 1 eV impact energies.

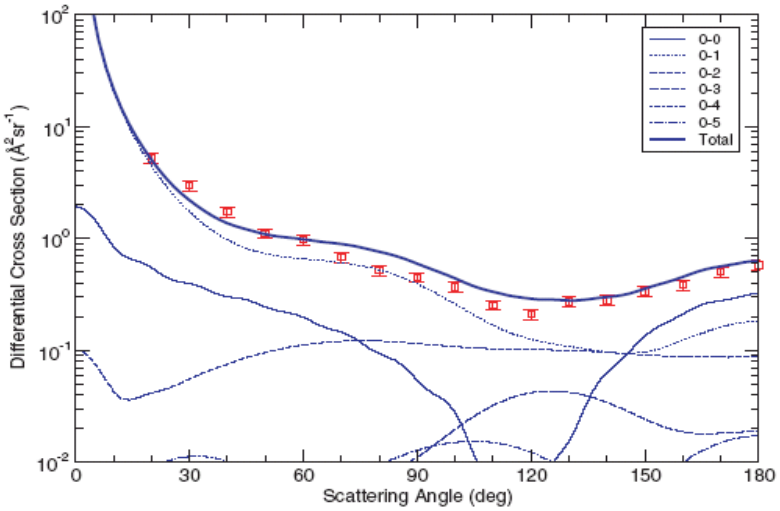

Figure 13: Faure et al[69] - theoretical calculation of DCS at 4eV energy, compared with work of Cho (squares). Black line is full DCS.

Another possibility in this energy regime is attachment of the electron leading to subsequent dissociation. This results in subsequent dissociative fragmentation in the form of anions, H^-, O^-, OH^-. Recommended cross section values are shown in figure 14. Three peaks corresponding to Feshbach resonances are evident at 6.5, 8.5 and 12 eV.[67]

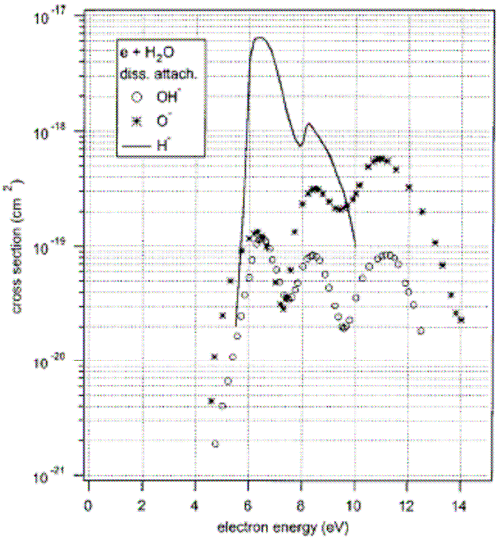

Figure 14: Electron attachment cross section of H_2O for the production of relevant anions.[67]

(B) The electron energy is greater than the threshold (12.6 eV) and therefore ionises the molecule leaving H_2O^+, which can subsequently dissociate. This occurs through the following decay channels (with the appearance potential included),

(I) $H_2O^+ \rightarrow H^+ + HO$, (16.95 eV)

(II) $H_2O^+ \rightarrow H_2^+ + O$, (20.7 eV)

(III) $H_2O^+ \rightarrow H + OH^+$, (18.116 eV)

(IV) $H_2O^+ \rightarrow H_2 + O^+$, (19.0 eV)

Itikawa *et al* recommend the ionisation cross-sections of Straub *et al*,[70] shown in figure 15.

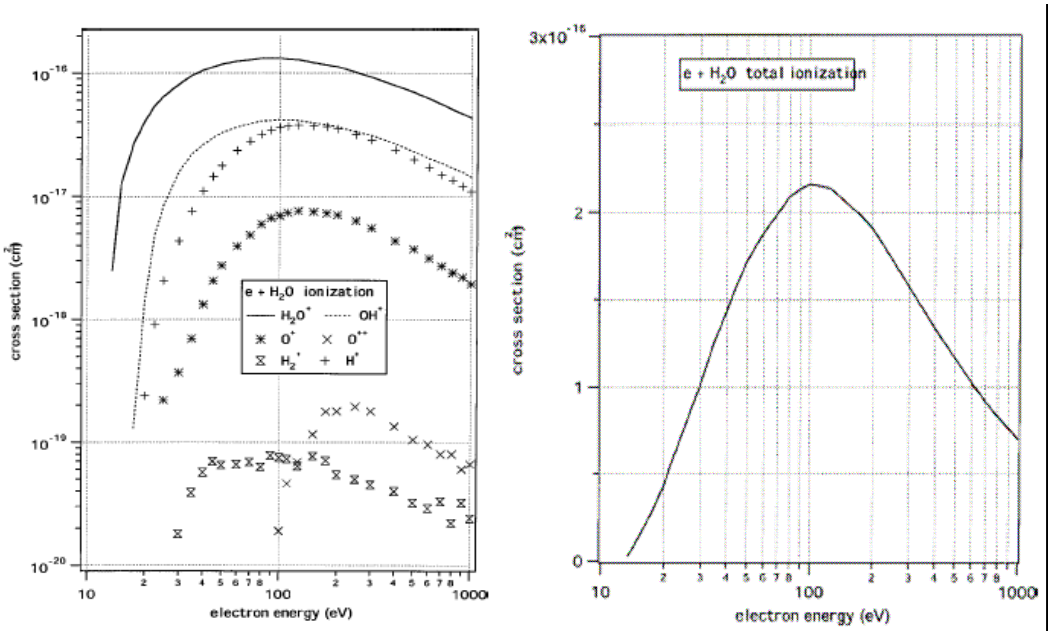

Figure 15: Partial and total ionisation cross-sections for electron impact.[70]

Much work has been conducted on the single ionisation case alone,[66] including recent studies of the triple differential cross section (cross section for the ejection of an electron into angle θ_e produced by the ionisation from an incident electron, energy E, scattered into the angle θ_s).[71,72]

(C) The electron energy is above 36.5 eV,[73] for which double ionisation can also occur along with the single ionisation processes above. The decay channels for double ionisation are,

(i) $H_2O^{++} \rightarrow H^+ + OH^+$,

(ii) $H_2O^{++} \rightarrow H^+ + O^+ + H$

(D) Finally, above 75 eV and triple ionisation processes take place. Experiments conducted by Fremont *et al*[74] cover all the above ionisation regimes by looking at single, double, and triple ionisation in the range 20-200 eV. Their results, shown below (figure 16), give the fragment energy distribution, when an effusive H_2O beam is crossed with an electron beam of a given impact energy. At 20 electron volts two peaks exist, a dominant peak labelled **b**, that arises from process (I) above, and is ~ 9 times greater than that of the peak labelled **a** attributed to process (IV). Further structure appears at 35 eV even though this is too low for direct double ionisation, **c** and **d** probably arise, as the paper suggests, due to single ionisation of an inner shell electron at ~ 32 eV and subsequent auto-ionisation giving a double ionisation effect.

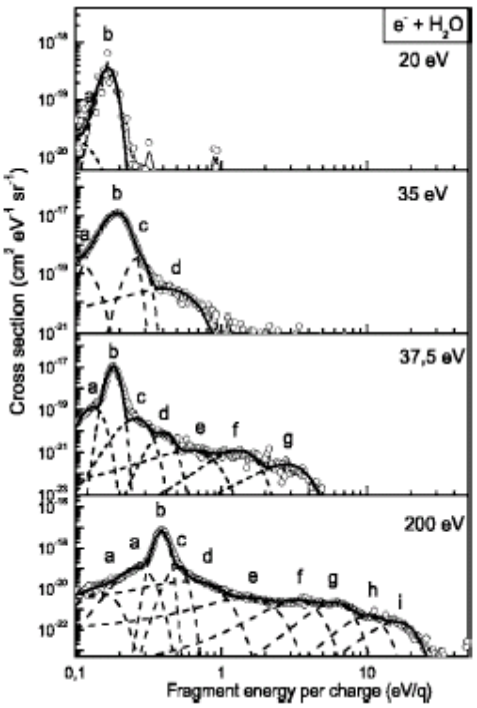

Figure 16: Electron impact fragmentation studies of water by Fremont et al.[74]

For 37.5 eV the additional features are accredited to double ionisation (C) with channels (i) and (ii) now contributing. The spectrum reveals additional structure for the maximum impact energy of 200 eV.

Research has been carried out by Scully *et al*[75] investigating auto-dissociation of doubly charged water molecules, and has led to branching ratios of the double ionisation channels (i) and (ii), shown in figure 17).

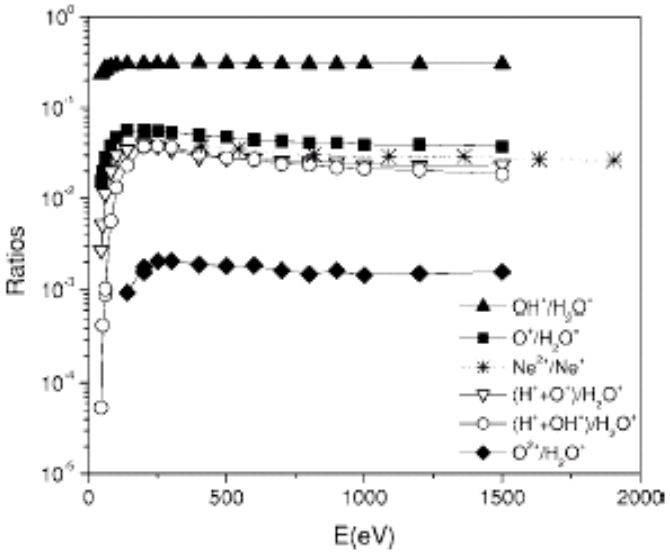

Figure 17: Auto-dissociation branching ratios of doubly charged water molecules.[75]

In conclusion, there exists a large database of cross-sectional information for the case of electron interactions with water. The importance of these studies is that they allow most permutations of the effects of secondary electron impact on water to be accounted for. This information can then be used in extracting cross-sectional information about the ionisation/dissociation of bio molecules solvated in water, or water clusters.

1.7.3 Water Clusters

In order for us to take our understanding of H_2O at the molecular level and develop it into a theory that describes liquid water one obvious route is through the study of water clusters and the variance of structure and characteristics with size and conditions. Early studies on water clusters, conducted in the 1950's by Pimental, involved the use of IR spectroscopy.[76,77] Then, in 1974, Dyke and colleagues measured the microwave spectra of small clusters generated by a molecular beam. Yet it is particularly since the 1980's that the number of experiments and theoretical treatments have blossomed and flourished. A number of reviews on the topic are available.[77,78,79,80] Research conducted to date can be separated into studies carried out on neutral water clusters, largely through spectroscopic techniques to discern structure, and studies that involve ionisation of the cluster, looking at the protonated water clusters produced using spectrometric methods. These later studies are often aimed at investigation of the processes that are ongoing in the cluster, such as aggregation and dissociation.

Neutral Water Clusters

Starting from the lower end of the mass spectrum, an approach was developed by people, like Liu, Crazan and Saykally,[78] to build up an accurate experimental picture of neutral water (dimer through to hexamer) clusters using VRT spectroscopy working in the far infra-red. The experimental data gathered showed transitions between energy levels, the result of splitting of the vibrational-rotational energy levels of the cluster. This splitting can result in at least two energy levels only by assuming quantum tunnelling occurred for the hydrogen atoms to another low potential energy configuration. It was theoretical work by Wales on the trimer, figure 18, in 1993, that rationalised the problem in terms of two isomerisation (tunnelling) methods.[81] One method involves the flipping motion of a single water molecule - the same effect as interconversion of the dangling protons in the trimer diagram. The second, more complex method, involves the rotation of a water molecule, and interconversion of the dangling protons, into a transition (bifurcation state), followed by an allowed rotation of only one of the two molecules it is connected to.

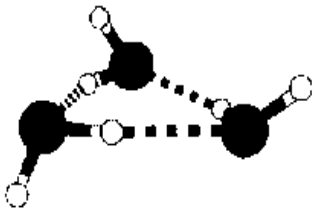

Figure 18: Lowest energy structure water trimer.[81]

Using the experimental data provided by Saykally and others, Wales continued to improve upon the trimer theory by subsequently treating and explaining the splitting and rearrangements of dimers and hexamers.[82] Since then, with the growth in algorithm methods and computational power, along with ultrafast infrared spectroscopy,[83,84,85,86] much has been revealed about the structure of neutral clusters of all sizes, with geometrical arrangements unveiled for sizes greater than 1000 molecules. Here, I present the results of a joint computational and experimental effort by Buch, Bauerecker, Devlin, Buck and Kazimirski,[80] from 2004, on large clusters, n = 20 – several 1000, which highlights some of the progress made in discerning the structure of water clusters. Based on their findings they propose that for the region n = 1 – 200 the cluster is a compact-amorphous one. At n ~ 300 a crystalline six member ring core begins to take shape and for n > 1000 cluster structures can be described as quasi-spherical, with a crystal interior and a disordered surface (figure 19).

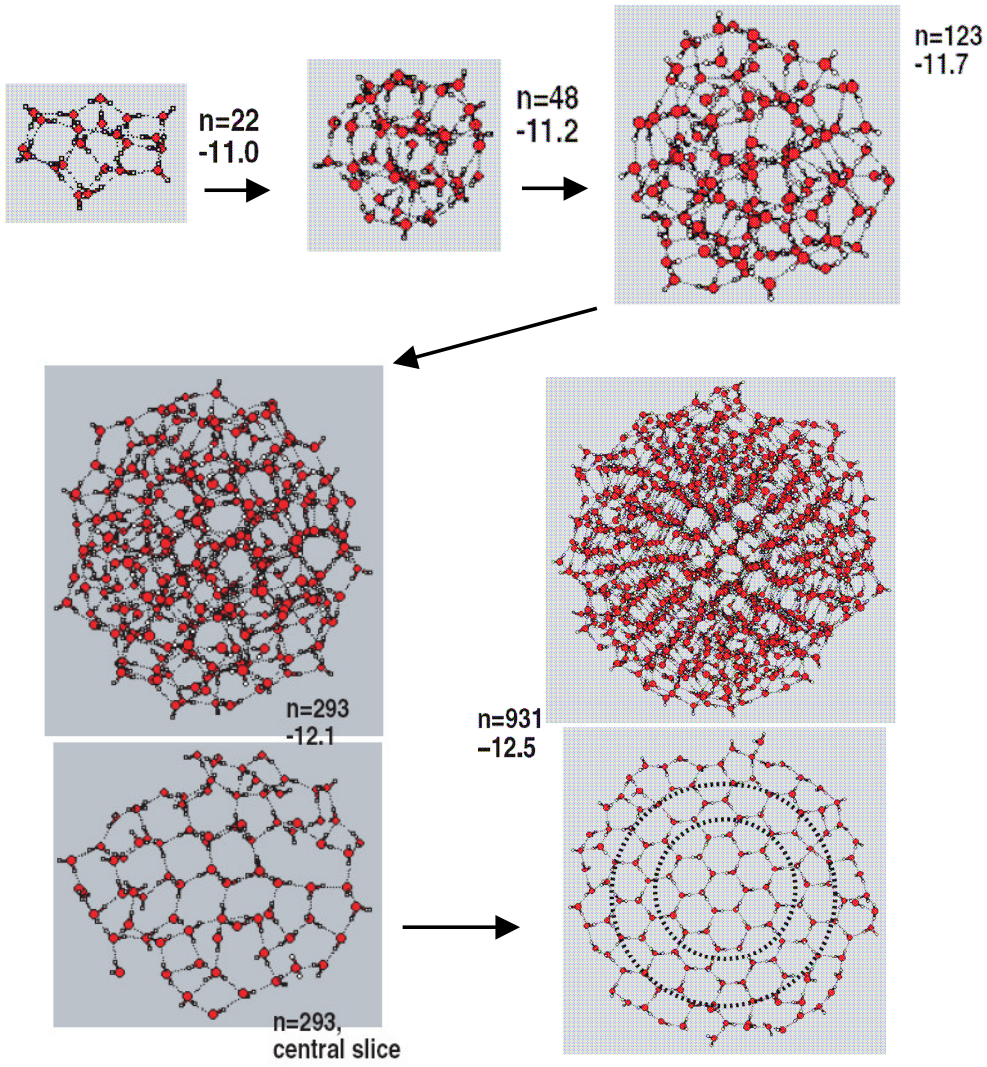

Figure 19: Proposed water cluster structures based on lowest potential energy surfaces.[80]

Protonated Water Clusters

Neutral water clusters have been studied by several mass spectrometric techniques, electron impact ionisation,[87,88,89] corona discharge ionisation,[90] resonance lamp ionisation,[91] and single photon ionisation.[92] However, when neutral water clusters are subjected to ionisation the mass spectra generated are generally dominated by the protonated cluster ions $(H_2O)_nH^+$. Unprotonated ($2 \leq n \leq 10$) clusters have been observed by applying near-threshold photons (11.83 eV) from an Ar resonance in an expansion of mixed argon/water clusters.[82] Chang *et al*[79] provide a review of work conducted on medium size protonated clusters. In a typical mass spectra (figure 20) we can observe the protonated parent clusters $(H_2O)_nH^+$**,** labelled P, and the daughter clusters $(H_2O)_{n-1}H^+$**,** designated D.

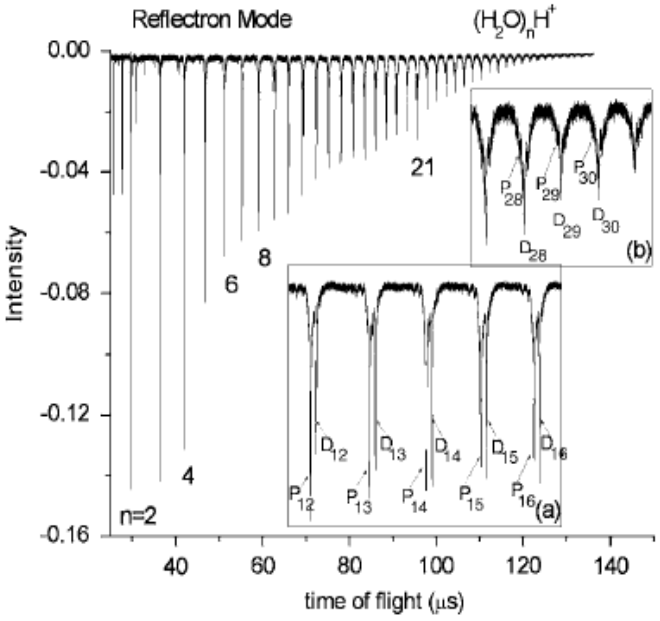

Figure 20: Time of flight mass spectrum of water clusters ionised by a soft x-ray laser (26.5 eV). [84]

The process, involved in transforming $(H_2O)_n$ to $(H_2O)_nH^+$, is similar to that of methanol, and proceeds via intracluster proton transfer,

$$(H_2O)_n + e^- \rightarrow [(H_2O)^+_n]^* + 2e^-$$

$$[(H_2O)^+_n]^* \rightarrow (H_2O)_nH^+ + OH$$

with the daughters created by unimolecular dissociation,

$$(H_2O)_nH^+ \rightarrow (H_2O)_{n-1}H^+ + H_2O$$

Other features in the mass spectrum of protonated clusters are the existence of "magic number" clusters, observable as unusually strong peaks. For water two have been identified, $(H_2O)_{21}H^+$and $(H_2O)_{28}H^+$. It was for some time unclear whether these peaks were the result of faster decay of $n = 22$ than neighbouring ions or could be attributed to an exceptionally stable $n = 21$ cluster. IR spectroscopy on the OH bond has recently shown that the formation of a highly stable clathrate structure (figure 21) is most plausible.[79]

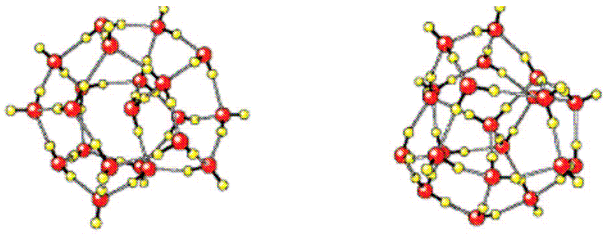

Figure 21: Plausible clathrate structure for magic number cluster $(H_2O)_{21}H^+$.[79]

The generation of unprotonated clusters occurs similarly to that for methanol. It is believed that mixed cluster ions $(H_2O)_nAr_m^+$ are formed and dissociate swiftly to $(H_2O)_n^+$**.** With insufficient excess energy having existed for proton transfer, evaporative loss of Ar is more favourable.

1.8 DNA and Low Energy Electron (LEE) Interactions

1.8.1 Introduction

It was shown in 2000 that the effects of low energy electrons (LEE) in inducing double and single strand breaks in DNA through electron attachment to the nucleobases were quite significant.[93] However, many of these studies are of gas phase DNA or DNA plasmids deposited on substrates. In its natural environment this is not the case, it is an aqueous solution that sustains its helix form in a living organism. By the evaporation of DNA, nucleobases in particular, into water clusters a very close approximation to this natural environment could be provided, one that is advantageous to the study of low energy electron interactions in a controlled manner.

In this section I will look at the effects of low energy electron impact on DNA and nucleic acids. First I provide a brief introduction to DNA, proceed by describing the sources for its damage and their effects, before looking at the research that has led to this relatively new and important area of research's growth. This will include a summary of some of the more significant findings to date. To conclude there is a section on water and nucleic acids that includes some interesting work carried out on nucleobases in water clusters.

1.8.2 DNA

DNA (deoxyribonucleic acid) is a nucleic acid in the form of a double helix that can be as long as two metres, in the case of a human chromosome, and exists in the cell nucleus. Its function is that of controlling the manner of development of all the cells in the human body through the genetic code it carries. The unique code it carries manipulates the proteins, via the sequence of amino acid residues they are comprised of, manufactured within the cell, and as a consequence of this the entire construction of a human being.

DNA is actually composed of two strands of nucleotides that are held together by hydrogen bonding of the bases that comprise the nucleotides. 165 base pairs are known as a nucleosome and form by wrapping around a complex core of histone proteins. A string of these form chromatin fibres, by continuation on up until we have a chromosome, with the scale and packing shown in figure 22.[94] A nucleotide is a chemical compound that consists of a heterocyclic base, a sugar, and one or more phosphate groups. There are four standard bases involved in DNA nucleotides, adenine, guanine, cytosine and thymine (figure 23).

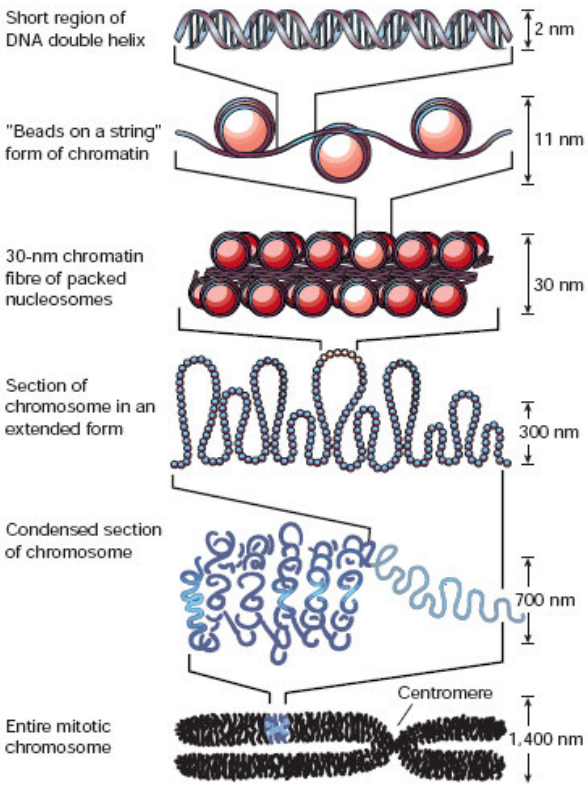

Figure 22: The organisation of DNA within a chromosome.[94]

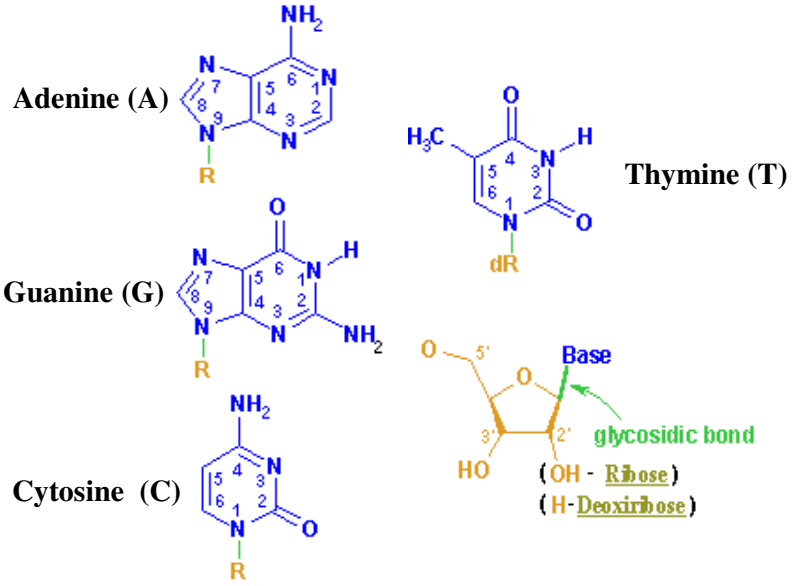

Figure 23: DNA bases Adenine (A), Thymine (T), Cytosine (C) and Guanine (G). Bottom right is a pentose sugar that forms part of the helix backbone.

These bases can be arranged along the backbone in any order. This allows for a great degree of uniqueness, because of the number of permutations that are available. Two strands are combined in a helix only as long as the bases are bonded to complementary bases i.e. A to T and G to C. These are called base pairs, (figure 24), and are a crucial factor in replication of the double-stranded structure of DNA.

In replication the two strands separate. Then each strand's complement is recreated by exposure to a mixture of the four bases. An enzyme creates a complementary strand by finding the correct base in the mixture by virtue of "which key fits" and bonding it with the original strand. In this way the base on the old strand dictates which base appears on the new strand, and the cell ends up with an extra copy of its DNA.

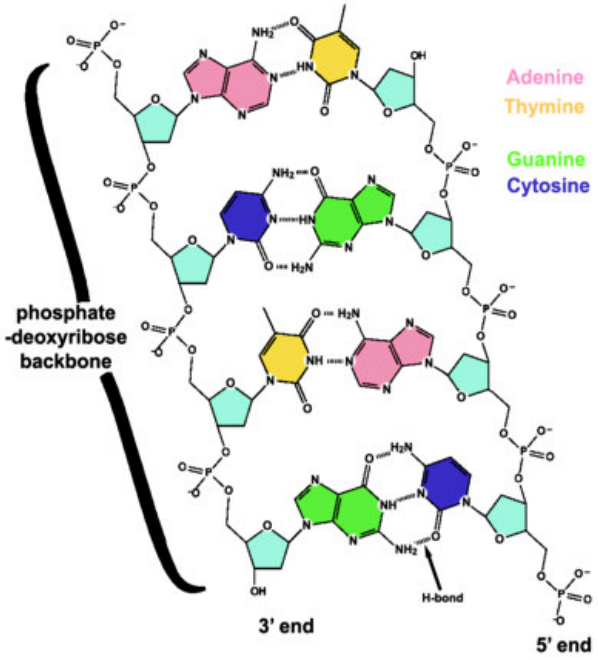

Figure 24: Hydrogen bonding of DNA bases.

In order for DNA to translate its instructions into proteins, it must communicate its message to ribosomes, external to the nucleus of the cell via RNA. RNA differs in that it contains just one strand of the DNA, has uracil instead of thymine, and ribose instead of deoxyribose.

1.8.3 DNA Damage

Damage to DNA can occur in several ways, both due to internal chemical or metabolic processes (endogenous), and external damage sources (exogenous). Of interest are the exogenous process and they exist in a handful of forms:[95]

1. Ultraviolet radiation from the sun, which can lead to skin cancer.
2. Human made mutagenic chemicals that attack the cells.
3. Chemotherapy and radiotherapy.
4. Plant toxins.
5. Other radiation forms i.e. X-rays and γ-rays, the effect of which leads to the creation of secondary electrons within cells, 10^4 per 1MeV deposited.[96] It is these slow electrons and the consequences of their interactions that we are interested in.

Along the path (track) taken by radiation in a cell several reactive species are created, radicals, ions and the aforementioned electrons. Subsequently these species interact with the constituent elements of the DNA, the nucleic acid bases or the deoxyribose sugars causing structural or chemical changes. If this initial damage is not repaired quickly enough by the mechanisms that exist within the cell for this purpose, the damage to the DNA, before replication, can lead to incorporation of wrong bases opposite damaged ones. Daughter cells that inherit these wrong bases carry on these mutations and the damage is irreparable. If a cell accumulates enough damage without sufficient repair it then enters one of three possible states:

1. A state of inactivity or dormant state (*senescence*).
2. Cell suicide (*apoptosis*)
3. Unchecked cell division that grows beyond control leading to a tumour that is cancerous.

If only one strand of a double helix has a defect imposed, this is known as a *single strand break* (SSB). The undamaged strand is then used as a standard by which to repair its complementary half. More dangerous are the occurrence of breaks in both strands-

double strand breaks (DSB). In this case the consequences are hazardous. Two repair mechanism exist to fix this, one which patches the strands together with certain loss of sequence information (non-homogeneous end joining NHEJ), and another that relies on a neighbouring template, but both fail to operate complete recovery. It is now known that the low energy secondary electrons with energies below the ionisation threshold of DNA can induce these single and double strand breaks. This research is discussed in the next section.

1.8.4 Low Energy Electron studies involving DNA and its Bases

Research into understand the effects secondary electrons, created by ionising radiation, have on DNA is a relatively new area of research and is being conducted by many groups, notably those of L. Sanche[93,97] and T.D. Märk.[104,105] These low-energy secondary electrons are generated by electron-impact ionization caused by high-energy electrons, originally produced directly by the ionizing radiation. In the electron-impact ionization process, the scattered electron loses part of its kinetic energy, while another electron is ejected, with energy much lower than the first one. It was believed that because these secondary electrons are created in greatest abundance with energies in the range 1- 20 eV,[96] and these energies are below ionization range, that they could be ignored in terms of their effects on DNA. In 2000 Boudaïffa *et al*[97] presented findings that challenged this consensus; they showed that damage to nucleic acids, in the form of single and double strand breaks (SSB/DSB) in particular, can be generated through electron attachment to the acid followed by bond breaking due to energy transfer to an anion. This initial work, on plasmid DNA, discovered strong bond breaking peaks at 10eV, both single and double in ratio 4:1, shown in figure 25. Since then these findings have been reconfirmed, also showing strand breaking for energies below 4 electron volts (figure 26), from work conducted on DNA thin films.[98,99]

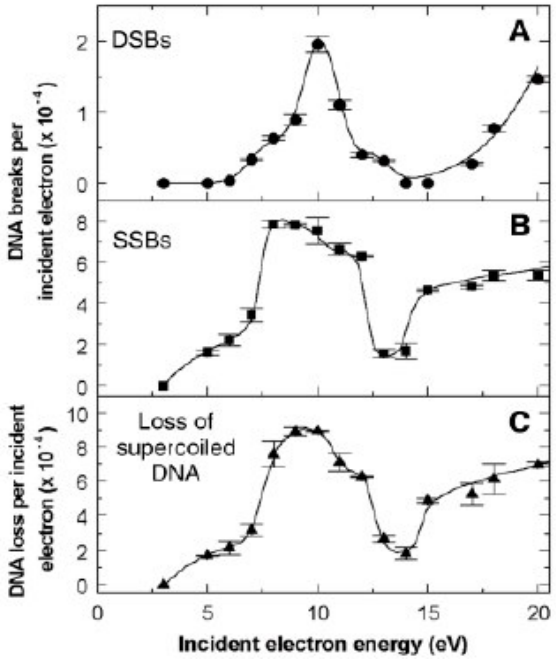

Figure 25: Single and double strand breaking of DNA.[97]

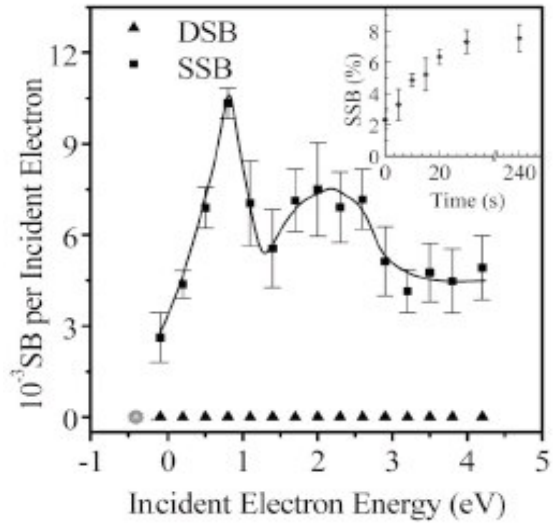

Figure 26: Evidence of DNA damage for incident electron energy E < 4 eV.[99]

In 2005 L. Sanche reviewed work done and concluded that, [100]

1. Below 15 eV bond ruptures in DNA and its bases occur via the formation of transient anions decaying into dissociative electronically excited states or into the dissociative electron attachment (DEA) channel.
2. Above 15 eV rupture occurs via direct scattering but transient anions can play a role up to 40 eV.
3. Any damage induced depends on the transient lifetime of the anion, which in turn depends on the environment of the molecules.
4. Bond cleavage is considerably increased by substitution of a halogen atom.
5. Scattering of the anions formed by DEA give rise to secondary products, particularly OH^- from the backbone. By this mechanism a break in one strand producing a radical or anion can lead to a double strand break via its scattering off that strand reactively.

Subsequent experimental work[101,102] has led to a proposed model for the resonance interaction of low energy electrons (LEE) with DNA which builds on points 1 and 5 above: [103]

The incoming LEE are captured forming a core excited/core excited shape resonance on a DNA base at energy E_0 close to, or above, the first electronic excitation energy threshold forming a transient anion. This anion can decay by any one of three channels (figure 27):

1. Elastic channel - The electron is re-emitted with the same incident energy. It can be emitted back into vacuum (e_v^-), or transferred within the strand (e_t^-); above 4 eV the vacuum case becomes increasingly likely.

2. Inelastic channel – The base becomes electronically excited along with the release of a low energy electron (0 - 4 eV), again into vacuum or along the strand.

3. DEA channel – Fragmentation of the base itself occurs.

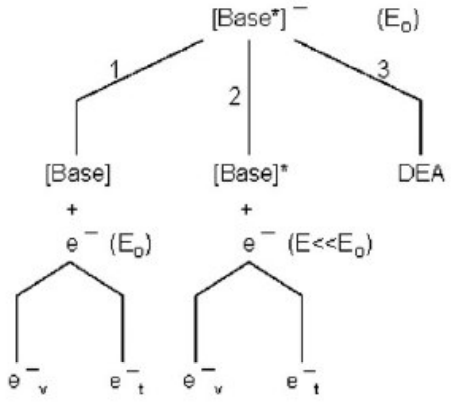

Figure 27: Decay channels for transient anion formed by LEE interaction with DNA.[103]

The branching ratio of these channels is believed to depend on the magnitude of the departing electron wavelength.[103] The geometrical arrangement of the bases is also emphasized for its role. It is also concluded that most strand breaks occur via channel 1 whereby an electron transfers from a base to the phosphate group causing subsequent rupture of the C-O bond via DEA.

Concurrent to this much work has been done also on low energy electron attachment to the bases; cytosine, thymine, uracil, and adenine have been all been studied.[104,105,106,107] The dissociated fragments that occur after DEA have been the primary source of analysis. Of the fragmentations observed the most abundant are the dehydrogenated molecules (figure 28), with no detections of the parent anions before fragmenting. As for DNA strands the process begins with resonant electron capture forming a transient anion, which decays as follows,

$$e^- + M \rightarrow M^{-*} \rightarrow (M - H)^- + H^*$$

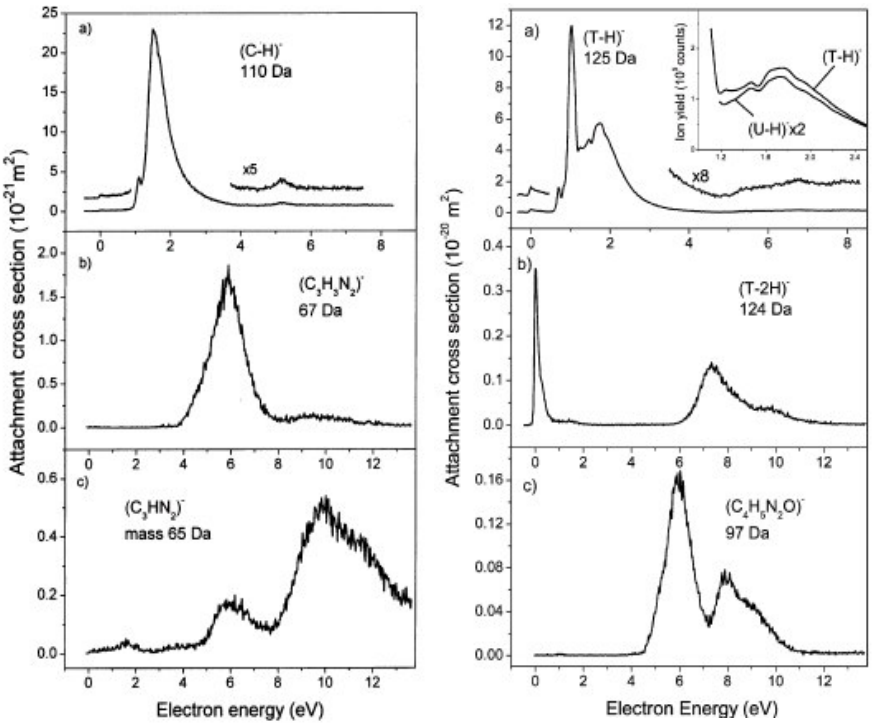

Figure 28: Electron attachment and fragmentation for cytosine(left), thymine(right).[104] Notice the abundance in the production of de-hydrogenated molecules $(X\text{-}H)^-$.

This process occurs largely below 3 eV. Studies conducted on bromouracil and thymine show that, while these low energy resonant electron attachments are pronouncedly exhibited, the cross sections differ by more than two orders of magnitude, with bromouracil being the larger of the two.[108,109] Because it was known that replacement of thymine with bromouracil leads to an increase in sensitivity to ionizing radiation these studies further support the idea that the initial mechanism responsible for direct DNA damage is this bond cleavage by low energy secondary electrons. A further finding is the influence of functional groups on bond and site selective dissociation.[110] This implies the possibility of controlling and inducing select chemical reactions by using specific electron impact energies for DEA.

1.8.5 Water and Nucleic Acids

Water is critical to the DNA helix. Without the screening of water the phosphate groups repel one another and the familiar helix becomes distorted and can in some sense be said to collapse.[66] It has also been shown that water mediates certain protein - DNA interactions, and that these interactions become less likely as dehydration is imposed.[66]

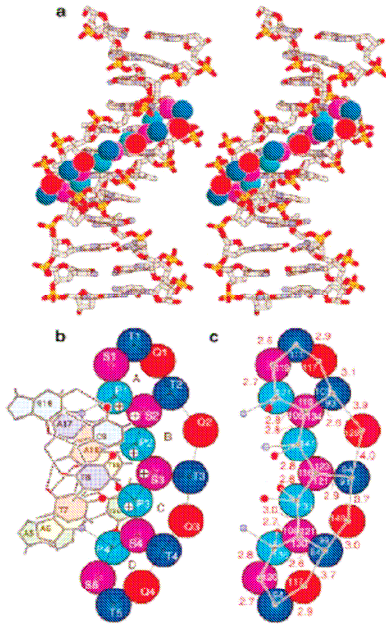

Figure 29: Hydration layers of DNA.[66]

Thus, if we are to truly understand the effects of low energy secondary electrons in causing damage to DNA, then we must also understand how water is effected by low energy electrons and whether its enveloping of the helix provides protection or increases the damage inflicted. This is not clear. Date *et al*[111] calculated and compared the ionisation and excitation effects of the secondary electrons ejected by the primary process of low energy proton impact around the Bragg peak region of liquid water. The processes due to the secondary electrons are more than 50% of the total processes (figure 30). In an ideal protective environment for DNA the solution would keep to a minimum the production of these damaging electrons.

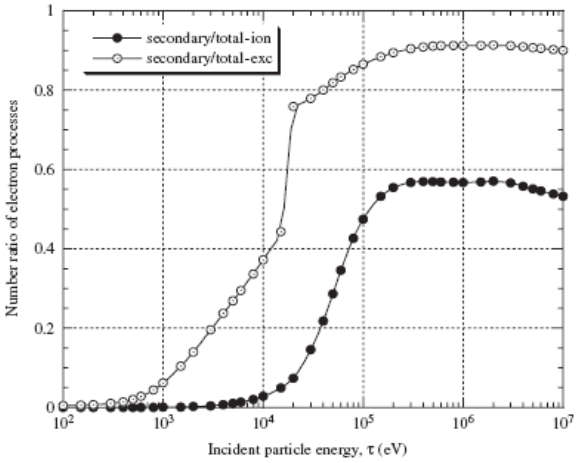

Figure 30: Ratio of secondary and primary processes (low energy proton impact for ionisation and excitation.[111]

A recent experiment, involving the impact of LEE's on a substrate of short single strand DNA covered by 3 monolayers of water (60% of first hydration layer), reveals the increase by a factor of 1.6 in the damage inflicted by DEA on DNA.[112] The formation of unseen-before transient anions due to water bondage to DNA at the oxygen of a phosphate group is believed to be the cause.

On the other hand we have the work of Liu *et al*[113], where they fragment anions of adenosine 5'-monophosphate (AMP^-), as well as AMP^-, solvated in differing numbers of water molecules, by collision with 50 keV neutral atoms. For isolated AMP^- various fragmentations occur, however by solvating in water, with *n* larger than 13 per molecule, the AMP^- becomes entirely protected with the loss of water the observable fragmentation process (figure 31). Though in this case water does provide a protective environment for AMP^-, it remains to be seen that this holds true for a broader spectrum of biomolecules and DNA bases, under varying collision conditions, specifically low energy electron impact.

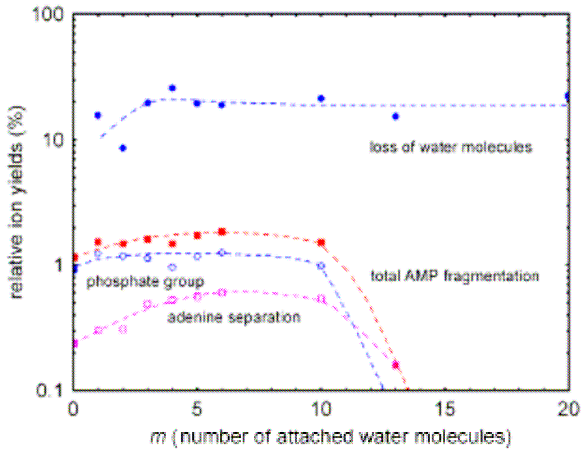

Figure 31. Relative ion yields for dissociation of AMP^- solvated in water molecules of number m.[113]

In another closely related piece of work, mass spectrometry of anions formed by DEA to nucleobase molecules and clusters embedded in helium droplets has shown that, while stable transient parent anions do occur (unlike the gas phase), an increase is observed in the cross section of fragment dehydrogenated anions over a wide energy range up to 15 eV (usually less than 3 eV).[114,115] If these cold droplets are more akin to the actual biological environment of relevance, over the gas phase, then this may be very significant in its implications for radiation damage.

1.9 Research at Maynooth

The purpose of the research described in this Masters of Science thesis (at the National University of Ireland Maynooth) was to develop an operational apparatus for the study of the interaction of electron impact fragmentation of molecular clusters. Through the observation of ion fragments and neutral metastables produced when these targets are impinged by low-energy electrons it might be possible to extract information on what processes are at work in molecular or DNA damage caused by radiative sources. In particular it is a long-term goal for this experiment to be used in studying the effects of low-energy electron impact on nucleobases solvated in water or methanol clusters.

The work had several primary objectives, including the development of an operational cluster source, the design, construction, and implementation of a functional neutral metastable detector, and the modification of the electron gun through the incorporation of a deflection system. Secondary objectives included the development of several computer programs, for control of the electron impact energy, for the acquisition of data and excitation functions, and for quick data analysis. Other work included minor modifications and implementations aimed at optimising the system.

Chapter 1 has provided an overview of current research that is the motivation for these developments.

Chapter 2 contains a review of the various methods used to generate clusters, a more detailed description of the supersonic expansion method employed in this work, and a summary of the time-of-flight methods of ion detection and neutral metastable detection.

Chapter 3 provides a description of the apparatus and the modifications and implementations made to it. Clusters are produced by a supersonic expansion from a pulsed valve with nozzle. Electrons impact upon these neutral clusters causing ionisation and subsequent dissociation leading to neutral and ionised fragments. Ions are extracted into a time-of-flight mass spectrometer and a multichannel scaler records a

mass spectrum. Alternatively neutral metastables fragments can be detected as a function of their time-of- flight.

Chapter 4 gives a detailed description of the interfacing techniques employed, the programs (LabVIEW) that have been developed for control of the electron impact energy, acquisition of scans/excitation functions, and data analysis, as well as a look at code written for analysis of the time-of-flight spectra.

Chapter 5 is the experimental chapter and describes the tests performed, time-of-flight scans taken for ions and neutral metastables, and displays the results obtained.

1.10 References

[1] R. L. Johnston "*Atomic and Molecular Clusters*", Taylor and Francis, London (2002)

[2] *http://www.lsbu.ac.uk/water/images/platon1.jpg*

[3] *http://www.saltinstitute.org/images/nacl1.gif*

[4] T. P. Martin, "*Elemental and Molecular Clusters*", Springer-Verlag, Berlin (1998)

[5] M. A. Duncan and D. H. Rouvray, "*Microclusters*", Sci. Amer. (December 1989)

[6] C. P. Schulz, R. Haugstatter, H Tittes, *J. Phys. D.* **10** (1988) 279

[7] C. L. Chien, *Annual Rev. Mat. Sci.* **25** (1995) 129

[8] G. Schmidt, *Chem. Rev.* **92** (1992) 1709

[9] T. S. Ahmadi, Z. L. Wang, T. C. Green, A. H. Mostafa, A. El-Sayed, *Science* **272** (1996)**,** 1924

[10] N. Tian, Z. Y. Zhou, S. G. Sun, Y. Ding, and Z. L. Wang, *Science* **316** (2007) 732

[11] R. L. Whetten, J. T. Khoury, M. M. Alvarez, S. Murthy, I. Vezmar, Z. L. Wang, C. C. Cleveland, W. D. Luedtke, U. Landman, *Adv. Mat.* **8** (1996) 428

[12] D. J. McGinty, *J. Chem. Phys.* **55** (1971) 580

[13] J. K. Lee, J.A. Barker and F.F. Abraham, *J. Chem. Phys*. **58** (1973) 3166

[14] P.K. Doye, *"The structure, thermodynamics and dynamics of atomic clusters"* PhD Thesis (University of Cambridge, 1996)

[15] M. Boudart, *Nature* **372** (1994) 320

[16] Z. Xu, F. S. Xiao, B.C. Gates, *Nature* **372** (1994) 346

[17] R. Boyle, *The Sceptical Chymist* (1661)

[18] M. Faraday, *Phil. Trans. Roy. Soc. London* **147** (1857) 145

[19] S. A. Ochs, R. E. Coté, P. Kusch, *J. Chem. Phys*. **21** (1953) 459

[20] A. Kantrowitz and J Grey, *Rev. Sci. Inst.* **22** (1951) 328

[21] E. W. Becker, Z. Bier, W. Henkes, *Z. Phys.* **146** (1956) 333

[22] O. Echt, K Sattler, E. Recknagel, *Phys. Rev. Lett.* **47 (**1981) 1121

[23] W. Miehle, O. Kandler, T. Leisner, *J. Chem. Phys.* **91** (1989) 5940

[24] R. Karnbach, M. Joppien, J. Staplefeldt and J. Wörmer, *Rev. Sci. Inst.* **64** (1993) 2838

[25] W. Kamke, J.Devries, J. Krauss, E. Kaiser, B. Kamke, *Z. Phys. D* **14** (1989) 339

[26] A. Burose, C. Becker, A. Ding, *Z. Phys. D.* **20** (1991) 35

[27] W. Kedziersky and J. W. McConkey, *J. Chem. Phys.* **107** (1997) 6521

[28] E. T. Verkhovetsova, E. A. Bondarenko, Y S Doronin, *Opt. Spect.* **63** (1987) 22

[29] P. J. M. van der Burgt and J. W. McConkey, *J. Chem. Phys.* **102** (1995) 8414

[30] C. P. Malone, W. Kedziersky, J. W. McConkey, *J. Phys. B: Atom. Mol. Opt.* **36** (2003) 3607

[31] W. D. Knight, K. Clemenger, W. A. de Heer, W. A. Saunders, M. Y. Chou and M. L. Cohen, *Phys. Rev. Lett.* **52** (1984) 2141

[32] H. W. Kroto, J. R. Heath, S. C. O'Brien, R. F. Curl, R. E. Smalley, *Nature* **347** (1985) 354

[33] www.theory.chem.cf.ac.uk/~nickw/c60

[34] S. Iijima, *Nature* **354** (1991) 56

[35] www.weizmann.ac.il/kimmel-nano/Home/nanotube.jpg

[36] S. Bates, "*When simple systems do complex things"* Capability Computing **4** (2004) 3

[37] C. S. Cummings and W. Bleakney, *Phys. Rev.* **58** (1940) 787

[38] G. Vikor and M. V. Kurepa, *J. Serb. Chem. Soc.***61** (1996) 437

[39] N. Durič, I. Cadez and M. Kurepa, *Fizika* **21** (1989) 339

[40] J. Appel and C. Kubach, *Chem. Phys. Lett.* **11** (1971) 486

[41] T. G. Finn, B. L. Carnahan, W. C. Wells, and E. C. Zipf, *J. Chem. Phys.* **63** (1975) 1596

[42] D. E. Donohue, J.A. Sciavone and R.S. Freund, *J. Chem. Phys.* **67** (1977) 769

[43] J. A. Schiavone, D.E. Donohue, R.S. Freund, *J. Chem. Phys.* **67** (1977) 759

[44] W. von Niessen, G. Bieri, L. Åsbrink, *J. El. Spect. Rel. Phen.* **21** (1980) 175

[45] T. Skalicky and M. Allan, *J. Phys. B.* **37** (2004) 4849

[46] D. Bouchiha, J. D. Gorfinkiel, L. G. Caron and L. Sanche, *J. Phys. B.* **40** (2007) 1259

[47] B. Ibănescu, O.May, A.Monney, and M.Allan, *Phys. Chem. Chem. Phys.* **9** (2007) 3163

[48] V. Prabhudesai, A. H. Kelkar, D. Nandi, and E. Krishnakumar, *Phys Rev. Lett.* **95** (2005) 143202

[49] M. Ziskind, C. Mihesan, N. Lebrun, B. Chazallon, C. Focsa and J.L. Destombes, *Appl. Phys. A* **79** (2004) 991

[50] S. Morgan and A. W. Castleman, Jr., *J. Am. Chem. Soc.* **109** (1987) 2867

[51] S. Morgan, R. G. Reese, and A. W. Castleman, Jr., *J. Am. Chem. Soc*. 111 (1989) 3841

[52] F. Dong, S. Heinbuch, J.J. Rocca and E.R. Bernstein, *J. Chem. Phys.* **124** (2006) 224319

[53] M. El-Shall, C. Marks, L.W. Sieck and *M*. Meot-Ner, *J. Phys. Chem*. **96** (1992) 2045

[54] H. Bergesen M. Abu-samha, A. Lindblad, R. R. T. Marinho, G. Öhrwall, M. Tchaplyguine, K. J. Børve, S. Svensson, and O. Björneholm, *J. Chem. Phys.* **125** (2006) 184303

[55] G. Vaidyanathan, M. T. Coolbaugh, W. R. Peifer and J. R. Garvey, *J. Chem. Phys.* **94** (1991) 1850

[56] E. S. Wisniewski, M. A. Hershberger and A. W. Castleman, Jr., *J. Chem. Phys.* **116** (2002) 5738

[57] M. Abu-Samha, K. Børve, J. Harnes, and H. Bergersen, *J. Phys. Chem. A*. **111** (2007) 8904

[58] M. Abu-Samha, K. J. Børve, L. J. Sæthre, G. Ohrwall, H. Bergersen, T. Rander, O. Björneholm, M. Tchaplyguine, *Phys. Chem. Chem. Phys.* **8** (2006) 2473

[59] E. Tsuchida, Y. Kanada, and M. Tsukada, *Chem. Phys. Lett.* **311** (1999) 236

[60] J. H. Guo, Y. Luo, A. Augustsson, S. Kashtanov, J. E. Rubensson, D. K. Shuh, H. Agren, and J. Nordgren, *Phys. Rev. Lett.* **91** (2003) 157401

[61] J. H. Guo, Y. Luo, A. Augustsson, S. Kashtanov, J. -E. Rubensson, D. Shuh, V. Zhuang, P. Ross, H. Ågren, J. Nordgren, *J. El. Spec. Rel. Phen.* **137** (2004) 425

[62] S. Kashtanov, A. Augustson, J.-E. Rubensson, J. Nordgren,. H. Agren, J.-H. Guo and Y. Luo, *Phys Rev. B.* **71** (2005) 104205

[63] G. Baratta, G. Leo, and M. E. Palumbo, Astronomy and Astrophys. 384 (2002) 343

[64] P. Ball, "*H_2O: The biography of water*", Weidenfeld and Nicolson (1999)

[65] M. Chaplin, http://www.lsbu.ac.uk/water/.html

[66] P. Ball, *Chem. Rev.,* **108** (2008) 74

[67] Y. Itikawa and N. Mason, *J. Phys. Chem. Ref. Data*, **34** (2005) 1

[68] H. Cho, H. Lee and Y. S. Park, *Radiat. Phys. Chem*., **68** (2003) 115

[69] A. Faure, J. D. Gorfinkel and J. Tennyson, *J. Phys. B: At. Mol. Opt. Phys.*, **37** (2004) 801

[70] H. C. Straub, B. G. Lindsay, K. A. Smith, and R. F. Stebbings, *J. Chem. Phys.*, **108** (1998) 109

[71] C. Champion, C. Dal Cappello, S. Houamer and A. Mansouri, *Phys. Rev. A*, **73** (2006) 012707

[72] D. S. Milne, S. J. Cavanagh, Birgit Lohmann, C. Champion, P. A. Hervieux and J. Hanssen, *Phys. Rev. A*, **69** (2004) 032701

[73] S. J. Cavanagh, S. Y. Truong, P. Bolognesi, and G. C. King, *Sci. Rep. SRS, Atom. Mol. Spectr.*, **2** (2000)

[74] F. Frémont, C. Leclercq, A. Hajaji, A. Naja, P. Lemennais, S. Boulbain, V. Broquin, and J. Y. Chesnel, *Phys. Review A***, 72** (2005) 042702

[75] S. W. Scully, J. A. Wyer, V. Senthil, and M. B. Shah, *Phys. Review A*, **73** (2006) 040701

[76] R. L. Johnston, "*Atomic and Molecular Clusters*", Taylor and Francis, London and New York (2002)

[77] F. N. Keutsch and R. J. Saykally, *Proc. Nat. Acad. Sci of United States*, **98** (2001) 10533

[78] K. Liu, J. D. Cruzan, R. J. Saykally, *Science,* **271** (1996) 5251

[79] H. Chang, C. Wu, J. Kuo, *Int. Rev. Phys. Chem.,* **24** (2005) 553

[80] V. Buch, S. Bauerecker, J.P. Devlin, U. Buck and J.K. Kazimirski, *Int. Rev. Chem. Phys.,* **23** (2004) 375

[81] D. J. Wales, *J. Am. Chem. Soc*., **115** (1993) 11180

[82] D. J. Wales, Rearrangement of Water Dimer and Hexamer, in "*Theory of Atomic and Molecular Clusters*", J. Jellinek (Ed.), Springer-Verlag, Berlin (1999)

[83] C. J. Fecko, J. J. Loparo, S. T. Roberts, and A. Tokmakoff, *J. Chem. Phys.,* **122** (2005) 054506

[84] S. Woutersen and H. J. Bakker, *Phys. Rev. Lett***., 96** (2006) 138305

[85] T. Steinel, J. B. Asbury, J. Zheng, and M. D. Fayer, *J. Phys. Chem. A*, **108** (2004) 10957

[86] R. Rey, K.B. Moller , J.T. Hynes, *J. Phys. Chem. A*, **106** (2002) 11993

[87] O. Echt, D. Kreisle, M. Knapp, and E. Recknagel, *Chem. Phys. Lett.*, **108** (1984) 401

[88] U. Nagashima, N. Nishi and H. Tanaka, *J. Chem. Phys.*, **84** (1986) 209

[89] C. Bobbert, S. Schütte, C. Steinbach, U. Buck, *Eur. Phys. Journ. D*, **19** (2002) 183

[90] M. Okumura, L. I. Yeh, J. D. Myers, Y. T. Lee, *J. Phys. Chem.*, **94** (1990) 3416

[91] N. Nishi, H. Shinohara, K. Yamamoto, U. Nagashima, N. Washida, *Far. Disc. Chem. Soc.*, **82** (1986) 359

[92] F. Dong, S. Heinbuch, J.J. Rocca and E.R. Bernstein, *J. Chem. Phys.,* **124** (2006) 224319

[93] B. Boudaiffa, P. Cloutier, D. Hunting, M. A. Huels and L. Sanche, *Science*, **287** (2000) 1658

[94] G Felsenfeld and M Groudine, *Nature* **421** (2003) 441

[95] J. D. Watson, "*Molecular Biology of the Gene*" Peason Benjamin Cummings CSHL Press (2004) 5th ed.

[96] International Commision on Radiation Units and Measurements, ICRU Report 31 (1979)

[97] B. Boudaïffa, P. Cloutier, D. Hunting, M. A. Huels and L. Sanche, *Science* **287** (2000) 1658

[98] L. Sanche, Mass Spectrom. Rev. **21** (2002) 349

[99] F Martin, P. D. Burrow, Z. Cai, P. Cloutier, D. Hunting and L. Sanche, *Phys. Rev. Letters*, **93** (2004) 6

[100] L. Sanche, *Eur. Phys. Journal* **35** (2005) 367

[101] Y. Zheng, J. Richard Wagner, and Léon Sanche, *Phys. Rev. Lett.* **96** (2006) 208101

[102] Y. Zheng, Pierre Cloutier, Darel J. Hunting, J. Richard Wagner, and Léon Sanche, *J. Chem. Phys.* **124** (2006) 064710

[103] S. Ptasińska and L. Sanche*, Phys. Chem. Chem. Phys*. **9** (2007) 1730

[104] S. Denifl, S. Ptasińska, M. Probst, J. Hrusak, P. Scheier, and T. D. Märk, *J.Chem.A*, **108** (2004) 6562

[105] S. Ptasińska, S. Denifl, B. Mróz, M. Probst, V. Grill, E. Illenberger, P. Scheier, and T. D. Märk, *J. Chem. Phys.* **123** (2005) 124302

[106] M. Imhoff, J. Deng and M. A. Huels, *Int. J. Mass Spect.* **245** (2005) 68

[107] S. Ptasińska, S. Denifl, V. Grill, T. D Märk, P. Scheier, S. Gohlke, M. A. Huels, and E. Illenberger, *Angew. Chem. Int. Ed.* **44** (2005) 1647

[108] K. Aflatooni, G. A. Gallup, P. D. Burrow*, J.Phys. Chem. A* **102** (1998) 6205

[109] S. Gohlke and E. Illenberger, *Europhysics News*, **33** (2002)

[110] S. Denifl, P. Sulzer, D. Huber, F. Zappa, M. Probst, T. D. Märk,, P. Scheier, N. Injan, J. Limtrakul, R. Abouaf, and H. Dunet, *Angew. Chem. Int. Ed*. **46** (2007) 5238

[111] H. Date, Sutherland, T. Hayashi, Y. Matsuzaki and Y. Kiyanagi, *Rad. Phys. and Chem.*, **75** (2006) 179

[112] S. Ptasińska and L. Sanche, *Phys. Rev. E* **75** (2007) 031915

[113] S. Liu, S. Brøndsted Nielsen, and P. Hvelplund, H. Zettergren and H. Cederquist, B. Manil and B. A. Huber, *Phys. Rev. Lett.*, **97** (2006) 133401

[114] S. Denifl, F. Zappa, I. Mähr, J. Lecointre, M. Probst, T. D. Märk, and P. Scheier, *Phys. Rev. Lett.* **97** (2006) 043201

[115] S. Denifl, F. Zappa, A. Mauracher, F. F. da Silva, A. Bacher, O. Echt, T. D. Mark, D. K. Bohme and P. Scheier, *Chem. Phys. Chem*. **9** (2008) 1387

CHAPTER 2

Clusters - Sources and Detection

2.1 Generating Clusters

Many factors are of concern when building a cluster source: what atoms or molecules are being dealt with; what size clusters we are interested in; do we want to deposit the clusters or can they be free; can we allow the clusters to be at a any temperature; what are the available vacuum conditions; and so on. Consideration of these factors has led to many different methods for generating clusters. These methods have all been substantially reviewed.[1,2,3,4] In this chapter I will provide a short summary of these methods. The method used in this work – supersonic expansion - will be discussed in a more detail in section 2.2.

Gas Aggregation – In this method atoms or molecules are evaporated into a flowing, or stationary cold gas. Then, due to energy transfer upon collision, cooling occurs, followed by condensation and clustering. The intensities obtained are lower than those obtained from supersonic jets, however they can be used efficiently for producing large clusters (n < 10,000). Evaporation techniques are used for studies involving biomolecules that are heated and seeded into a carrier gas for subsequent beam line studies.[5] In a modified form the gas aggregation technique has also been used to produce biomolecules, SO_2, SO_3, $ClONO_2$, and HCl, solvated in large water clusters.[6] Figure 32 show a typical gas aggregation source (*left*) used to generate sodium clusters (*right*).[7]

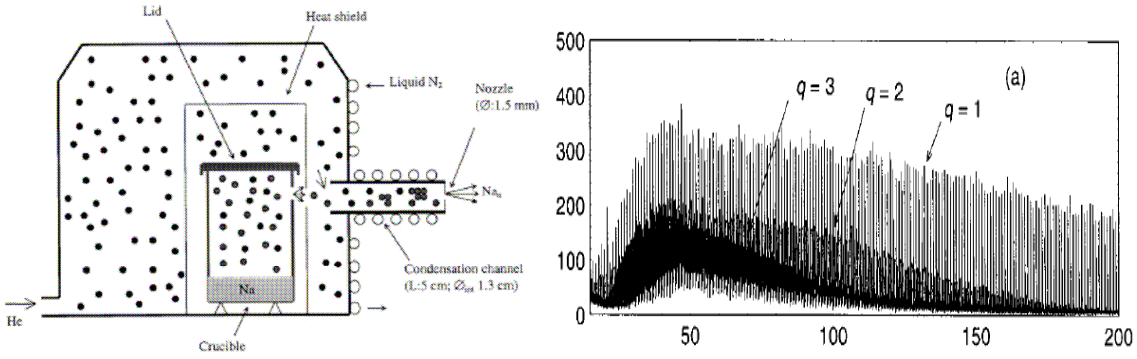

Figure 32: Gas aggregation source, (left), used in the generation of sodium clusters, mass spectrum (right).[5]

Laser vaporisation source - A high-energy laser is focussed and pulsed onto a target material. This evaporates atomic layers from, and beneath, the surface. In the subsequent energetic plasma, formed about the laser focus, expansion and cluster formation occurs. The cluster intensity per pulse is quite high, however when averaged over a cycle is not as high as that from nozzles in an expansion. By ablating into a cold inert, gas cluster formation can be enhanced. This source produces neutral and ionic species.

Electrospray Ion source (ESI) – This source (figure 33) is used to generate solvated ion clusters by injecting a solution through a surgical needle. The needle is held at a high positive or negative voltage (several kV). The emerging solution becomes charged and disperses into a fine mist by Coulomb forces. Due to the fields present the charged droplet that make up this mist migrate towards the glass capillary. The droplet travels down the capillary until molecular cluster ions, or molecular ions are formed due to cyclical reactions, evaporation and Coulomb explosions.[8] Originally developed for the study of large organic molecules this method has recently been used to produce nucleotides in water clusters.[9]

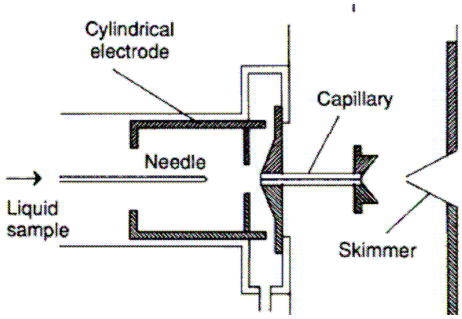

Figure 33: Electrospray Ion Source (ESI) - Small, charged droplets produced by the electrospray evaporate, generating a high electric field at the droplet surface. Molecules that were dissolved in the droplet can attach to charges and be lifted into the gas phase by this field.[8]

Electrical arc discharge source - Instead of using a laser, a pulsed arc discharge is used to vaporise the material directly. A relatively high percentage of the clusters formed are ions, hence this method avoids the need for an ionisation region later on. Intensities can be quite high but cluster sizes are typically not very large.[2]

Ion Bombardment/ Sputtering - Heavy ions strike the target surface and remove molecules, atoms and clusters. Small clusters are produced with a wide range of ejection energies.[2]

These are but a handful of the more common clustering methods to be found in use. Others include *liquid metal ion sources* (LMIS) and *laser induced pyrolysis*. A detailed description can be found in the aforementioned references.[2,4]

2.2 Supersonic Expansion

Supersonic expansion is by far the most common and widespread method for the generation of clusters, and is also the method employed in this thesis. Kantrowitz and Grey first proposed this method in 1951.[10] Kistiakowski *et al,*[11] performed the first experimental setup and discovered just how dependent the products were on the expansion conditions.

A supersonic beam is a beam of atoms or molecules in which the central stream velocity exceeds that of the local speed of sound. It is formed by the rapid expansion and cooling of a gas across a high-pressure gradient. A nozzle is used to create this gradient between a high-pressure region and low-pressure region or vacuum. The shape of the nozzle used is very important for good cluster production. Convergent -divergent conical nozzles are favoured because there shape increases the probability of collisions as the clusters are forming in the expansion.[12]

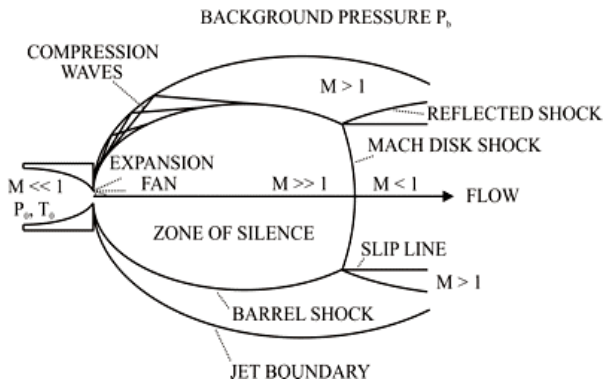

Figure 34: Supersonic expansion region.[3]

Clusters are formed in this adiabatic supersonic expansion. As the high-pressure gas expands rapidly into vacuum via the narrow nozzle, condensation starts as molecules lose most of their thermal energy. Nucleation is believed to be initiated by dimer formation – dimer formation occurs as part of a three particle collision whereby the third particle carries away excess energy released in the formation of the dimer. After the expansion the clusters grow by absorbing free molecules. Because of all the energy being released while the cluster aggregates, its temperature is higher than the surrounding gas. This surrounding gas density will decrease as the cluster moves away from the nozzle and at some point will become so low that cluster growth stops. After this the cluster can begin to cool down and evaporate monomers until the average thermal energy per molecule in the cluster is lower than the binding energy required per monomer. The predominant experimental factors that affect the condensation are nozzle size, temperature, geometry, and the type and pressure of the backing gas. In general higher backing pressure and lower temperature lead to larger clusters.[3] For rare gases, Hagena introduced the parameter Γ^* to describe the magnitude of condensation. This can be calculated from the stagnation conditions, however, relating this to the mean cluster size $\langle N \rangle$ is empirical and it would appear to vary largely on a system-by-system basis.[13] Also of note is that this parameter only applies to rare gas clusters.

Once the beam is generated the core part of the expansion, that of the highest cluster density, can be successfully collimated and extracted by appropriate use of a skimmer positioned downstream of the expansion, within a distance x_m of the nozzle,[14]

$$x_m = 0.67D\sqrt{\frac{P_0}{P_b}}$$

This corresponds to the distance necessary to avoid the shock wave (Mach disk) generated in the supersonic expansion. D is the nozzle diameter, P_b /P_0 is the background/stagnation pressure of the high/low pressure regions either side of the nozzle. This distance is typically of the order of 1 m for the setup used in this work. Thus the skimmer easily satisfies the above criteria at a distance of ~ 10 mm.

As a case study, Table 3 compares the expansion conditions used in the generation of methanol clusters by several groups. The work conducted by these groups has already been discussed in chapter 1.

Reference	Vaidyanathan[15]	Dong[16]	Morgan[i,17]	El-Shall[18]	Abu-Samha[19]	Barrett, present work.
Method	SE	SE	SE	SE	SE	SE
Pulsed(P)/ Cont(C)	C	P	P (10 Hz)	P (10-20 Hz)	P	P (5-10 Hz)
Nozzle Diam.	250 μm	200 μm	200 μm[ii]	500 μm[iii]	150 μm[iv]	200/100 μm
Nozzle Temp.[v]	298 K	Room	Room	Room	135-145 ^{O}C[vi]	Room
Carrier Gas Use	Ar/He With/without	Helium	Argon ~15% Met. Vapour	Helium	Helium	Argon
Stag. Pressure	1.47 bar	1.72 bar	<1.3 bar	2-4 bar	1.4 -1.5 bar	1.5-3.5 bar
Clusters Prod.[vii]	ArMethanol/ HeMethanol/ Methanol	Methanol	Methanol	Methanol	Methanol	Methanol
Size Regime	Small	Small	Small	Small	Large	Small
Other Notes	Ar/He flow through Methanol reservoir at room temp. Methanol vapour also used.	He flow through Methanol reservoir at room temp.	500 μs pulse widths. Expansion Chamber < 1×10^{-7}bar	100-200 μs pulse width. He flow through Methanol reservoir at room temp.	300 μm skimmer.	Clustering optimised using methanol vapour.

Table 3: Comparison of supersonic expansion conditions for the production of methanol clusters. SE = Supersonic Expansion. Small: n ≤ 20, Medium: 20 ≤ n ≤ 100, Large: n > 100.

[i] Some of these conditions found in O. Echt, P. Dao, S. Morgan and A. W. Castleman Jr., J. Chem. Phys. 82 (1985) 4076.
[ii] The impression given upon reading is that the nozzle is a straight through nozzle.
[iii] Conical 30^{o} nozzle
[iv] Conical 20^{o} nozzle
[v] Unless stated in paper nozzle temperature is assumed to be room temperature approximately
[vi] Bergesen et al (ref. 25) use same facility. Operate nozzle at 420K and reservoir heated to 320K
[vii] Clusters produced are all protonated upon ionisation with the exception of reference 26 where some unprotonated clusters are observed.

In the present setup used at National University of Ireland, Maynooth, the conditions are comparable with those of several groups in table 3, particularly Morgan *et al.*[16] The expansion is pulsed between 5-10 Hz through a conical divergent nozzle, 15^{o} opening angle, of diameter 200/100 μm with a valve pulse width of 250-550 μs. The nozzle temperature is that of the room and the stagnation pressure is in the range 1.5 - 3.5 bar. Argon has been used as a carrier gas across a reservoir of methanol. The setup will be presented in detail in chapter 3.

Note the widespread use of a carrier gas as an aid to cluster formation in the work conducted on methanol. This is not essential as clustering can occur quite well using just a vapour, however use of a carrier gas can enhance the production. The carrier gas acts to cool the growing clusters and carry off excess heat in condensation. It is important that the partial pressure of the carrier gas is not too low or too high, as in this situation it provides either an insufficient rate of collisions to aid cooling or so high that it inhibits collisions between the atoms or molecules of relevance.[2]

2.3 Fragmentation Products - Ions and Metastables

Once we have a suitable source the next step is the investigation of relevant interactions with those clusters produced. In the present work this involves the process of electron impact with the target. Using suitable detection methods we gather information about the effects of this collision by inference from its by-products. When an electron collides with a cluster there are three general processes possible, electron attachment (dissociative electron attachment), excitation, and ionisation. In electron attachment the electron attaches to the cluster forming a transient negative ion, which can subsequently dissociate producing a range of fragments; neutrals, neutral metastables, neutral radicals and negative ions are all possible. If the electron does not attach, yet is not energetic enough to ionise, the electron may still excite the cluster. This excited cluster is then a neutral metastable particle. This particle can remain in an excited state until detection, or decay into its dissociative products, neutral and neutral metastable particles. Finally, for an energy above the ionisation potential, the electron interaction can cause ionisation of the cluster, through electron loss, as well as excitation of the cluster. This process

creates a positive ion, which could potentially dissociate into a positive ion and a neutral or neutral metastable particle.

Thus from electron impact interactions with clusters we can be left with neutrals (including radicals), and negative and positive ions, in excited or ground state configurations. It is only from these products, including the electrons, that we can extract information on the interaction. Neutral species in the ground state are very difficult to detect. The ions can be detected and resolved into mass spectra, in our case using a reflectron time of flight mass spectrometer, while the metastable (long lived excited state) products can be detected using a channeltron detector arrangement, again applied in a time of flight technique.

2.4 Ion Detection – Time-of-Flight Mass Spectrometry

Mass spectrometry is the resolution of an assembly of particles by their mass to charge ratio. It first relies on having ions that can be manipulated through appropriate electric fields. These fields can be used to resolve in two manners, either by filtering all but the relevant mass, as in a quadrupole mass filter, or to derive the mass spectrum by transforming the time taken to traverse some path, as in a time of flight mass spectrometer. This second method requires the used of a pulsed source. Time of flight mass spectrometers operate on the principle that when an ion of mass m and charge q is accelerated through a potential difference V it acquires a velocity,

$$v = \sqrt{\frac{2qV}{m}}$$

By applying a suitable field E across the region in which the positive ions have just been produced, these ions will be accelerated. Though they will all acquire nearly the same kinetic energy, their velocities will depend on their mass to charge ratio. After acceleration these ions traverse a field free region, and by their arrival times it can be established what mass/charge species are in evidence, with the smallest ratio particles arriving earliest. Mass spectrometric methods have been extensively reviewed.[20,21] Some recent developments in time-of-flight techniques include velocity slice imaging,[22]

and cold target recoil ion momentum spectroscopy (COLTRIMS).[23] Here I will only contribute a brief description of the reflectron time-of-flight mass spectrometer, which is the instrument used in this work.

The reflectron TOF mass spectrometer is similar to a linear time of flight mass spectrometer, but it incorporates a reflector electric field region that reverses the ions path, making them traverse the field free region a second time. As well as enhancing resolution by virtue of a longer flight path it does so by other means also. If two ions of the same *q/m* ratio enter the reflector, yet one has a slightly higher velocity (on account of velocity distribution following ionisation), the faster one will penetrate deeper into the reflector before it is turned around (figure 35). This acts to focus a group of ions with the same *q/m,* and a velocity distribution Δv, such that they will leave the reflector in reverse sequence, with the same velocity spread. By the time they are detected they are in closer temporal proximity, providing second order focussing in time. Mamyrin invented this method in 1966,[20] and it has since become is a well established technique.

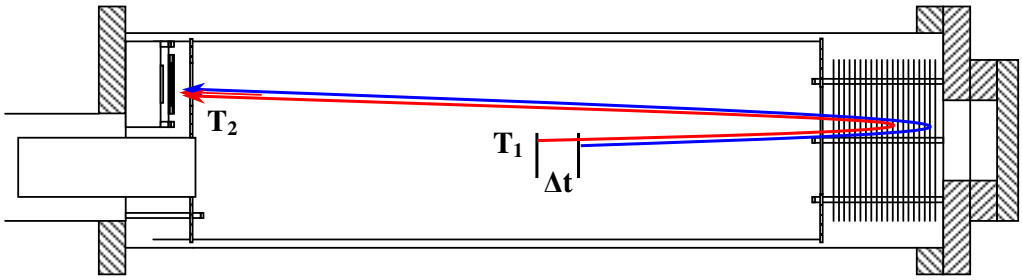

Figure 35: Time of flight mass spectrometer. Ions are accelerated from collision region (left) into field free flight region. Path is reversed by reflector electric field before re-traversal of flight tube and detection. For an initial velocity spread that leaves two ions (red/blue) spatially separated the reflectron acts to focus and narrow this distribution upon reaching the detector.

2.5 Time-of-flight Detection of Neutral Metastable Fragments

Neutral atoms, molecules and atomic/molecular clusters can all be found as by-products of electron impact. These fragments can be detected when they hit a metal surface, by virtue of the release of an electron from the conduction band, provided the fragments are in metastable or high-lying Rydberg states. The term metastable is quite loose as regards time (typically $\tau \geq 10^{-4}$ s), but generally a species is considered to be so if it exists long enough to be detected, i.e. their natural lifetime exceeds the time of flight in a piece of detection apparatus. Rydberg atoms and molecules fall into this category. They have one electron that has been excited to an orbital of high quantum number *n,* are relatively stable with energies just below threshold. In order to be detected the excitation energy of the metastable must also exceed the work function of the metal surface prepared for detection (of typically 8 eV, but lower for specially prepared surfaces).[24] These neutral particles cannot be accelerated using electric fields to distinguish masses, yet by combining a neutral detector with a time of flight scheme we can see arrival times that are proportional to the velocity and kinetic energy acquired in the fragmentation process. Further information is acquired, regarding fragmentation, by measuring kinetic energy spectra as a function of electron impact. An increase in the yield of metastables can indicate the onset of a fragmentation process for a given impact energy, and the rate of increase, or slope of *dN/dE* as a function kinetic energy distribution can provide information about the fragmentation process i.e. whether it is derived from a repulsive excited state or from the repulsive curve of a bound excited state (figure 36).[25]

Few studies have been undertaken on neutral metastable cluster fragments produced by electron impact. Of these studies conducted, some have looked at rare gas clusters (Ar, Xe),[26,27] as well as N_2O and CO_2 molecular clusters.[28] The detection of neutral metastables has been far more extensively used in electron and photon impact dissociation studies of molecules. Over thirty molecules have been examined in this manner, including N_2, H_2O, CO_2 and CH_4.[29,30]

The design, development and implementation of a neutral metastable detector forms part of the work conducted in this thesis and will be discussed in chapter 3 and chapter 5.

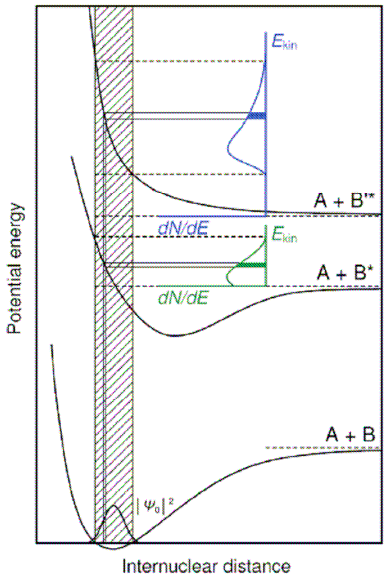

Figure 36: Illustration of two types of dissociation processes and the associated kinetic-energy distributions of the metastable fragments. The illustration is for a diatomic molecule AB, and B* indicates an atom in a metastable or high-Rydberg state. (Adapted from figure 1 of reference 25.)

2.6 References

[1] H. Haberland, "*Clusters of Atoms and Molecules*" Vol. 1 Springer-Verlag, Heidelberg (1994)

[2] H. Pauli, "*Atom, Molecule, and Cluster Beam II*" Springer-Verlag, New York (2000)

[3] G. Scoles, "*Atomic and Molecular Beam Methods*" Vol.1 Oxford University Press, NY (1988)

[4] R. L. Johnston "*Atomic and Molecular Clusters*", Taylor and Francis, London (2002)

[5] P. Sobocinski, S. Bari, J. Postma, F. Alvarado, R. Hoekstra, B. Manil, J. Rangama, V. Bernigaud, B. A. Huber and T Schlatholter, *J. Phys. Conf. Series* **101** (2008) 012006

[6] C. J. Apps, N. E. Watt, and J. C. Whitehead, *Israel Journal of Chemistry* **37** (1997) 419

[7] T. Bergen, X. Biquard, A. Brenac, F. Chandezon, B. A. Huber, D. Jalabert, H. Lebius, M. Maurel, E. Monnand, J. Opitz, A. Pesnelle, B. Pras, C. Ristori, and J. C. Rocco, *Rev. Sci. Inst.* **70** (1999) 3244

[8] J. B. Fenn, M. Mann, C. K. Meng, S. F. Wong and C. M. Whitehouse, *Science* **246** (1989) 64

[9] S. Liu, S. Brøndsted Nielsen, and P. Hvelplund, H. Zettergren and H. Cederquist, B. Manil and B. A. Huber, *Phys. Rev. Lett.*, **97** (2006) 133401

[10] A. Kantrowitz, J. Grey, *Rev. Sci. Inst*. **22** (1951) 328

[11] G. B. Kistiakowski and W. P. Slichter, *Rev. Sci. Instr*. **22** (1951) 333

[12] H. Pauli, "*Atom, Molecule, and Cluster Beam I*" Springer-Verlag, New York (2000)

[13] O. Hagena and W. Obert, *J. Chem. Phys*. **56** (1972) 1793

[14] H. Ashkenash and F. S. Sherman, *Proc. 4th Int. Symp. Rarefied Gas Dynamics* Vol.2, Academic Press, New York (1966)

[15] G. Vaidyanathan, M. T. Coolbaugh, W. R. Peifer and J. R. Garvey, *J. Chem. Phys.* **94** (1991) 1850

[16] F. Dong, S. Heinbuch, J.J. Rocca and E.R. Bernstein, *J. Chem. Phys.* **124** (2006) 224319

[17] S. Morgan, R. G. Reese, and A. W. Castleman, Jr., *J. Am. Chem. Soc*. **111** (1989) 3841

[18] M. El-Shall, C. Marks, L.W. Sieck and *M*. Meot-Ner, *J. Phys. Chem*. **96** (1992) 2045

[19] M. Abu-Samha, K. Børve, J. Harnes, and H. Bergersen, *J. Phys. Chem. A*. **111** (2007) 8904

[20] C. Weickhardt, F. Moritz and J. Grotemeyer, *Mass Spec. Rev*., **15** (1996) 139

[21] B. A. Mamyrin*, Int. J. Mass Spect*., **206** (2001) 251

[22] B. Whitaker (editor), "*Imaging in Molecular Dynamics, technology and applications"*, Cambridge University Press (2003)

[23] J. Ullrich (editor), "*Ten Years of Cold Target Recoil Ion Momentum Spectroscopy and Reaction Microscopes*", (Max-Planck-Institut fur Kernfysik, Heidelberg, Germany) (2004)

[24] H. Hotop, "*Detection of Metastable Atoms and Molecules", Experimental Methods in Physical Sciences*, Volume 29B, Ed. F. B. Dunning and R. G. Hulet, Academic Press (1996) 191

[25] E. C. Zipf, in "*Electron-Molecule Interactions and their Applications*", Vol.1 Acad. Press (1984)

[26] P. J. M van der Burgt and J. W. McConkey, *J. Chem. Phys,* **102** (1995) 8414

[27] C. P. Malone, W. Kedriewski, J. W. McConkey, *J. Phys. B: Atom. Mol. Opt.* **36** (2003) 3607

[28] C. P. Malone, W. Kedriewski, J. W. McConkey, *J. Phys. B: Atom. Mol. Opt.* **33** (2000) 4863

[29] R. S. Freund, "*Rydberg States of Atoms and Molecules*", Cambridge University Press (1983)

[30] J. W. McConkey, C. P. Malone, P. V. Johnson, C. Winstead, V. McKoy, I. Kanik, *Physics Reports* **466** (2008) 1-103

CHAPTER 3

Experimental Apparatus

3.1 Overview of Setup

The content of this chapter will include a description of the apparatus, explaining how it operates, as well as a summary of any modifications and implementations that have been made to the setup as part of this thesis, highlighting certain advances upon earlier configurations.[1,2] Descriptions of tests conducted on these implementations will be given in chapter 5. A description of the interfacing and timing scheme of the equipment is provided in chapter 4.

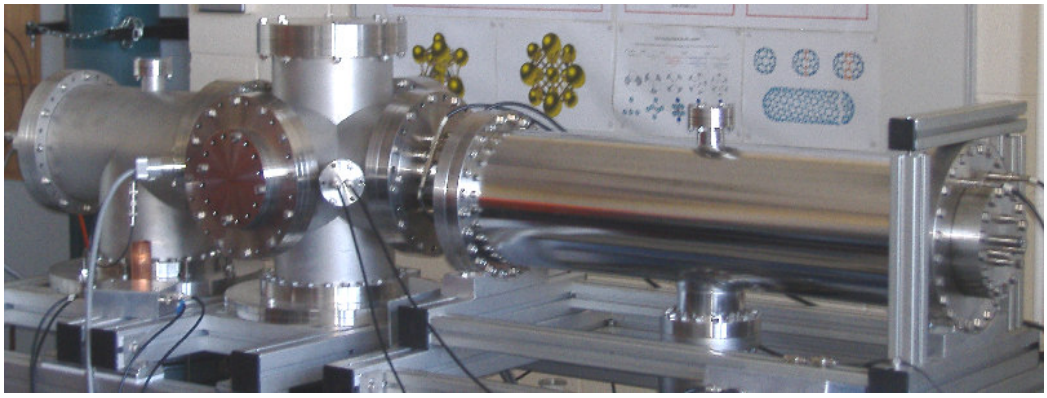

Figure 37: The cluster apparatus at the National University of Ireland, Maynooth.

The setup, shown in figures 37 and 38 consists of 3 vacuum chambers; the expansion chamber, the collision chamber, and the time-of-flight tube, which are held under vacuum by a diffusion pump, and two turbomolecular pumps, respectively, backed up by rotary pumps. Experimental events take place in the system following a timing sequence that is controlled by a digital delay generator (explained in chapter 4). A source gas or vapour (from a simple reservoir) is fed into the expansion chamber (1, see figure 38). It is contained within the pulsed valve (2) at stagnation pressure. The pulsed valve lets a burst of gas escape through a divergent nozzle into the expansion chamber, forming clusters in the subsequent supersonic expansion. The forward portion of this expansion is extracted into the collision chamber by a skimmer (3).

Figure 38: Overhead diagram of experimental apparatus setup.

1. Inlet line
2. Pulsed valve
3. Skimmer
4. Extraction grids
5. Metastable detector
6. Reflector
7. MCP detector

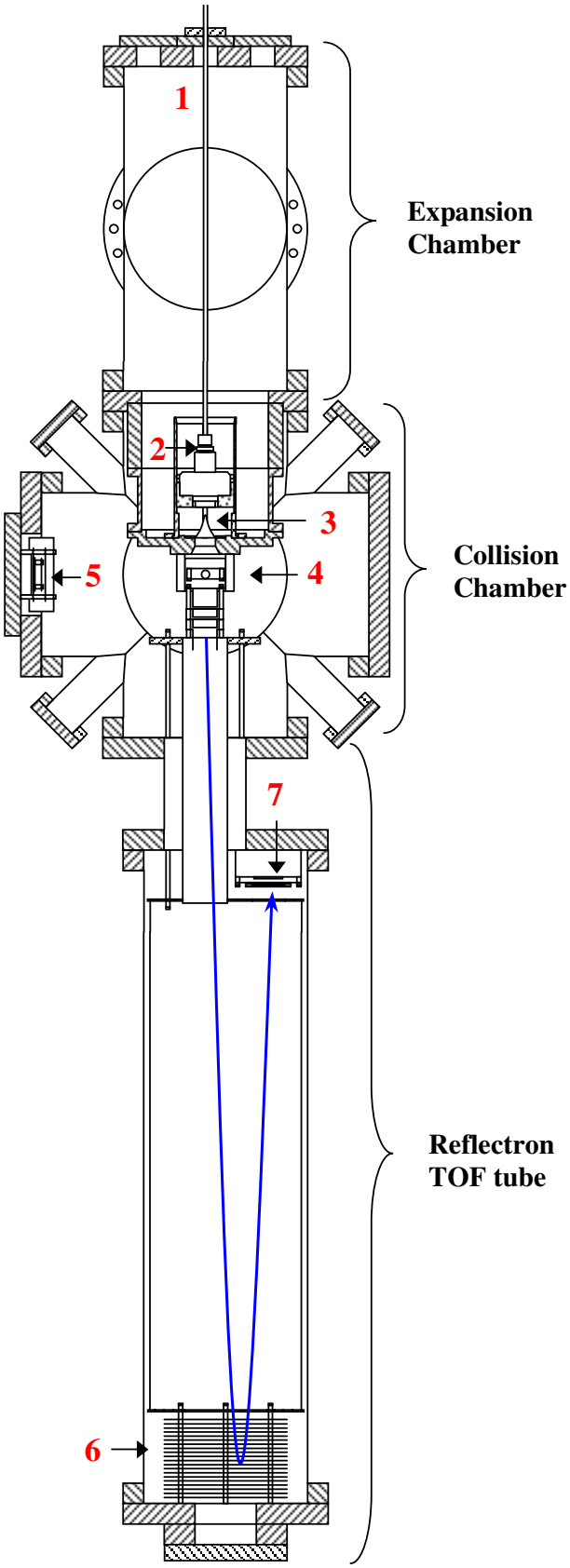

The skimmer is mounted on a top hat arrangement separating the expansion and collision chamber. In the collision chamber the cluster pulse is crossed and ionised by a pulsed electron beam. The electron gun is mounted above, and at 90^{o} to the cluster beam line. Electron impact occurs between two grids A1 and A2 (4) used to extract any ions produced into the reflectron time-of-flight tube. The extracted ions (blue line) traverse the flight tube, are turned around by the reflector (6), and re-traverse the tube before being detected by a microchannel plate (MCP) arrangement (7). Data acquisition then takes place using a multichannel scaler described in chapter 5. A channeltron metastable detector (5), for the measurement of excited neutral species, is mounted in the collision chamber, at 90^{o} to both the cluster beam and electron beam.

3.2 Expansion Chamber

In the expansion chamber clusters are generated in a supersonic expansion from a pulsed valve and collimated using a skimmer that acts to extract the forward portion of the cluster beam into the collision chamber. The chamber is held under vacuum by an Edwards E09K (2800 l/s) diffusion pump at a pressure of 1×10^{-7}mbar, however under pulsing of the valve the pressure increases to 2×10^{-5}mbar. Gas or vapour is fed to the valve by a tube that passes through the back flange of the chamber via an o-ring seal. The valve is mounted in a Teflon holder that slides into a circular brace. The brace is attached to a top-hat arrangement that also holds the skimmer (see figure 40). Alignment of the valve and skimmer, as well as the electron gun, which is mounted on the opposite side of the top hat, is ensured by this configuration. Two valve types have been tested for cluster generation as part of this thesis (results of these tests can be found in chapter 5). The original valve used was a Series 9 solenoid valve from General Valve Corporation (diameter 0.5mm). The nozzle arrangement for this valve is displayed in figure 39. This valve has been found to be inferior in producing clusters compared to the Lasertechnics model LPV pulsed valve currently employed, mainly on account of the difference in size of the nozzles employed.

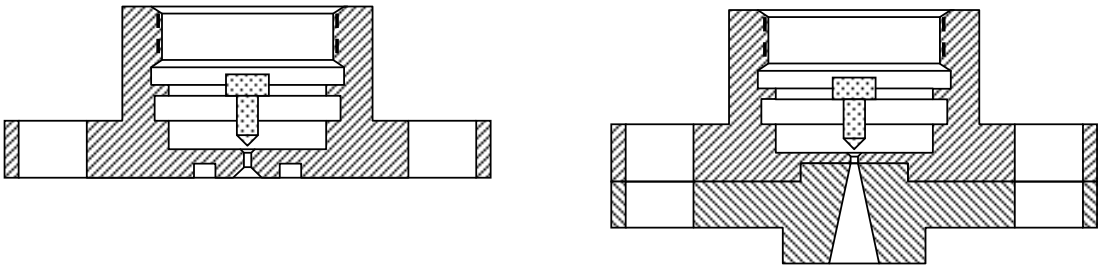

Figure 39: Un-adapted (left) and adapted nozzle (right) arrangement of the Series 9 solenoid valve. The length of the divergent part of the nozzle was extended by the lower element.

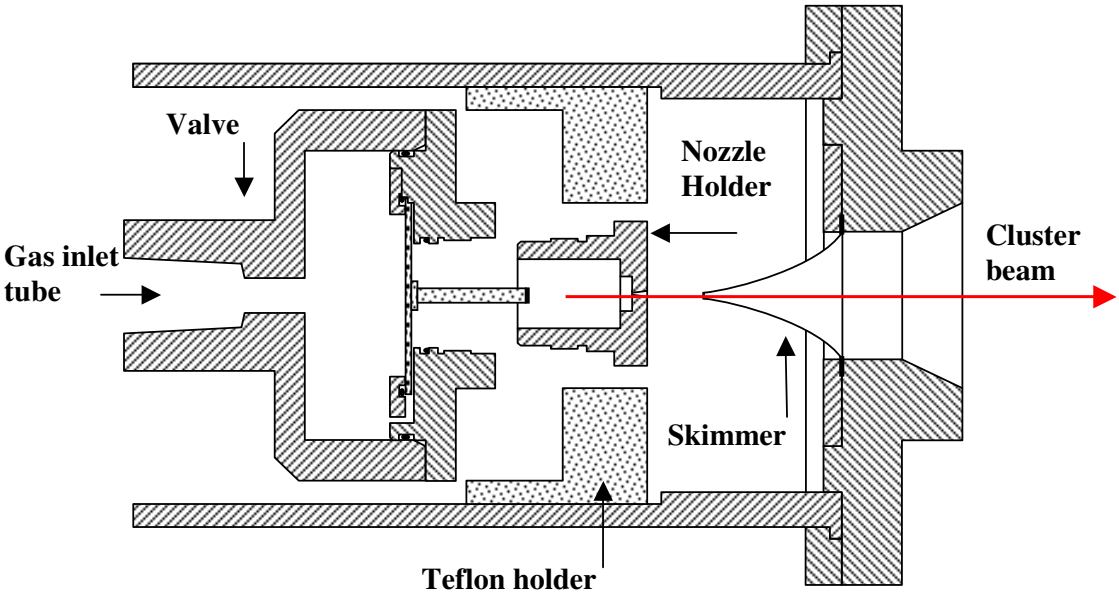

Figure 40: Semi-exploded schematic of Lasertechnics LPV pulsed valve, the supersonic expansion and the skimmer region.

This valve operates by applying a voltage (+100 - 150V) to one side of a piezoelectric bimorph disk mounted in the valve. Upon application of this voltage the disk flexes, drawing back an aluminium piston, tipped with a Viton seal, opening the valve. The valve can operate up to 150 Hz however it is only used in the range 5-15 Hz in this work, for pulse widths of 150 - 550 μs. Because only a 0.3 mm conical nozzle and a 0.1mm straight through nozzle were available with this valve (which is no longer manufactured), it was decided to drill out the 0.1mm nozzle and mount a separate 0.2mm conical nozzle into the opening obtained. The nozzle used is a conical/divergent nozzle of diameter 0.2mm from Agar Scientific. This is inserted and press-held into the

body of the original LPV valve nozzle by a circular aluminium plate, the arrangement shown in figure 41. The original valve nozzle is screwed into the body of the valve, against the piston, its tightness adjustable. The nozzle to skimmer distance is also adjustable; as part of this work the distance is ~ 7mm (subject to nozzle depth in valve seat). By increasing this distance we can focus the cluster beam more, but only by sacrificing cluster flux into the collision chamber. The skimmer used to collimate the beam has an orifice diameter of 1.2mm and a base width of diameter 22.9mm.

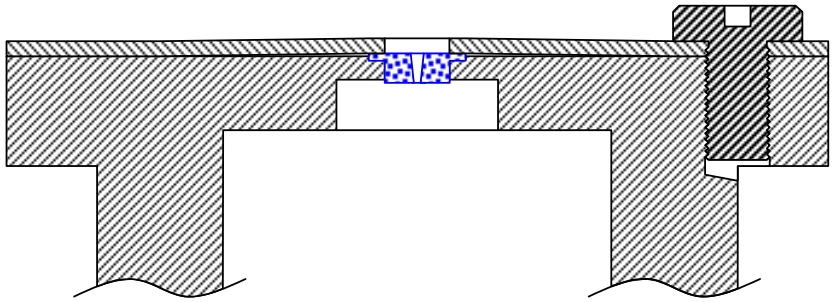

Figure 41: Nozzle arrangement for mounting of the Agar Scientific 0.2mm nozzle (blue dots) onto the original LPV valve nozzle.

3.3 Collision Chamber

The collision chamber is held under pressures of 1×10^{-7}mbar by a Leybold Turbovac 361 turbomolecular pump. Under pulsed operation of the system the pressure does not exceed 1×10^{-6}mbar. The chamber contains the electron gun (described in section 3.4) used for ionisation and interaction studies, the extraction grids A1 and A2, and a Faraday cup mounted directly beneath the electron gun for monitoring of currents. These elements are mounted on the top hat, in what is known as the interaction region, shown in figure 42 and figure 43. The chamber also contains the neutral metastable detector (described in section 3.6), which is mounted on a chamber flange at 90 degrees to the direction of the electron beam and the cluster beam.

Clusters enter the chamber through the skimmer entrance to the left of the interaction region. When the clusters are between the grids the electron beam is pulsed, ionising and fragmenting the clusters. The electron beam is collected by the Faraday cup,

consisting of an inner and outer cup, located beneath the grids. Optimising the beam alignment and focus is achieved by maximising the ratio of current on the inner and outer cup. These currents are measured using two Keithley 610C ammeters. Ions are extracted by pulsing of the grids A1 and A2. In operation A1 is kept at +100V while A2 is held at ground. Before the electron beam is pulsed A1 is dropped to ground so there is no field between the plates. After the electron beam pulse has ionised the clusters the voltage on A1 is restored and the ions are repelled into the reflectron TOF region. (The voltage on A1 is provided by an ITAR power supply, manufactured by Jordan Incorporated.)

The neutral metastable detector collects neutral metastable fragments produced and deflected by 90 degrees from electron interactions with clusters. In this time-of-flight mode of detection the grid A1 is held at ground.

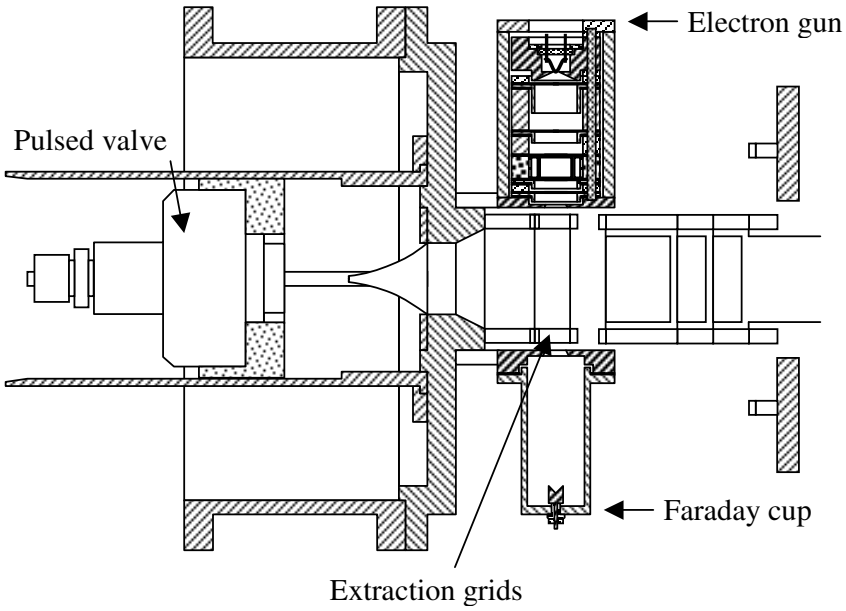

Figure 42: Interaction region of collision chamber. The electron gun, extraction grids A1(left) and A2(right), and faraday cup are mounted on the top hat arrangement separating the collision chamber from the expansion chamber. On the right is the einzel lens arrangement discussed in section 3.4.

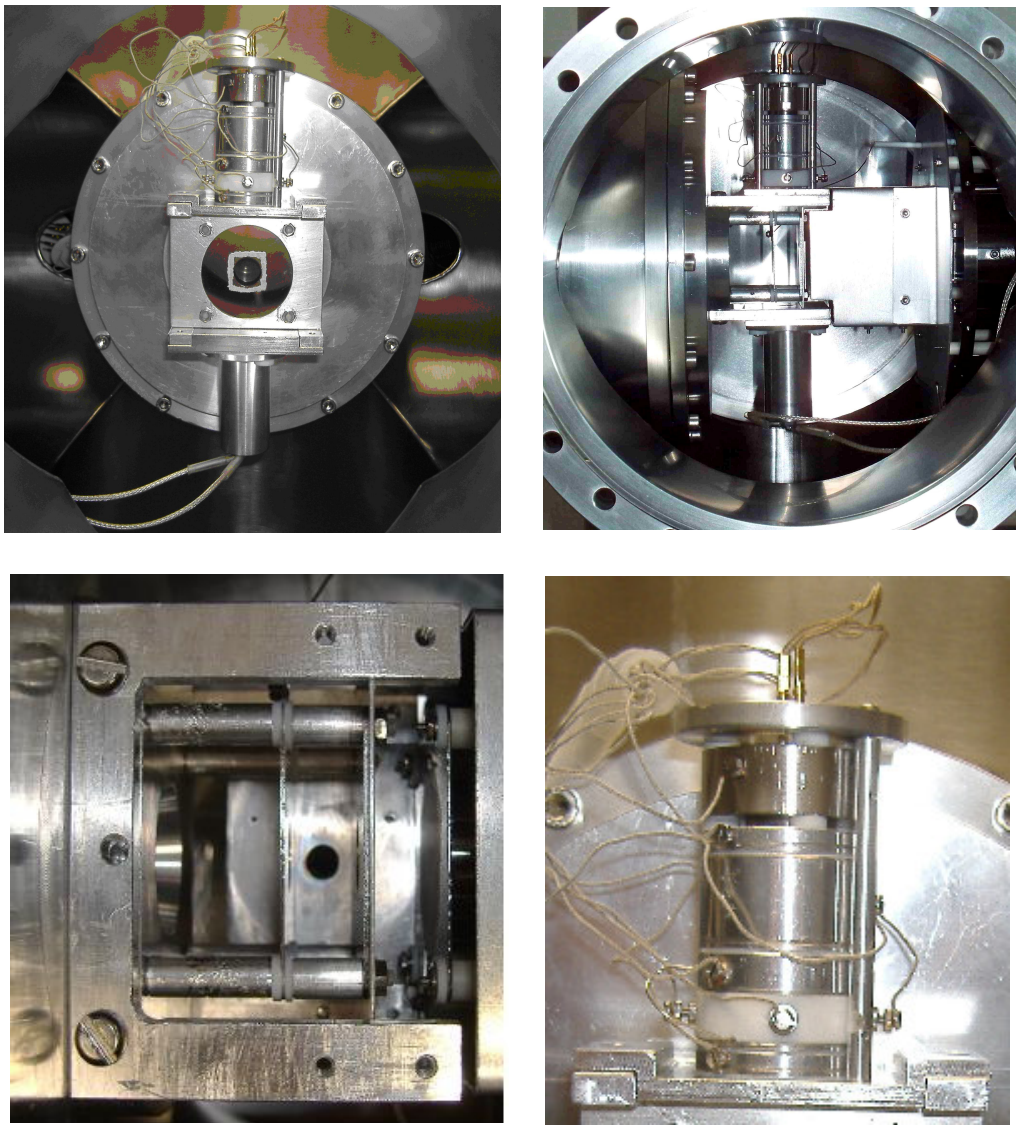

Figure 43: Interaction region of collision chamber. Top left: Frontal view of electron gun (top), extraction grid (middle), and Faraday cup (bottom) arrangement. Top right: Side view of interaction region. Bottom left: Overhead view of interaction region featuring U-bracket mounting of electron gun, extraction grids A1 and A2, and entrance to Faraday cup. Bottom right: Close-up view of electron gun, featuring Teflon deflection element (white).

3.4 Electron Gun and Deflection System

3.4.1 Electron Gun

The electron gun (figure 43 and figure 44) consists of a grid and 4 lens elements to focus the beam. It also features a deflection system (section 3.4.2), implemented as part of this work, that allows fine tuning of the electron beam alignment. The filament current is typically set to 2.2A and a voltage of 2.72V. Held at a very slight negative voltage, the grid element, V_{GRID}, squeezes the electrons into a beam before they enter the rest of the electron gun. The lens element voltages, V_1, V_2, V_3, V_6, are variable, permitting focussing of the beam. These voltages are set via an external voltage control box. A KEPCO APH 500M supplies 300V to a potential divider network within this control box, which is then distributes to the lens elements. Suitable settings for these lens elements are provided in chapter 5. The electron impact energy is controlled externally by a separate programmable KEPCO APH 500M power supply. A LabVIEW interface has been built for this control function (chapter 4). The actual energy is determined by the potential difference between the filament tip and the target region that is held at ground. For the best achievable settings it will be shown (chapter 5) that the e-gun has good stability for an operational range of 15 – 200 eV.

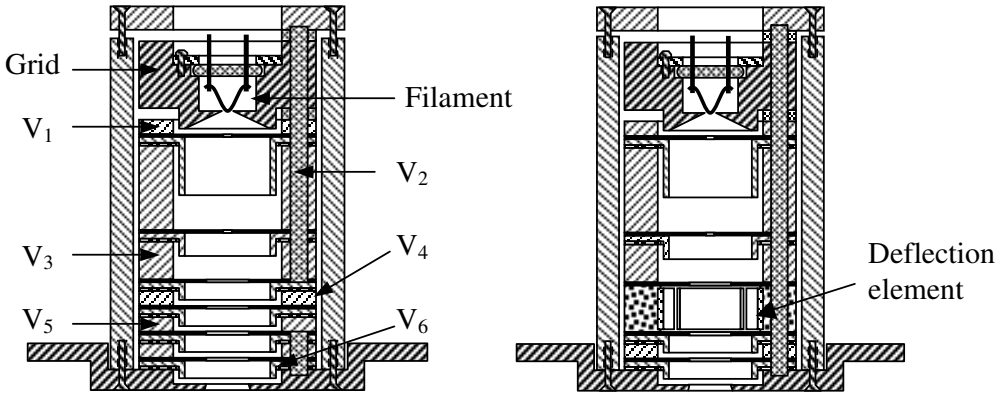

Figure 44: Previous electron gun arrangement (left). Present electron gun arrangement (right).

3.4.2 Deflection System

The electron gun deflection system was largely introduced to allow steering of the electron beam across the cluster beam, permitting the region of highest cluster yield to be used in experiments.

In order to implement the deflection system alterations had to be made to both the original gun and the voltage box responsible for its control. The previous electron gun consisted of a grid and 6 lens elements, (figure 44 (left)). To incorporate the deflection system, the element of the previous electron gun, V_4, had to be removed to make space for the deflection element itself. This also freed up an extra two inputs on the 11 pin vacuum feedthrough required for the new up, down, left, right elements, for which there were already two free inputs. The choice of which lens element to remove was made by testing for the element with the least negative effect on focussing of the beam upon its removal; the fourth element was chosen. The replacement deflection element, a Teflon ring with four inner orthogonal plates for deflection has deflection voltages about the voltage V_3. The element previously at V_5 would now be kept at V_3 (achieved by a short connector wire). The two inputs now freed up (V_4, V_5) could be used for two deflection voltages.

The voltage box is a unit that allows control of all electron gun voltages via a potential divider network. It also allows checking of the voltages while the gun is in operation. For the electron gun deflection system to work extensive changes had to be introduced to the voltage box with substantial rearrangements to the electronic circuitry and the basic layout. A diagram of the revised circuit can be seen in figure 45.

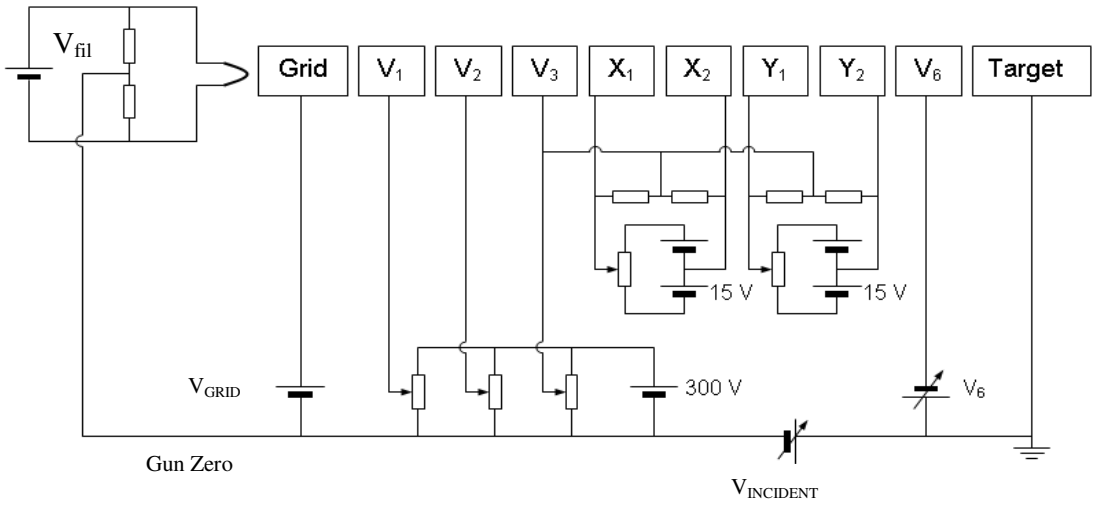

Figure 45: Schematic diagram of the revised potential divider network used in voltage control of the electron gun lens elements.

The power required for the deflection system was +/-15V DC. This was provided by two EPSD 15/200C AC-DC converters from VxI Power Limited. They provide both +15 and -15 Volts and require 230 V AC input voltage. The setup works quite well with the potentiometer allowing variance of the deflection voltage from +15 V to –15 V across each pair of deflection plates, evident by monitoring the improvement in Faraday cup currents upon steering of the beam.

Tests were conducted to see if the electron gun would maintain stability to lower energies by suitable variance of a programmable $V_{6,}$ as a function of the incident energy V_{inc}. These tests showed little improvement in stability and therefore the measurements presented in this report were all performed with a fixed voltage V_6.

3.5 Reflectron Time-of-Flight Region

A Leybold Turbovac 361 turbomolecular pump is used to maintain vacuum in the time-of-flight chamber. The reflectron setup is shown in figure 47. Ions are repelled into the reflectron TOF region by the grid A1. They first pass through an Einzel lens arrangement, where the first and third elements are held at –1200V, while the middle one, V_{FOCUS}, is set to –1400V. It is this voltage that provides primary focussing of the ion beam. In order for the ions to reach the detector they must be deflected slightly before traversing the flight tube. This is achieved by setting V_{DEF} = XY1 to –1140V with respect to the other deflection plate XY2 which is at –1200V. This was found to be the optimal value by experiment (chapter 5). The voltages used in the reflector are critical to providing second order focussing, and were re-determined using the theoretical approach discussed in Lynch.[1] The optimal values are V_{R1}= -374V and V_{R2} = +83. A resistor divider network spreads the strength of the electric field in the reflector uniformly across 18 plates and grid apertures, figure 46 (left). The flight tube features a liner, figure 50 (right), held at –1200V, that is insulated from the exterior chamber. At the end of their flight path the ions are detected by a microchannel plate (MCP) detector, operated at –3700V. This voltage is divided across two chevron plates in the MCP such that the voltage never exceeds 1000V across any one plate. The reflectron used in this thesis was manufactured by R. M. Jordan Company in California.

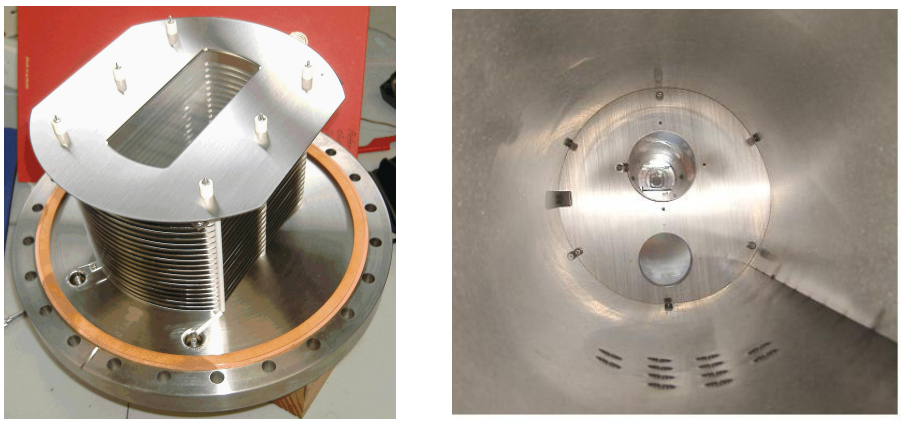

Figure 46: Left - Reflector grid elements of the TOF mass spectrometer. Right – TOF chamber as viewed from the reflector end. The top hole is the exit from the collision chamber, the bottom hole is the entrance to the MCP detector.

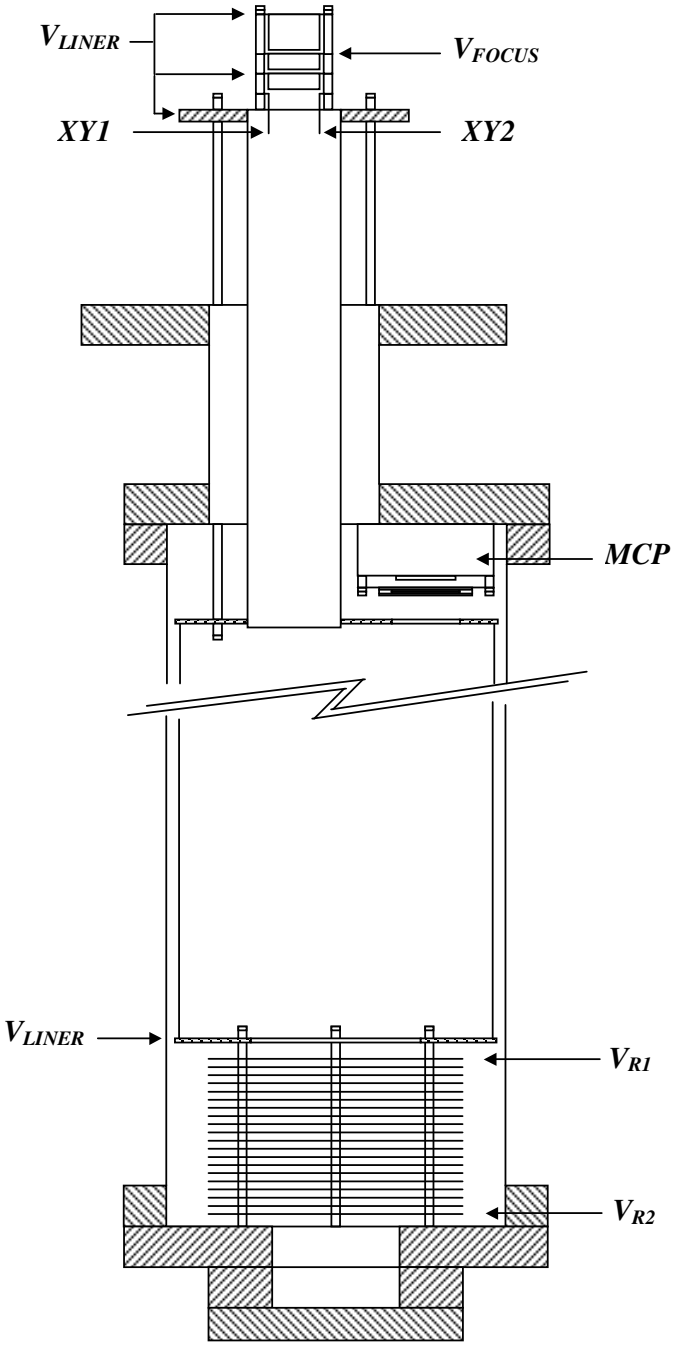

Figure 47: Schematic diagram of the reflectron.

3.5.1 Microchannel Plate Detection Efficiency

For an ion to be detected by the MCP detector, secondary electrons must be released from the surface of the first plate in the detector. The secondary electron emission rate is dependent on the velocity with which the ion strikes the surface, with no electrons released if this velocity does not exceed some threshold value.[3] For clusters this leads to a lower probability of ion detection for higher *n* on account of larger size clusters reaching the detector with a lower velocity. Studies on large argon clusters have shown that the relative detection rate does indeed vary significantly, with very distinct regimes of decrease, as observed in figure 48.[4]

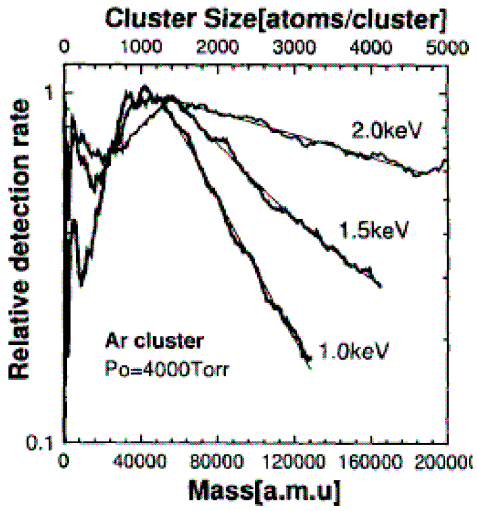

Figure 48: Dependance of relative detection rate on cluster size.[4] Shown with logarithmic scale.

The study also shows that this decrease in detection rate can be compensated by an increase in the acceleration energy of the ions.

In the Maynooth experiment, a significant increase of the voltage on the front of the microchannel plate is not possible, because of limitations imposed by the voltage ratings of the electrical vacuum feedthroughs and the maximum voltage across each of the microchannel plates.

3.6 Neutral Metastable Detector

A neutral metastable detector has been constructed for detection of neutral metastable particles ejected from the electron collision process. Fragments fly to the detector (at right angles to the electron beam), where positively or negatively charged elements are repelled; neutral elements are detected through Auger de-excitation on the surface of the channeltron, freeing electrons. The electrons emitted from the surface are accelerated and multiplied down the channeltron forming a charge distribution (pulse) that can then be extracted via a de-coupling circuit and resolved and counted using a discriminator – amplifier – counter setup.

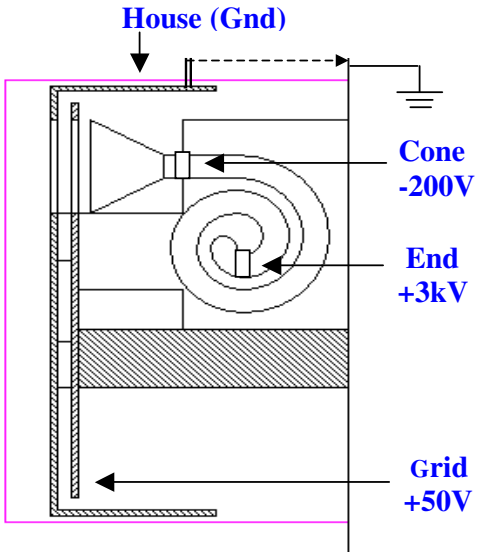

Figure 49: Schematic of metastable detector from the side.

In designing the metastable detector the key constraint was geometric; it needed to fit at the back of the reflectron as an optional position.

The detector was designed such that the cone of the channeltron is 23mm away from the center of the flange on which the detector is mounted. This was done to allow the possibility for mounting at two different positions: (1) in the collision chamber at exactly 90^{o} with respect to the cluster beam and nearly 90^{o} with respect to the electron beam, and (2) behind the reflector at the end of the time-of-flight chamber. The second position is useful for time-of-flight measurements of neutral excited clusters in order to

establish the forward velocity of the cluster beam (a measurement of this kind is planned in the near future). The detector is mounted on a flange that has four connectors. It has two BNC connectors, one for putting –200V on the cone to repel negative ions – electrons largely, the other for putting the grid at +50V to repel the positive ions, and two MHV connectors, one spare, and one for putting up to 5kV on the channeltron end. The manner of the connections can be seen in figure 50 (Teflon coated wires) as can the form of construction. The holder is made of Teflon with the house and grid fabricated from aluminium. In order for the particles to get to the detector there is a hole the width of the cone in both the House and Grid. This hole is covered with a fine gold wire mesh that was constructed by weaving about a stamp shaped frame, figure 50 (bottom left), and held by pressed contact against the House surface.

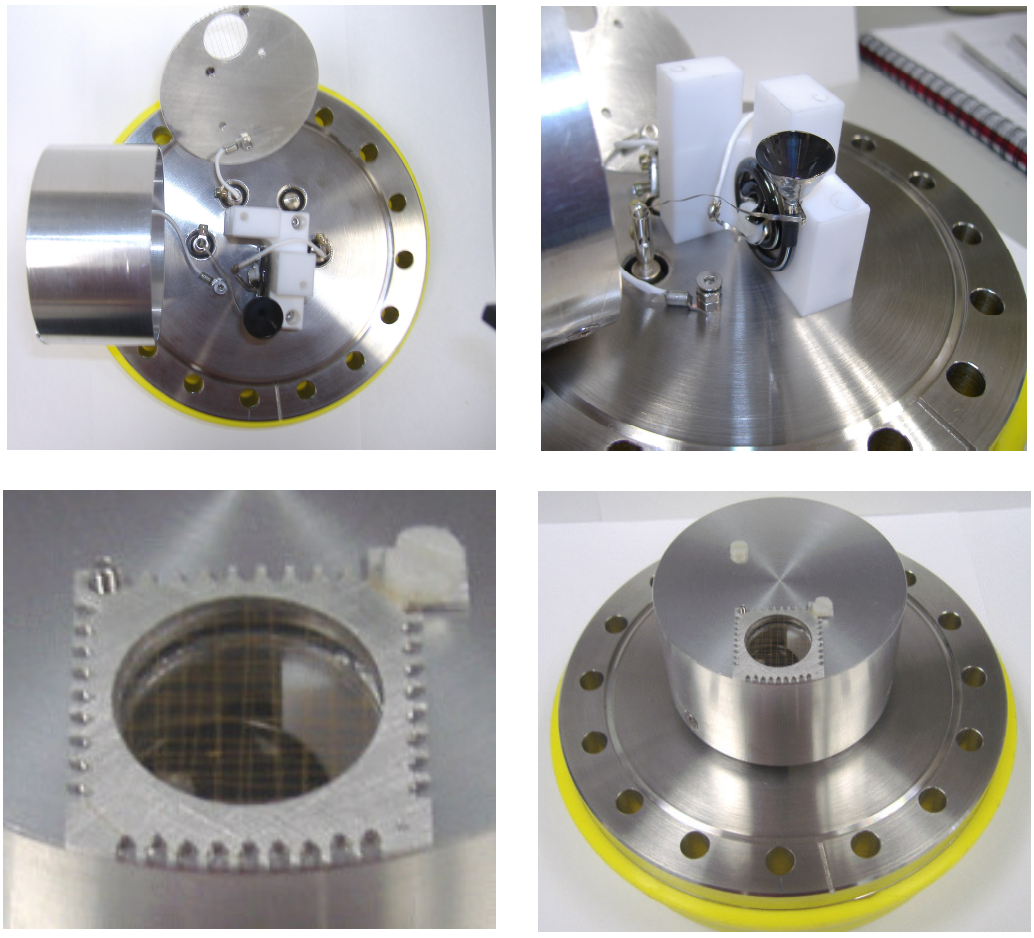

Figure 50: Assembly and connections of the metastable detector. Top left and right: Inside of open detector. Bottom left: Gold wire mesh covering entrance to detector. Bottom right: Detector ready for mounting in vacuum.

This was all home built (excepting channeltron), as was the decoupling circuitry (figure 51). In building the electronics the one major constraint was that the circuit had to fit into an aluminium box of dimension 5×5×3cm. This box has two outputs on its lid, one for input of MHV, and the other for output of BNC decoupled pulse signal from the detector. The circuit was built upon Vero board strip, and because of the high voltages involved the components used were 2Watt resistors and 3100V capacitors.

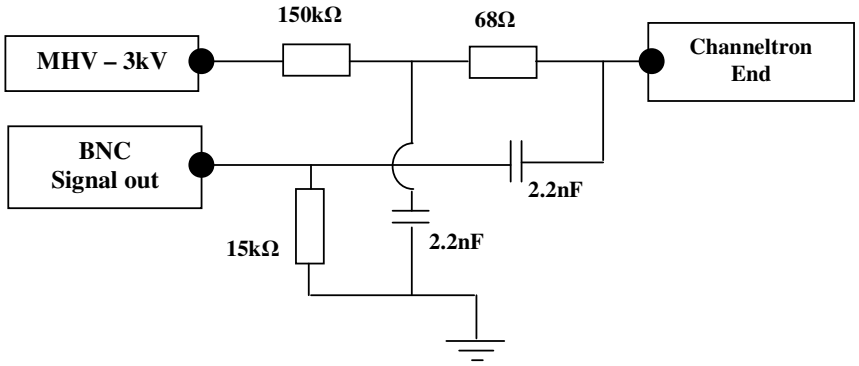

Figure 51: De-coupling circuit of metastable detector.

Tests indicate that the channeltron detector is functional and these will be presented in chapter 5.

Due to the fragile nature of the metastables being detected, it is important that any stray electric fields are eliminated from their flight path to the detector, hence the addition, to the interaction region, of the extra shielding shown in figure 52.

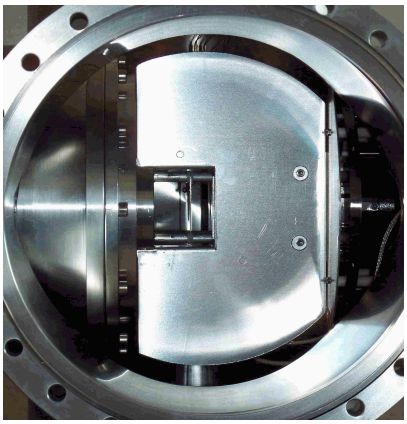

Figure 52: Shielding of electric fields for metastable detection.

3.7 Amplification and Discrimination of Detection Signals

Whether an ion is detected at the MCP, or a neutral metastable at the channeltron detector, the signal produced must undergo amplification and discrimination before data acquisition can occur at the multi-channel scaler. The setups used, figure 53, differ dependent on which of these cases we are dealing with.

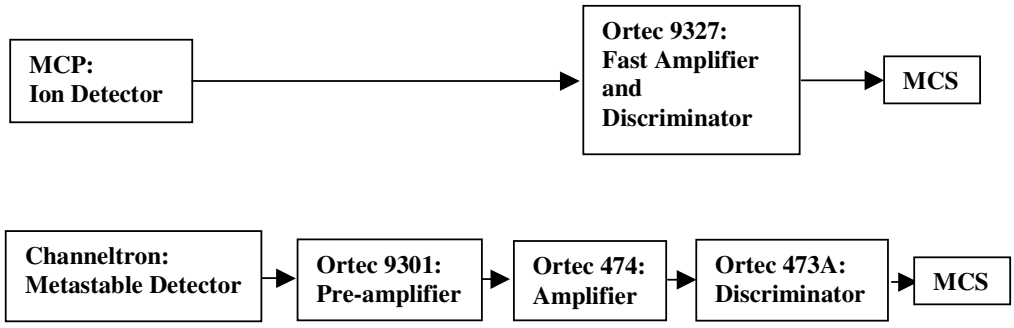

Figure 53: Discrimination and amplification routes for ion/metastable detection

The signal from the ion detector (MCP) passes into an ORTEC Model 9327 1GHz amplifier and timing discriminator unit. It can deal with pulse widths as low as 250 *ps* FWHM and is designed to handle pulses in the range 0 to –30 mV. In the current setup the NIM out signal from the 9327 is used to trigger a STOP count on the MCS. This signal is despatched whenever a signal from the MCP is received above the discriminator level. The discriminator is manually adjusted at the front of the unit, an LED indicates a detection; by adjusting this discriminator level until the LED just turns off (non-pulsing mode) noise can be eliminated.

For the channeltron detector the signal first passes through an ORTEC 9301 fast pre-amplifier. This is a small and compact unit that can be connected in close proximity to the detector, minimising noise in the signal. It has a voltage gain of 10 and is powered by both a +/-12V supply by connection to the ORTEC 474 timing filter amplifier, which provides this power output. The output signal from the 9301 pre-amplifier travels to the input of the ORTEC 474. It is used to further amplify and shape a pulse for subsequent discrimination from the ORTEC 473A constant-fraction discriminator. The gain ranges from 2 to 250. Integrating and differentiating circuits in the unit carry out the shaping

of the pulse. It has been found that the settings of coarse gain ×20 and integration of 20 *ns* produce an adequate pulse. The 473A discriminator unit outputs a NIM pulse of -0.8V to the STOP of the MCS marking detection from the channeltron, provided the signal is above the discriminator level. This is set by viewing the pulse outputs from the 473A, and adjusting the level until no noise is observed. The discriminator is operated in leading edge discrimination mode.

3.8 Modifications

The following is a brief summary of some other relevant modifications that have been made to the experiment throughout the course of this work:

1) The diffusion pump is positioned directly beneath the expansion chamber. It had an oil baffle and butterfly valve between it and the expansion chamber. Removal of both these elements enhanced pumping speed, however the introduction of oil vapour into the chamber meant the baffle had to be put back in place

2) Mounting of the extraction grid plates has been moved from the entrance of the of Einzel lens arrangement to the new mounting on the top hat with the objective of ensuring that e-gun, plates and faraday cups all have a common support and alignment.

3) Previously, the extraction voltage had operated by pulsing to ground from a negative voltage on A2, and back to negative again (-100V) to pull the ions out. This arrangement was changed in order to check the effects of a small unwanted deflection of the electron beam by the voltage on the liner of the time-of-flight tube. The deflection was subsequently remedied by more extensive shielding of the liner voltage from the collision region. Now A2 is held at ground while A1 is pulsed from positive to ground to positive, in effect pushing the ions out. Changing the polarity of the pulse required a jumper cable change to the A - D setting within the ITAR power supply box.

4) Two adjustments were made to better shield the electron beam and metastables path from the liner field. (i) The aluminium shield surrounding the Einzel lens was improved. (ii) An additional shield was added to the right of grid A2, as shown in figure 52.

3.9 References

[1] J. Lynch, *M. Sc. Thesis*, (2001) N. U. I. Maynooth

[2] E. Duffy, *M. Sc. Thesis*, (2005) N. U. I. Maynooth

[3] R. Kawakami, J. Kawata, K. Ohya, *Jap. J. App. Phys.* **38** (1999) 6058

[4] N. Toyoda, M. Saito, N. Hagiwara, J. Matsuo and I. Yamada, *Int. Conf. On Ion Implantation Technology Proc.,* **2** (1999) 1234

CHAPTER 4

Interfacing, Data Acquisition and Analysis

4.1 Overview

This chapter will describe the processes involved in taking a mass spectrum, or a time-of-flight spectrum of neutral metastable fragments. From interfacing hardware and software, to data acquisition and analysis, all the relevant exterior operations needed to obtain the relevant experimental data will be covered. In particular, this requires looking at the pulsing scheme employed (section 4.2), the means of acquisition and recording of the data (section 4.3), and the interfacing methods and software programs involved (sections 4.4 and 4.5). Data analysis is described in section 4.6.

The relevant event sequence in generating, acquiring and analysing a single time-of-flight mass spectrum is displayed in figure 54. First we setup the system to take a measurement. The operation settings of the system can be divided into three parts, those of the digital delay generator for control of the timing sequence, those that are input into a LabVIEW interface for control of the electron gun impact energy and acquisition settings, and finally all other settings, reflectron voltages, electron gun settings, detector voltages, etc, which have been discussed already in chapter 3. Once the settings are input we set the digital delay generator to run; this then commences the timing sequence and pulsing of the various elements within the system. If everything is functioning properly we then start the acquisition of a time-of-flight scan, via a LabVIEW interface designed for this purpose. It collects data from the multichannel scaler, records the data, and provides a visual display of time-of-flight spectrum.

Once the data has been recorded it is necessary to analyse the data and convert the TOF spectrum into a mass spectrum. This is conducted using code written in Matlab, a C programming language based software. Code has been constructed for a number of other tasks, including concatenation of data, peak searching and identification, as well as integration over peaks and time ranges. For fast identification of peaks and easy observation of spectra a LabVIEW program has also been built.

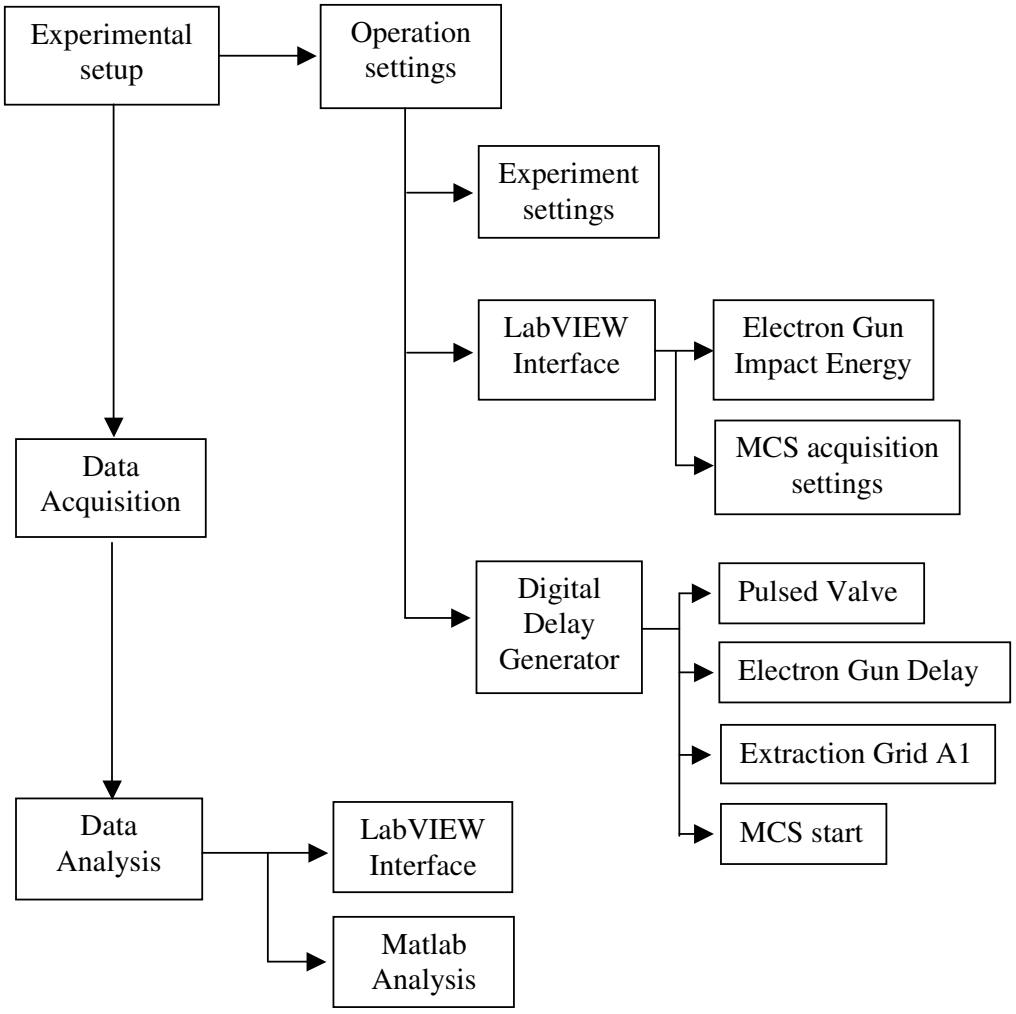

Figure 54: Operation sequences for generation, acquisition and analysis of a TOF mass spectrum.

4.2 Pulsing and Timing

In the experiment the valve pulse, electron pulse, ion extraction pulse and the trigger for the multichannel scaler all need to have the correct width and the correct delay with respect to each other. This timing sequence of the pulses used is controlled by a digital delay generator (DDG), DG535 from Stanford Research Systems. It contains a trigger, T_0 (controlled internally/externally), and has four independent delay channels, A, B, C, D, and two independent pulses, AB, CD, that can be set from 0 to 1000 seconds delay, in steps of 5 *ps* resolution, relative to T_0. The pairing of the delay outputs, A and B, C and D, is what defines the shape of the AB, CD pulses with the first delay shaping the leading edge and the second the trailing edge. Each channel can have a range of outputs; the pulse shape can be TTL, ECL, NIM, or VAR (a form where the amplitude and offset of the pulse can be set); the pulse out can be normal or inverted, and the output impedance can be either 50Ω or high. The role of each channel is shown in figures 55 and 56. This applies to the mass spectrometry case; when measuring time-of-flight spectra of neutral metastables A1 is kept at ground.

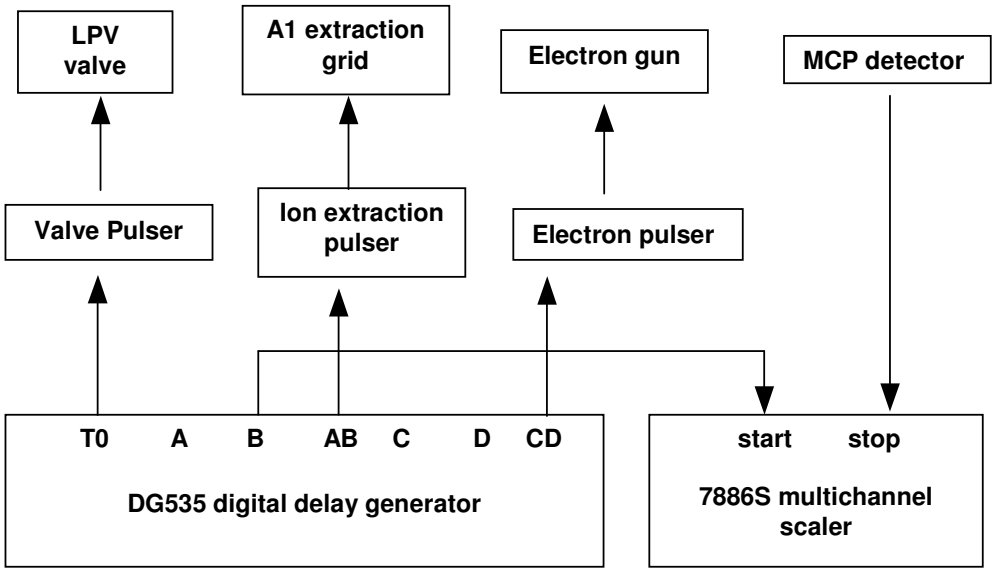

Figure 55: Pulsing setup

T_0 - All other channels are pulsed with reference to this one. It is triggered internally by the DDG, at normal rates of 10 – 20 Hz, and its output signal (50 Ω, TTL, Normal) is sent as a trigger to a homebuilt pulsing unit which then sends a pulse

of the variable width (150-550µs) and of magnitude 0 to 150V to the LPV pulsed valve. Typically the LPV valve is operated at 130V and opens for 350µs. In principle the shorter this width the better as it permits a higher repetition rate, because longer widths let more gas into the system.

AB - After a delay of typically 500µs the burst of gas from the supersonic expansion has passed through the skimmer, and is now reaching the collision region between the extraction plates. In order to ionise the clusters with an electron gun pulse first the extraction voltage on A1 grid (+100V) must be dropped to ground. After the ionisation has occurred this voltage is restored (after 1µs). This is initiated by the signal sent from the AB output, (High Z, TTL), to an ion extraction pulser unit connected to A1. By varying the delay in the onset of AB with respect to T_0 different portions of the cluster pulse can be examined and a profile can be constructed.

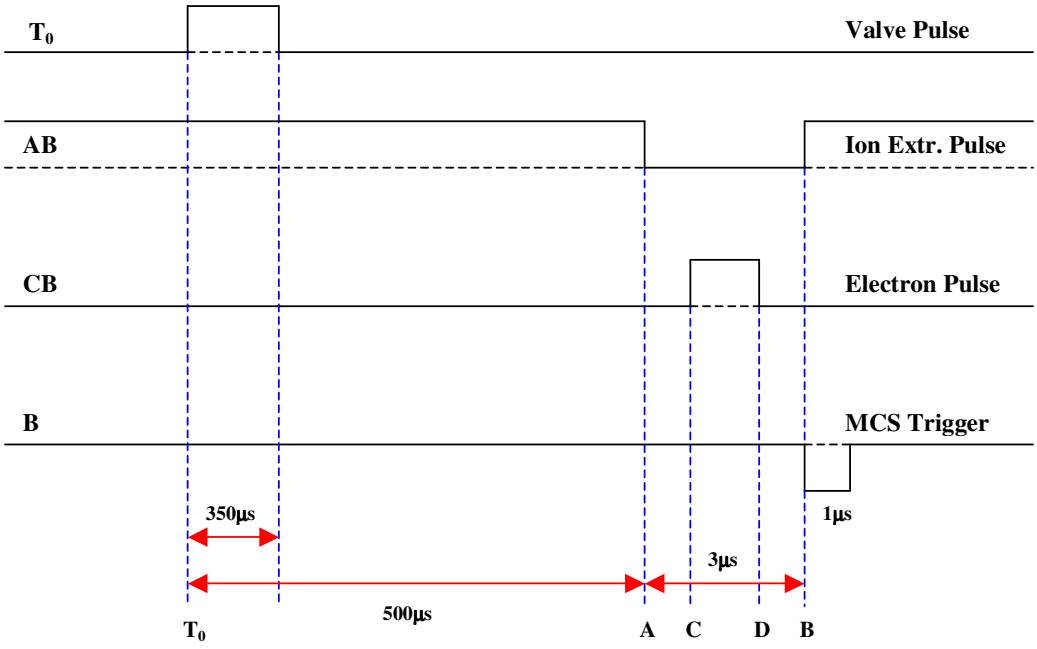

Figure 56: Pulse timing scheme

CD - Once the extraction plate has dropped to ground the electron gun is pulsed (1µs later). This is performed by an electron gun pulser box, which requires a 12V power supply for operation, being triggered by the CD output (50 Ω, TTL). This box pulses the grid element voltage, V_{GRID}, of the electron gun. This element is held at a negative voltage (-30V with respect to the zero of the gun) that repels the

electrons from the filament travelling into the gun. Upon pulsing, this voltage is increased to a slight negative voltage. Electrons can then enter the gun. This pulse has a variable width. It is normally set at 1 or 2 μs to provide the necessary time resolution for time-of-flight mass spectrometry, or time-of-flight detection of neutral metastables.

B - Upon restoration of the extraction voltage the ions are repelled into the TOF tube and then a pulse is sent from the B output (50 Ω, NIM, Inverted) triggering the start of the MCS.

For operation of the metastable detector the setup is essentially the same except that the extraction plate A1 is not connected or pulsed, but instead is held at ground; it is important that that the neutral metastables travel through a field-free region. Also, for neutral metastables detection we trigger the multichannel scalar on the leading edge of the extraction grid pulse signal, using the output from A. This gives us a reference point, provided by photons detected from the interactions of electrons with clusters.

4.3 Acquisition

The data acquisition is carried out by a 2GHz fast multichannel scaler (MCS) model 7886S, supplied by FAST ComTec. It is controlled via a server program that uses a set of functions stored in a dynamics link library (DLL) to interface and operate the MCS. MCDWIN is the name of the user interface software for controlling the server settings and displaying the data. This has been replaced by a new, more user friendly and flexible, LabVIEW interface. The 7886S is a computer card that fits into an ISA (Industry Standard Architecture) slot. The time resolution has been calibrated to 431.676 *ps* per channel, described in chapter 5. On the back of the 7886 card are a number of inputs and outputs: STOP IN, START IN, ABORT IN, SYNC OUT, DIGITAL IN, and a THRESHOLD ADJUST screw. The START IN input (fast NIM, -0.8V, 50 Ω) triggers a sweep of the MCS, upon receiving a pulse from the DDG. The signal from the relevant detector, after amplification and discrimination, is input into the STOP IN connector where it is registered as a count at the relevant binning location of the MCS. THRESHOLD ADJUST varies the discriminator level of the START, STOP and ABORT pulses.

4.4 Programmable Power Supply and DAQ Device

A programmable voltage supplied by a KEPCO APH 500 is used to control the electron impact energy. This power supply is controlled by a LabVIEW interface, which interacts with it via a National Instruments 6008 USB DAQ (data acquisition) device. The LabVIEW code will be discussed in the following section.

The KEPCO APH500 is a precision stabilised power supply, which has an operational range of 0 – 500 V, and a low current of 0 - 40 mA. It features programming terminals on the back to allow for external interfacing. These terminals allow for the programming of either the voltage or current output of the device. To control the voltage one needs to make two connections to VI IN and COM on the terminals board (terminals 6 and 10 respectively). For proper control V IN must apply a potential of 0-5V and COM just provides the common ground. This voltage is then amplified within the power supply by a factor of ten, giving the range 0 – 500 V. The analog output channel (ao0) of a NI 6008 DAQ controls this voltage.

The National Instruments 6008 DAQ is a small portable analog to digital converter device designed to connect to the computer via USB. This makes it relatively easy to connect and disconnect without the need to open the computer case, as would have been the case for previous ISA cards. The device provides four analog input channels for voltage measurements, two analog output channels and twelve bits of digital imput/output (0 or 5V). It also provides an event counter to count pulses generated elsewhere. The analog inputs can measure over a widest range of –20V to +20V while the output voltages range from 0 to 5V in 4096 steps, suitable for the precision required with the APH500. The range of operation and other functions of the 6008 are setup using a software package called the DAQ assistant provided by National Instruments. Otherwise it can be setup within the LabVIEW program used for its control. In LabVIEW this is the measurement function icon, titled DAQmx assistant, its icon shown in figure 57.

Figure 57: LabVIEW DAQ assistant icon for control of 6008 device

4.5 LabVIEW Data Acquisition Software

LabVIEW is a software interfacing package designed by National Instruments. It is a graphical programming language that targets acquisition of data, recording of data, control of external devices, data analysis and manipulation, and graphical interfaces as its main functions. Writing a program in LabVIEW requires selecting the relevant icons from a suitable palette, placing the icon on a block diagram, and wiring them together, with the data travelling along these wires from input to output. Unlike text based programming, the event execution is not in a set order, functions are executed and data is passed as it becomes available, known as dataflow programming.

Graphical code is written on a block diagram panel using icons and other graphical implements, but this is just one of two panels, the other being the Front Panel. The Front Panel is the user interface of the finished program. A completed program, with front panel and block diagram is referred to as a Virtual Instrument (VI). On the front panel are to be found controls, charts, indicators, inputs and outputs for the VI, all the elements needed to operate the program having to touch the block diagram itself.

Once a VI is created, it can then be represented by an icon, with the same number of inputs and outputs available as on its front panel. This icon can then be selected and used in another block diagram of a larger VI; the smaller VI is then referred to as a SubVI.

A property node is an icon that represents that calls on an associated value for use at another location within the block diagram. Its benefits lie in that it eliminates the running of wires across large tracts of graphical code. Several nodes with the same parent can be used, and simply changing the parent can change the value of all of these.

LabVIEW interacts with the MCS card via dynamic link library files (DLL). These DLL files contain C code written for communication with the card; this code was provided by Dr. Marcin Gradziel, and is a modified version of code supplied by FAST Comtec. The files are accessed in LabVIEW through the use of Call Library Function Nodes (figure 58). The node features inputs that are fed into the relevant function within the C code, which executes some operation with regard to the MCS. If necessary the MCS returns an output that can be extracted from the output terminal of the Call Library Function Node. In the *Scan_Acq* program described shortly two of these nodes are used, and hence two different DLL's. Both DLL's utilise the same C code (Appendix A), however they access different functions within this code. The first node is used to check if the card is initialised, connected to the PC, and ready to receive and transmit data. It is setup to access the *lw7886_init* function within the C code and returns a *true* or *false* dependant on the response. Hence it has but one input (the assignment of a base address for the device) and output. The second node used accesses the *lw7886_acq* function within the C code. It has three inputs and two outputs. It reads in the variables *range, timeout* and *sweeps* to setup the scanning conditions of the card. The input/output *buffer* is an originally empty array of data that is added upon with each sweep of the MCS, and forms the TOF spectrum upon completion of the scan. Finally there is an output, *sweeps,* of the actual number of sweeps the card performed.

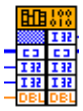

Figure 58: Call Library Function Node

Two VI's have been contructed using LabVIEW:

V_Inc_Cont.vi – A simple program that is used to control the electron impact energy (eV).

Scan_Acq.vi - The main program used in taking mass spectra and quick analysis. It consists of two separate programs on two different pages (**Page1, Page 2**), for convenience. This program's development was aided by work carried out by Mr. Liam O Connor and Mr. Michael Reid; as part of their final year physics degree project they helped develop a LabVIEW program for the acquisition single scans.

Page 1 is used for taking mass spectra or more generally time of flight scans. It is a data acquisition program that prepares the card for single or multiple sequential scans, records the data from the MCS, and allows real-time observation of the data as it is acquired and displayed on a chart. It surpasses the older MCDWIN software in that it allows smooth display and observation of the spectrum as it is being recorded, permits scales to be modified, regions to be magnified, and cursors to be used for early identification of peaks. It also allows for excitation functions to be taken by varying the electron impact energy with each scan. This is essential for taking excitation functions of ionised fragments with specific masses, or metastables with kinetic energy in a specific range.

Page 2 contains a simple program to look at recorded spectra and a cursor that when dragged over a peak will convert the TOF into a Mass/Charge ratio. Again this is useful as an early diagnostic tool before any later analysis is carried out using Matlab.

After discussing V_Inc_Cont.vi, I will describe Page 1 and Page 2 in reverse order as I believe it makes more explanatory sense.

4.5.1 V_Inc_Cont.vi

This is a simple program that is used to set and vary the electron impact energy, while displaying the present energy. Its inclusion will serve to highlight and describe some features used in the main program.

On the front panel, figure 59, we have two simple means of controlling the impact energy of the electrons, direct input via a text box, or a slider, either of which can be chosen by flicking the toggle switch into the right position. It features a highly visible display of the voltage that is being applied as well as an “Analog Out” indicator that shows the voltage the 6008 DAQ is applying to the V IN terminal of the programmable voltage power supply. There is also a STOP button that is used to halt the program once running.

The block diagram contains all the relevant elements for the program's operation, and they are held within a *while* loop (grey surround). With the *while* loop in place the voltage setting of the 6008 DAQ, responsible for the electron impact energy, is being updated continuously. The blue boxed "100" is the factor V IN is scaled up by in the KEPCO APH500; the user inputs the desired energy (eV), the toggle decides which indicator to take this value from, and the value chosen is divided by 100 before being sent to the *analog out* of the 6008 DAQ device.

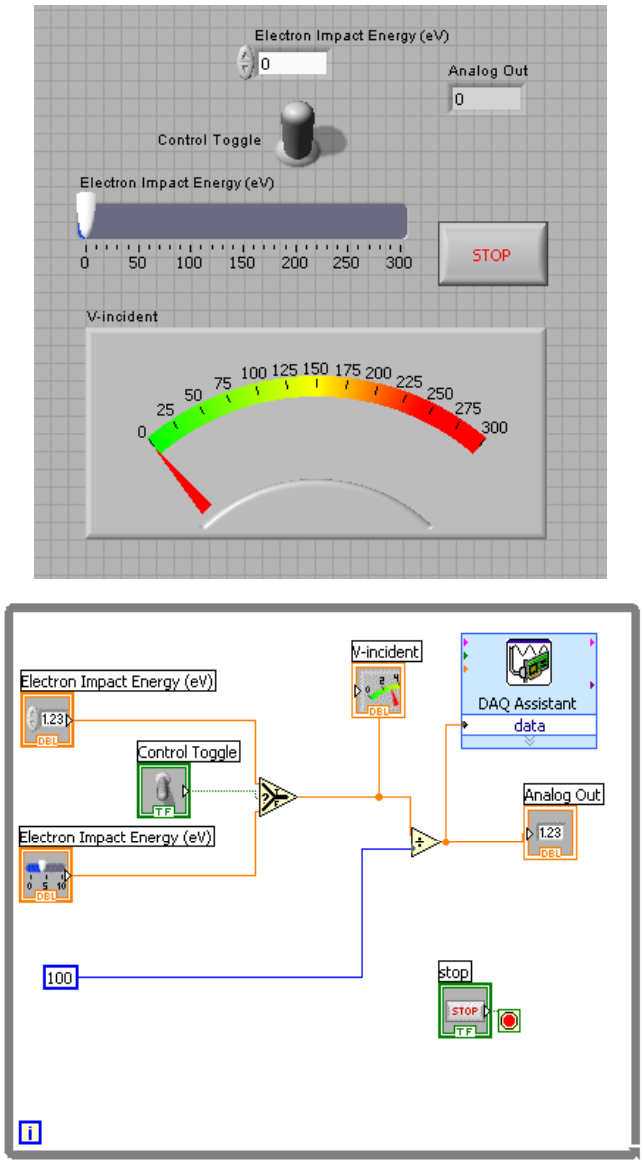

Figure 59: Top – Front panel of V_Inc_Cont. Bottom – Block diagram panel.

4.5.2 Scan_Acq.vi - Page 2

The *Page 2* program of Scan_Acq, figure 60, is used to open a previously acquired scan for observation, and for quick identification of the mass to charge ratio of peaks in a mass spectrum.

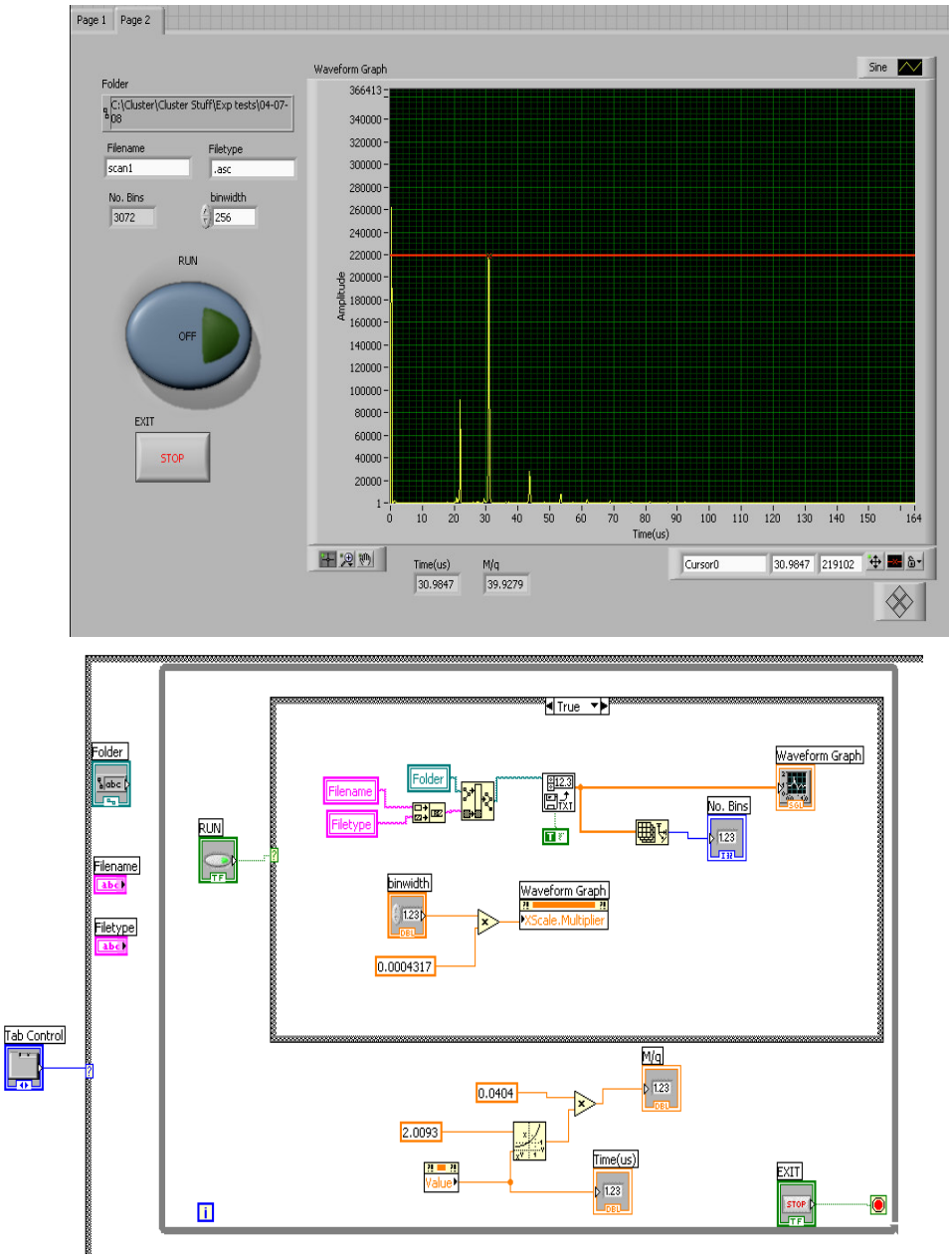

Figure 60: Front panel (top) and block diagram (bottom) for Page 2 of Scan_Acq. The entire loop of the diagram is not shown due to size constraints and the remainder being empty.

This program is simple in construction and is chosen for use by opening the main program and selecting the tab *Page 2*. This *Tab Control* in the block diagram chooses the *case* structure within which is bound the graphic language of the relevant page and program chosen.

The code in *Page 2* has two functions:

The first function is to open and read a scan from file, and display its mass or time-of-flight spectrum. This is performed by the piece of code shown in figure 61.

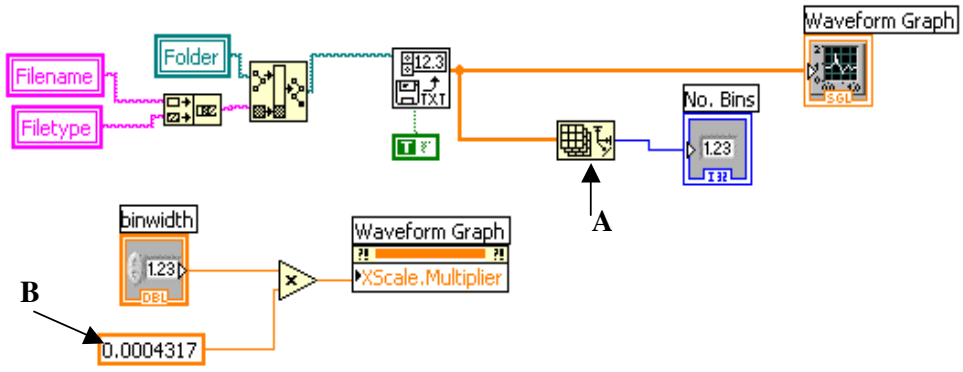

Figure 61: LabVIEW code used for opening files and for time axis scaling.

This occurs upon hitting the *run* button on the front panel. The upper code in the diagram is responsible for reading from a file and displaying the data. It also extracts, the number of channels recorded as part of the scan, via an array length measuring tool (A). The lower piece of code sets the time-of-flight axis scale for the waveform graph. The input box marked B indicates the time resolution (in microseconds) of one bin as calibrated in chapter 5. This is then multiplied by the binwidth of each channel of the MCS TOF spectrum taken, providing the relevant scale for the graph. This waveform graph has a massive array of settings, for zooming in and out, selecting regions, applying cursors and reading off values from these cursors, and it provides substantially more versatility than the previous software used.

The second function of the code in Page 2 is swift identification of peaks. By dragging a cursor over a peak in the mass spectrum we can read of the values of its TOF, its

magnitude and finally its ratio of mass to charge. The piece of code used is shown in figure 62.

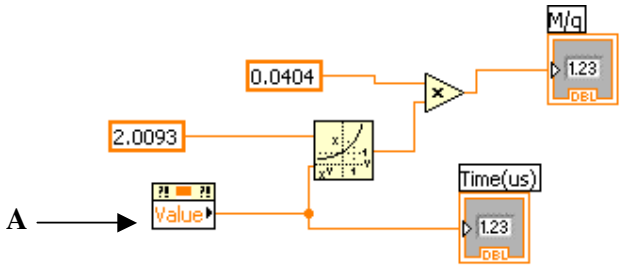

Figure 62: Mass to charge ratio calculation code.

It reads the time value (A) corresponding to the cursor position, and the mass to charge ratio is calculated using the relationship.

$$M/Q = 0.0404t(\mu s)^{2.0093}$$

This relationship is established in chapter 5, using Argon clusters as the calibration mechanism. The *while* loop that contains these pieces of code is needed so that one can move the cursor continuously while the mass to charge ratio is being updated regularly.

4.5.3 Scan_Acq.vi - Page 1

The LabVIEW program Scan_Acq - Page 1 is the main program used in the acquisition of scans. It can be used in single or multiple scan (multi-scan) mode. Single scan mode will not be explained separately, because it is covered in explanation of the multiple scan mode.

The multi-scan mode is designed for the acquisition of excitation functions. Scans are taken sequentially, with the specific electron impact energy incremented by some step value (*Step size*) each time, over some range of electron impact energies (from *Start Energy* to *End Energy*). Upon the increment in impact energy there is a time delay (*Delay*, typically 5 seconds) before the acquisition starts; this is to allow the electron gun to stabilise. By looping through the range of energies several times (*No. of Cycles*)

any time dependent effects can be taken into account. This is particularly important for the detection of metastables, where the scans need to be run over a long period. The scan data is acquired from the MCS and displayed in real-time, then saved to a specified location when each scan has finished running (*Filename*, *Folder* and *Filetype*). Several of the MCS settings are controlled via the interface: the range or number of channels (*Time*), the number of sweeps per scan (*Sweeps*), and the number of bins per channel (*Binwidth*). As well as this the interface visually outputs at what stage the program is currently at; the cycle number, sweep number, step number, etc, are all monitored. The user interface (front panel) is shown in figure 63, with all the inputs and outputs on display. The green and red lights next to the yellow *Run* button indicate whether the MCS is functional and ready to take a scan. The basic operation sequence of the program (multi-scan) is shown in figure 64.

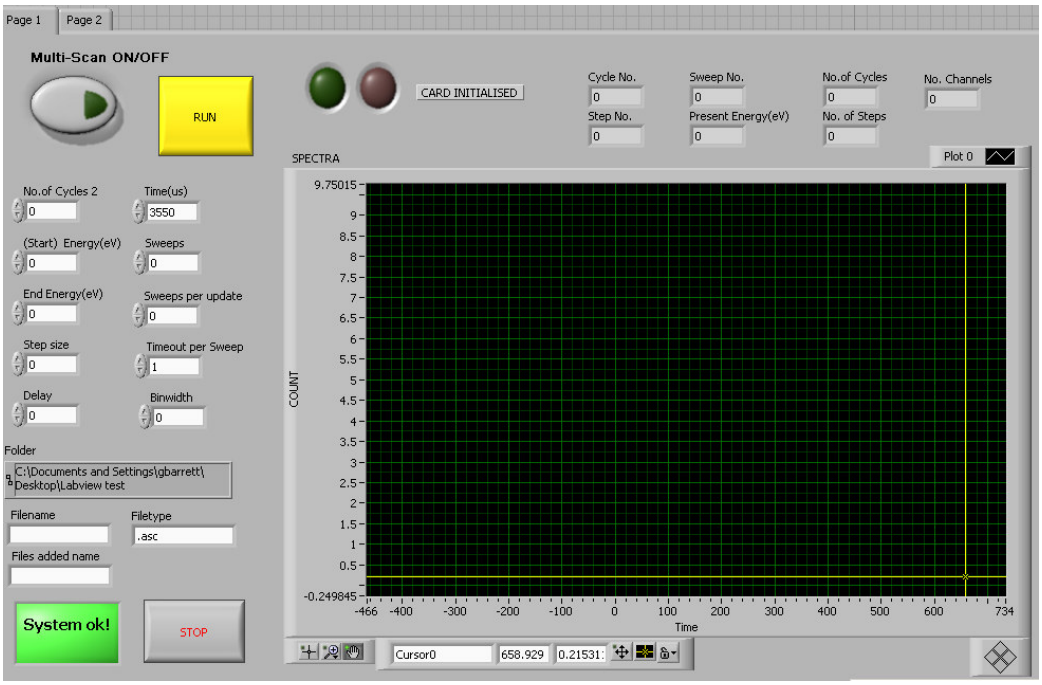

Figure 63: Front panel interface of the Scan_Acq – Page 1 program.

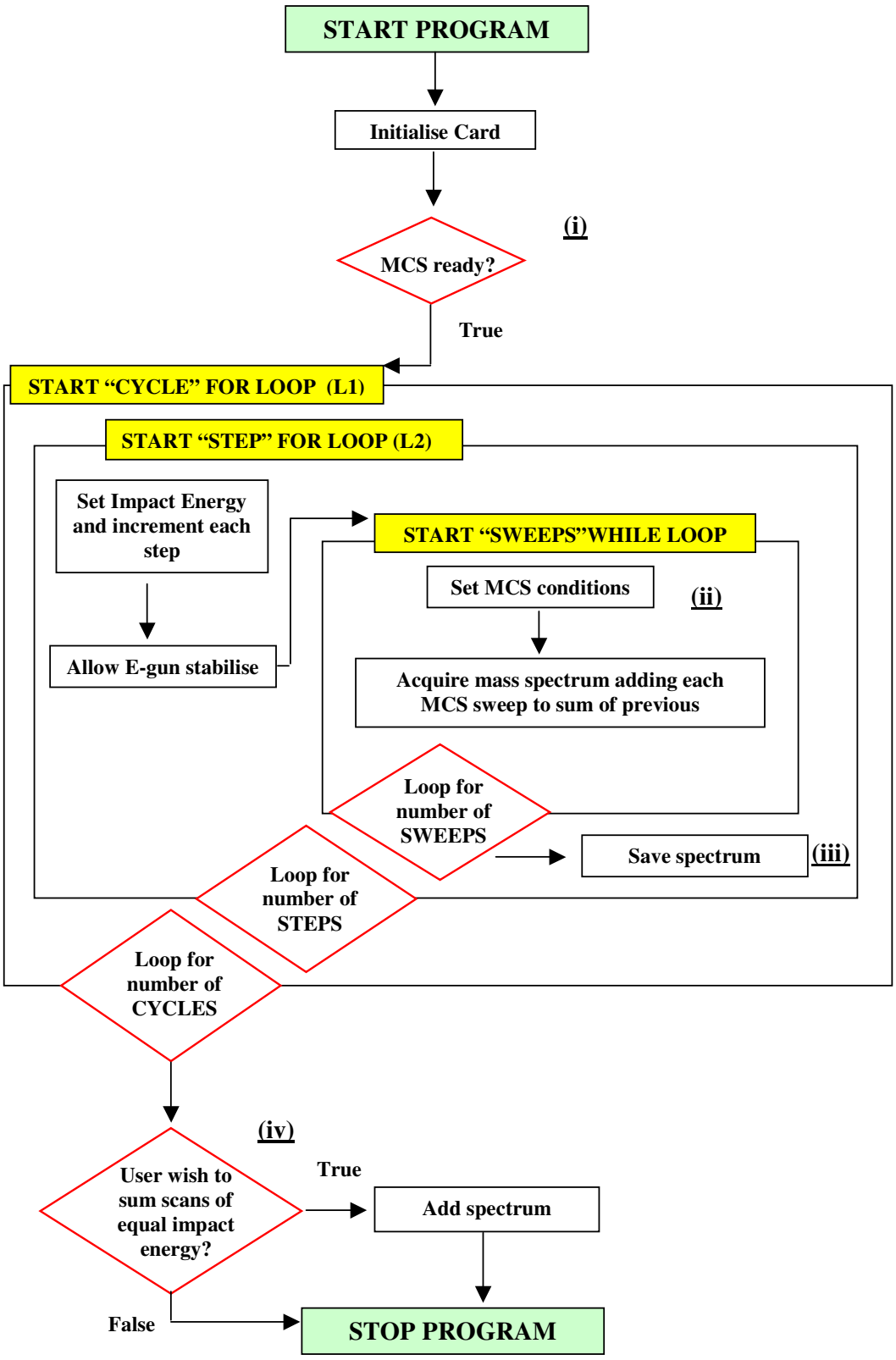

Figure 64: Flow diagram of the operation sequence of Scan_Acq - Page 1. Numerals represent areas that will be further explained in text.

The full block diagram is included in Appendix B and is slightly too cumbersome except to reproduce in miniature here, figure 65, only serving to highlight the region specific code corresponding to the actions in figure 64 are taken from.

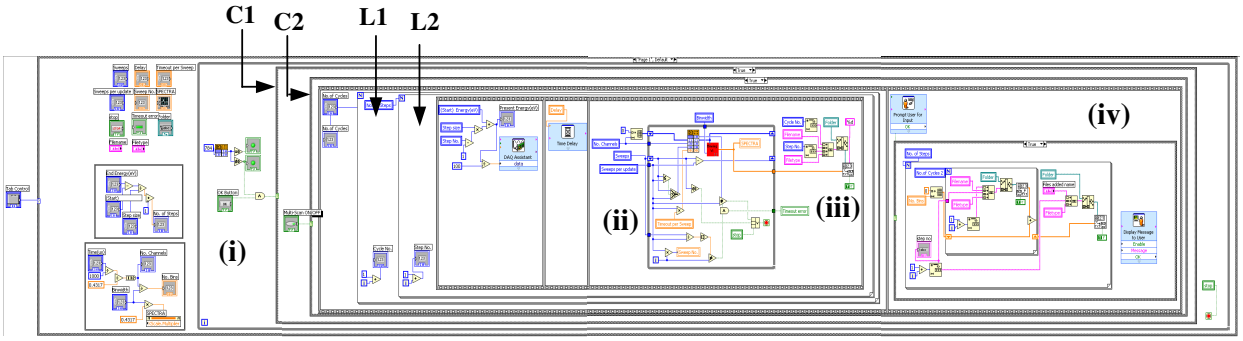

Figure 65: Miniature block diagram of Scan_Acq.vi. A large scale diagram is in Appendix B. Diagrams of sections (i) – (iv) are found in figures 70, 71, 72, and 74.

The program operates as follows:

(1) The program is set running. First the *call library node*, shown in figure 66, checks that the MCS is initiated and functional (region (i) with the code to the left of this region is used for simple calculations and defining of variables). If so, a *true* signal is sent to an indicator and to an *AND* function operator. Once the user observes that the card is initiated he can then set the program running by hitting *RUN* on the interface which also sends a *true* signal to the same *AND* gate. Upon receiving both these *true* signals the *AND* transmits a *true* signal itself, to a case structure (C1) that will only run the remainder of the program if *true* is received.

(2) We then proceed to a second case structure (C2), that chooses between single and multi-scan operation. This option is chosen on the user interface.

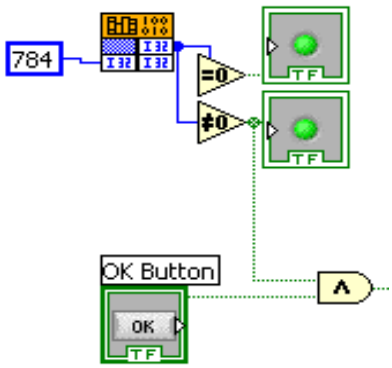

Figure 66: Card initiation region of section (i) figure 65.

(3) Multi-Scan being chosen we continue to a *for* loop (L1), that runs for the number of cycles entered in the interface. Within one cycle of this loop a complete set of scans across the range of electron impact energies, set on the interface, is taken. Multiple cycles are taken so that we have a number of such sets, each of which can independently be used to extract an excitation function, yet allow us to examine any time dependent effects in the spectra.

(4) Within the "*cycles" for* loop (L1) is a second *"steps" for* loop (L2), that runs the acquisition carried out by the MCS over a range of impact energies, stepping through those energies sequentially.

(5) Firstly, in this loop the electron impact energy is set as described for the V_Inc_Cont.vi program, and using code similar to that in figure 58.

(6) A time delay is put in place to allow the gun to stabilise before a scan is taken.

(7) After this delay the *"sweeps" while* loop (ii) used to acquire the TOF spectra is initiated (figure 66). It communicates with the MCS via the *Call library function node* as described earlier. The loop runs until the input number of sweeps has been carried out by the MCS. Data is binned within the loop by the SubVI

Binning.vi (shown in Appendix C). It concatenates the data from the MCS into a smaller array determined by the binwidth input by the user. This speeds up the waveform graphs display of the data and also reduces the observed effects of noise in the spectra.

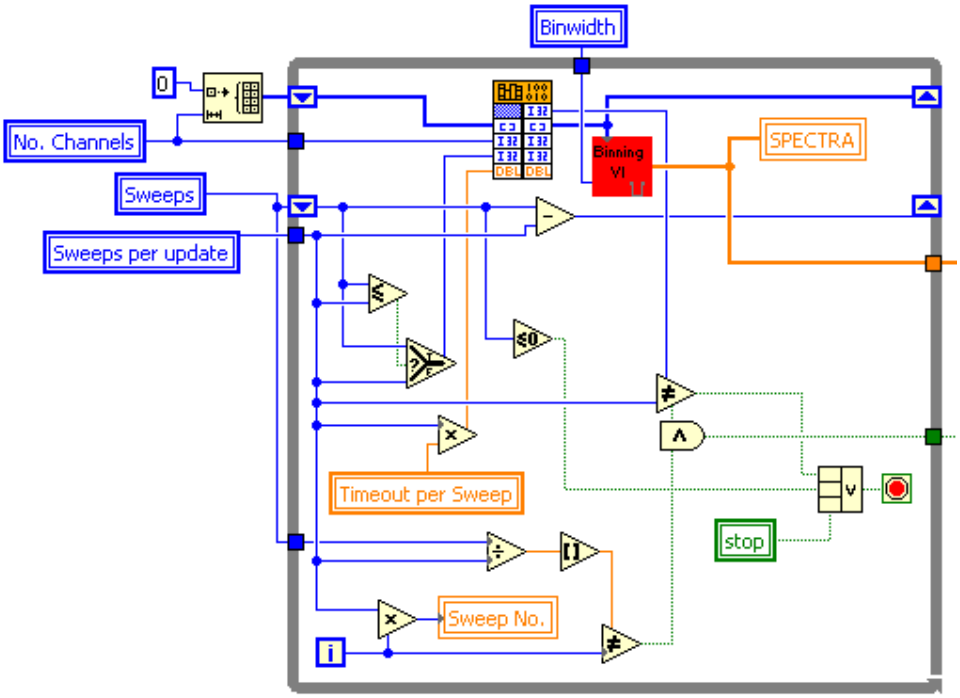

Figure 67: "Sweeps" while loop code for the acquisition of TOF spectra from the MCS. Section (ii) figure 65.

(8) Upon performing the relevant number of sweeps the data is sent from the while loop and saved (iii) in the address entered into the interface text panels (code shown in figure 67). For each step of the *"steps" for* loop the digit at the *end* of filename is incremented by one. For the different cycles a digit at the *start* of the filename is incremented, so for filename *scan* and number of cycles and steps both set to 3 the files are recorded in the following sequence in figure 68.

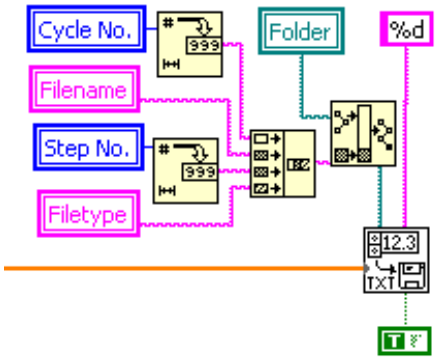

Figure 68: File saving code for Scan_Acq. Section (iii) figure 69.

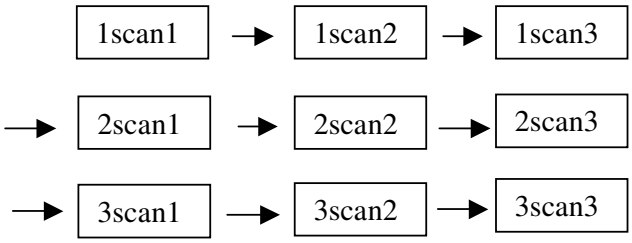

Figure 69: File saving sequence for cycle number and step number set to three with filename set to "scan".

(9) Finally, once all the steps and cycles have been performed the user will be given the request as to whether the scans of the same impact energy be summed together. Upon receiving a yes (or *true* signal) this task is performed by the code, figure 70, in region (iv).

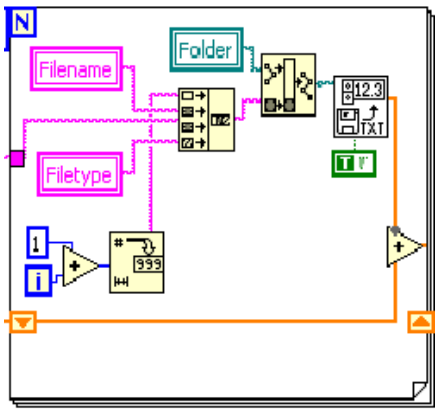

Figure 70: Scan summation code. Section (iv) figure 65.

(10) The program will only end properly once the *STOP* button is hit. Otherwise it sits, ready to take another scan or multi-scan.

4.6 Matlab Analysis

Matlab is a C based programming language and computing environment designed by *The MathWorks*. It is particular versatile when dealing with matrix operations, plotting and manipulation of data and of course algorithmic processes. The language itself is called M-code. It can be used simply by typing after the prompt in the Command window of the Matlab desktop. More often the code is written into a M-file that is then used as a function in that Command window. Matlab is also very capable in the plotting of data and has a sophisticated array of tools.

For the work conducted as part of this thesis it was necessary to write several pieces of code for analysis, manipulation and display of the data acquired by the MCS and LabVIEW software. Over time much of this code became incorporated into, or called upon by a bigger Matlab function or program. This program, "Cont16", is the final program developed for analysis of data and its functions are as follows:

(1) To display the raw data as a TOF spectrum.
(2) To concatenate the data into fewer channels and display this spectrum.
(3) Make it possible to sum over a number of peaks in the spectrum.
(4) To find the positions of all peaks above a certain threshold value.
(5) With the TOF corresponding to those peaks calculate the ratio m/q
(6) Display these peaks.

The code used is included in Appendix D. When the function is called upon by entering "cont16(scan)" in the command window, the following operations are carried out on the file named "scan":

(a) "Scan" is sent to the main program cont16.m first. Here, the data is first concatenated by a desired amount (2^n), and along with the raw data, displayed as a function of TOF. Then the user is requested as to which regions he would like to sum over. Integration is performed over those relevant regions and the results are output to the user. Then the program calls upon the program find_peaks.m to which it sends the concatenated data, now named "squash".

(b) In find_peaks.m an algorithm is carried out upon the data in "squash" that calculates the positions of the various peaks. Before it can do this however it first requests a threshold from the user, above which to search. The peak positions are calculated by looking at the zero points of the gradient of the data. The program then re-plots the data with markers on the peaks to aid the user in assessing whether they are genuine peaks or just noise (figure 71). At the end of this code is a call to either of two programs that can be used to calculate the mass to charge ratio of each of the peaks appearing in the mass spectrum.

(c) The two programs are titled comptime.m and massperq.m. The former calculates the mass to charge ratio using quite a large algorithm. It is based on a theoretical calculation involving the apparatus dimensions and the voltages applied in the reflectron. The later, a more accurate program, is based on a semi-empirical equation obtained by suitable fitting to an argon cluster mass spectrum. Typically it was massperq.m that was chosen for use in this work. However, the theoretical approach is of potential use. It contains factors to account for the initial velocity and position of the ions, and as such could reveal some useful information about the source cluster pulse and the initial ion spatial and velocity distribution upon extraction. This has not been fully explored.

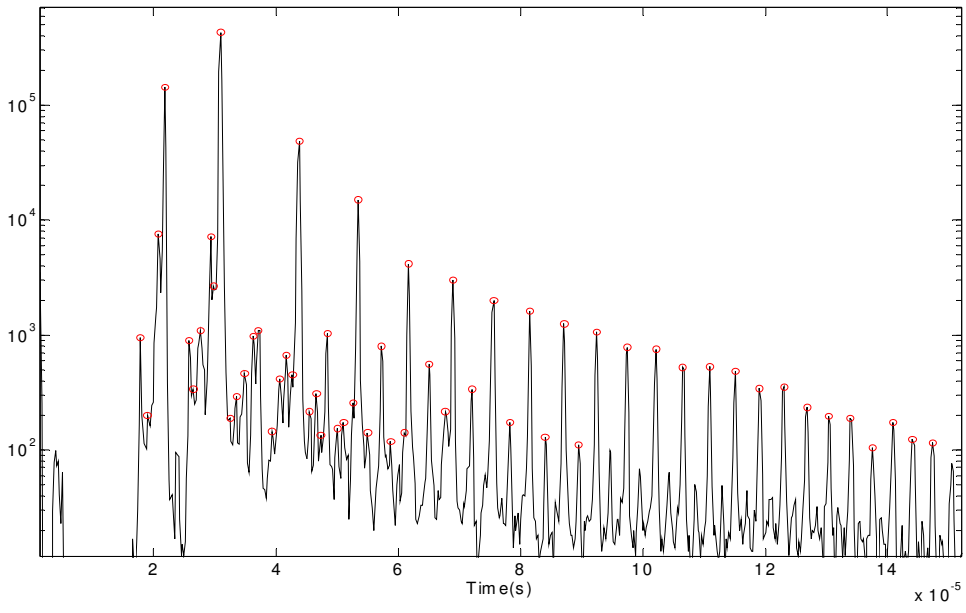

Figure 71: Portion of argon cluster spectrum, displayed using Matlab, with peak finding points indicated by red circles. Applied for a threshold of 100 counts.

This program has been used in most of the analysis and plotting on display in the experimental work of chapter 5.

CHAPTER 5

Experimental Results

5.1 Overview

This chapter will look at the experimental work carried out as part of this thesis. The experiments can broadly be split into three different classes, calibrations, optimisations, and measurements of time-of-flight spectra (ions and Metastables). Certain tests were carried out only to serve as indicators or as a diagnostic for another test. Substantial cluster production only became more regular with the use of the LPV valve and nozzle of .2mm from Agar Scientific. Before this many earlier tests were subject to low cluster yield.

Tests of the MCS, calibration and operation, will be looked at in section 5.2 and section 5.3. Optimisation tests of the deflection voltage of the reflectron were carried out, section 5.4, as well as tests of the detection rate of the MCP as a function of voltage, section 5.5. Tests of the electron gun stability range and the deflection system will be described in section 5.6 and 5.7. Calibration of the TOF mass spectrometer, necessary for mass to charge ratio determination is described in section 5.8. Section 5.9 deals with the experiments carried out on the earlier Series 9 solenoid valve and its replacement LPV bi-morph valve. The final four sections deal with experimental tests involving cluster production and metastable detection, section 5.10 showing cluster production dependence on pressure, section 5.11 looks at the mass spectra and excitation functions produced for argon with methanol clusters spectra and excitation functions displayed in section 5.13. Argon metastable time-of-flight spectra have been recorded and are presented in section 5.12.

5.2 Calibration of Multichannel Scaler

The multichannel scaler 7886S card was calibrated in order to determine the time length of one channel when there is only one bin per channel. The method used employed the Stanford digital delay generator (DDG) as the source of a START and STOP pulse sent to the MCS. On account of this the accuracy of the MCS calibration is limited by the accuracy of the digital delay generator (for a delay of 10000 ns the time error between two outputs is typically 100ns). The delay between the two pulses was varied over a range and the channel the STOP pulse was recorded at could be observed in the mass spectrum. During the course of the thesis the PC in which the card was installed (Windows 2000 with 196Mb of RAM) was replaced with a newer one (Windows XP and 1Gb of RAM). This should not have a substantial effect on the MCS channel width. For the old PC the precision of a channel was found to be 431.194 ± .028 ps/channel. After changing the PC the MCS was recalibrated, with the graph shown in figure 72, and while not substantially different, the new precision was determined to be 431.676 ± .003 ps/channel.

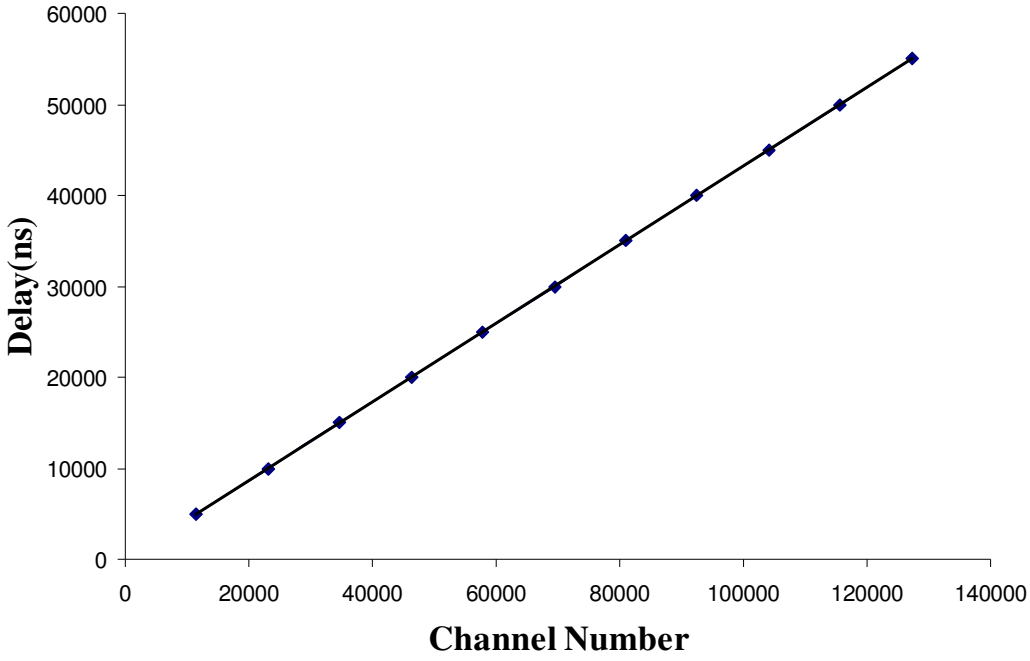

Figure 72: Calibration graph of 7886 multichannel scaler.

5.3 Multichannel Scaler Coincidence Test

Tests were taken to ensure that the MCS was counting all the pulses that were exiting the Ortec 9327 unit coming from the MCP. This was undertaken by simultaneous running of the 7886 and a Hewlett Packard 54520 digital oscilloscope (sampling rate of 2G Sa/s), both triggered by the same pulse from the Stanford DGG, over same time interval and number of scans (16 - limit of Oscilloscope memory), and both recording pulses detected by the MCP detector from ions created in a background gas of argon created by a DC (non-pulsed) electron beam. The setup is shown in figure 73.

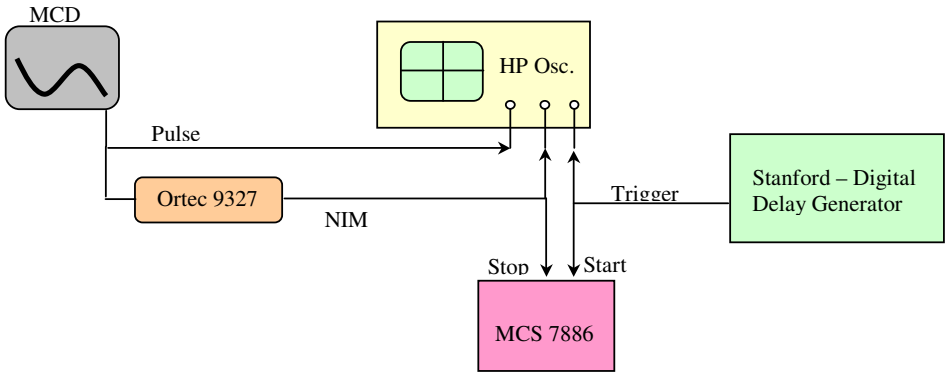

Figure 73: Coincidence test of 7886 multichannel scaler setup.

The tests showed that over the random spread of noise the detection positions were identical for both the 7886 and the HP 54520, figure 74, indicating the MCS is counting properly.

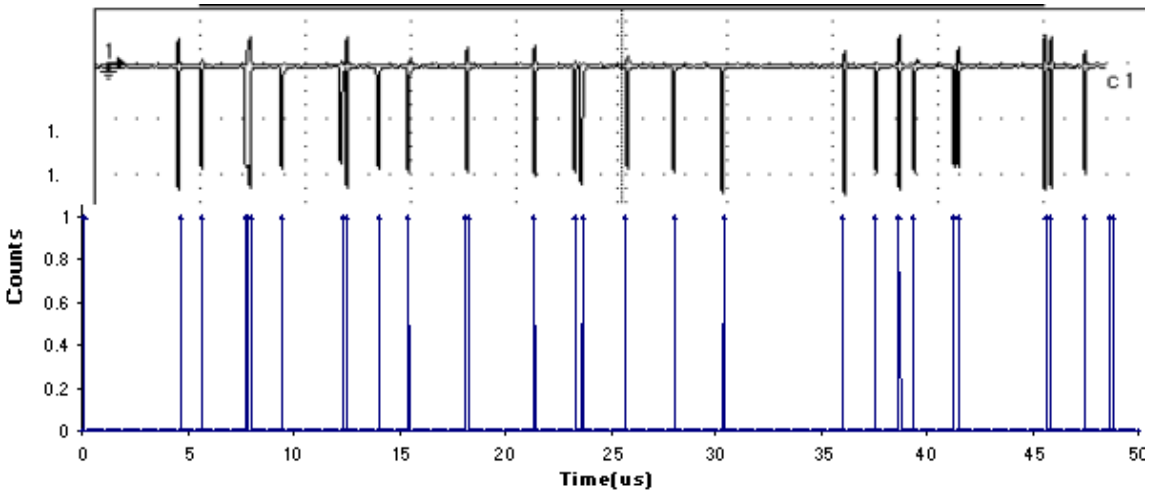

Figure 74: Typical coincidence test of 7886. Bottom MCS, top HP 54520.

5.4 Deflection Voltage Optimisation

In order to be detected at the MCP, ions entering the time-of-flight chamber are deflected downward by V_{def}, a voltage across a set of plates at the entrance to this region. A test has been done to find the optimum setting for this by measuring the argon ion yield as a function of this voltage. The result is shown in figure 75.

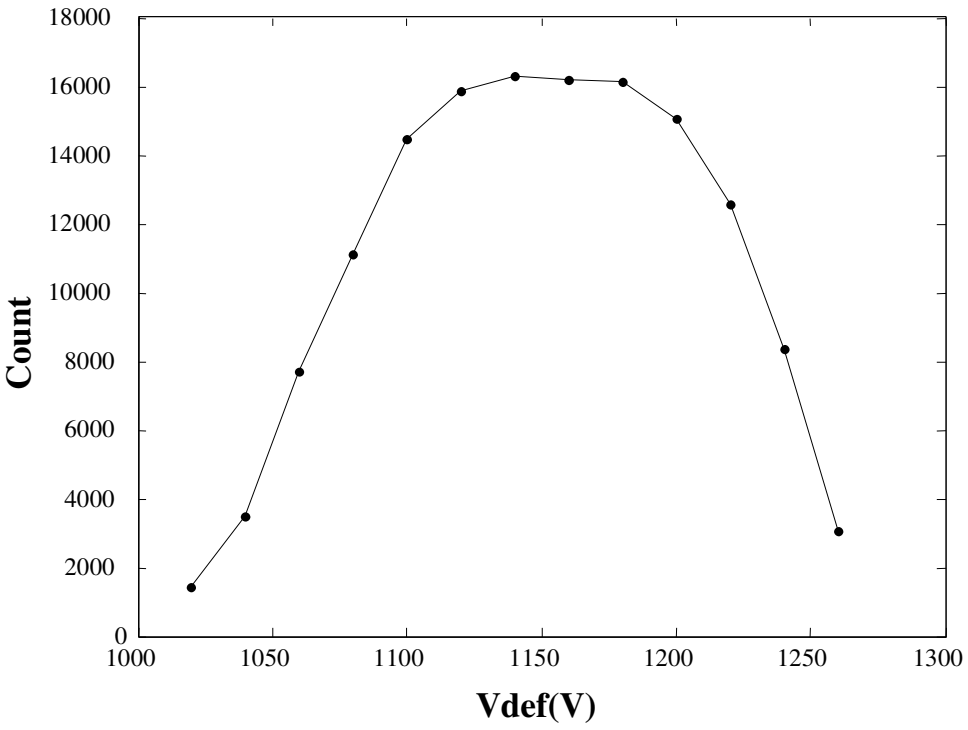

Figure 75: Optimisation of the deflection voltage. Voltages are negative.

This plot indicates an optimal operational voltage range of (-1130 to -1170V). This agrees with our typical operational value of –1140V, previously determined by J. Lynch.[1]

5.5 Microchannel Plate detection rate test

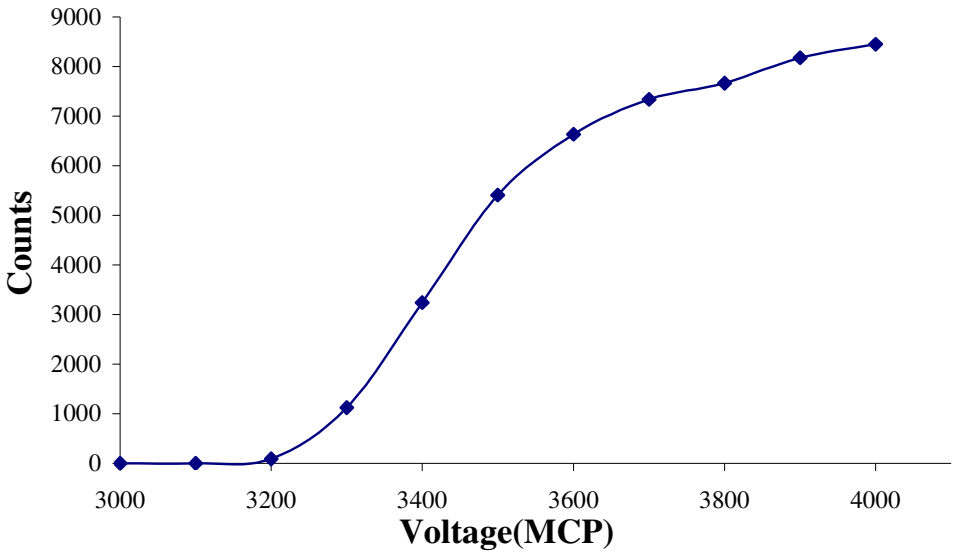

Figure 76: Argon$^+$ detection rate as function of MCP voltage. The MCP voltage is negative and corresponds to the voltage distributed across the MCP plates, as described in chapter 3.

The above graph, figure 76, is a test that shows the operational voltage for detection of argon ions from the TOF mass spectrometer. The rate increases rapidly from –3200 to –3500 before it begins to steady off. The detection dependency on voltage was only conducted for singly ionised argon but for future reference it would be worth conducting the same test on clusters as a function of size and to observe any variations. Typically the MCP is operated at -3700V, although higher voltages might be better for detection they could also shorten the lifespan of the MCP (see section 3.5.1).

5.6 Electron Gun Tests

The stability and alignment of the electron gun are crucial in taking excitation functions or the observation of low energy electron impact. Observing the Faraday cup currents as a function of electron incident energy tests these factors.

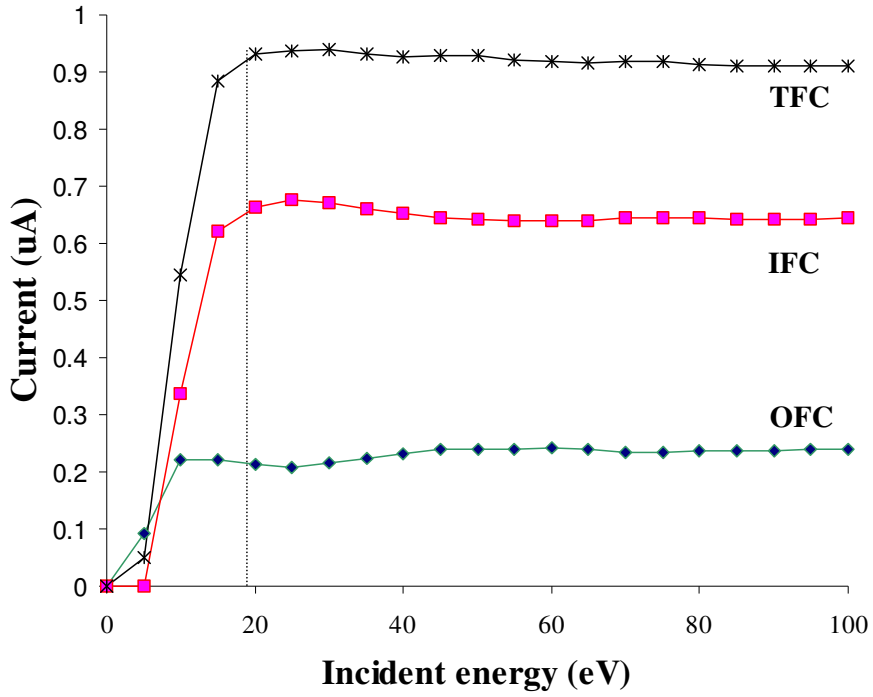

Figure 77: The total(TFC), inner(IFC), and outer(OFC) Faraday cup currents for a non-pulsed electron gun as a function of incident energy. The dashed line indicates the limit of stability.

Setting	V (Non-pulsed – Figure 87)	V (Pulsed – Figure 88)
$V_{filament}$	2.5	2.59
$I_{filament}$	2.232A	2.225
V_{GRID}	4.34	-0.78
V_1	61.9	104
V_2	263	260
V_3	49.8	41
$V_{X1/X2}$	0/0	-6.82/+6.82
$V_{Y1/Y1}$	0/0	-.009/+.023
V_6	12.8	31

Table 4: Electron gun settings for DC (Non-pulsed) and pulsed operation.

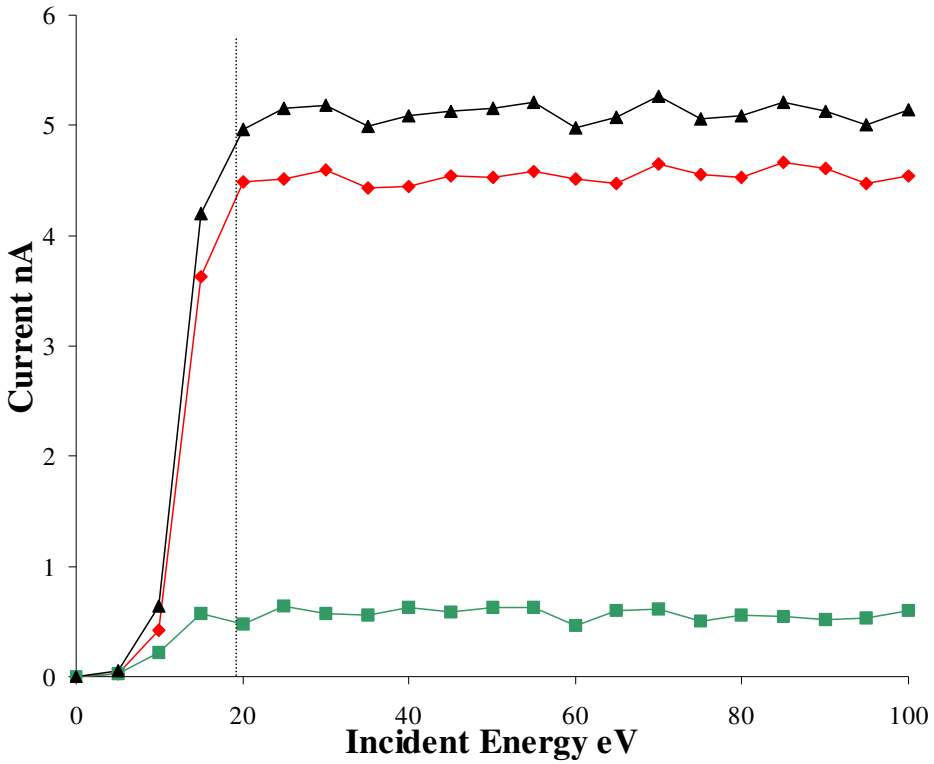

Figure 78: The total(TFC), inner(IFC), and outer(OFC) Faraday cup currents for a pulsed electron gun (10 kHz, 1 µs width) as a function of incident energy. The dashed line indicates the limit of stability.

Tests were carried out over a range of electron gun settings in order to determine the most suitable conditions for operation. The results shown in figure 81 and 82 indicate the range of operation over which the e-gun is stable, in pulsed and DC (non-pulsed) mode. It shows good stability down as far 20eV below which the current begins to collapse. It also shows a decent ratio of inner to outer Faraday cup currents, indicating that the beam is quite well localised. This ratio can be improved upon by suitable voltage settings, however with less constancy on variation of the impact energy. The alterations that were put in place, as described in section 3.8, to eliminate an observable deflection of the beam by the Liner voltage are adequate as little or no deflection is now observable. Suitable settings of the e-gun are included in table 4.

Clearly, the lower range of the e-gun is not adequate for electron impact energies below 15 eV and plans are underway to amend this by appropriate use of magnetic fields.

5.7 Deflection System Test

A test has been conducted to observe the effects of the deflection system in the Y direction as described in chapter 3. The latest of these tests was carried out by measuring the count rate of Ar^+ for the range of voltages possible on Y1. The indications are, from figure 79, that the deflection system is operational however is not adequate enough to steer the electron beam across the full width of the cluster beam.

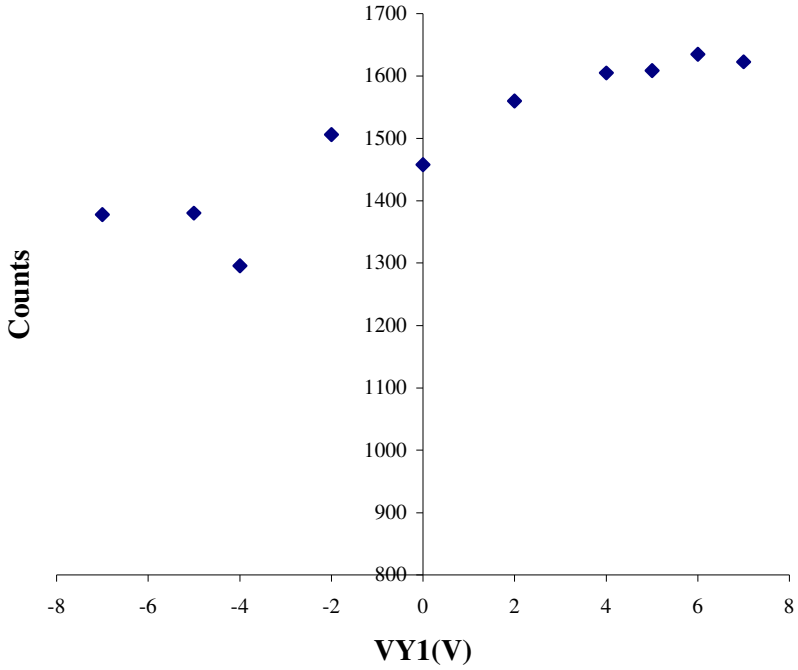

Figure 79: Variation in the detection rate of Ar^+ ions as a function of the Y deflection, perpendicular to the direction of the cluster beam.

The test indicates that the DC voltage sources currently used are not high enough. Plans are underway to replace them with AC to DC converters, that provide a higher DC voltage output.

5.8 TOF Mass Spectrometer Calibration

Generally in time-of-flight mass spectrometry the mass to charge ratio for a particular peak, at time *t* is given by an equation of the form,

$$\sqrt{\frac{M}{q}} = kt + c$$

where *k* and *c* are constants acquired as part of the calibration process.

Previously, prior to cluster production this was calibrated by using obvious peaks such as Ar^{+}, Ar^{++}, H_2O^{+}, CO_2^{+} and basically any remnants from the atmosphere gas that could be used. However this always left a limited number of data points to base that calibration on. Below, in figure 80, I have calibrated the TOF to M/Q ratio by using an Argon cluster mass spectrum. This allows an excellent number of data points. I have used the time positions of up to Ar_{32} and instead of using the linear equation above have chosen whichever method of fitting that produces the best R^2 fit. In the end this required a power series trendline that produces a value of unity for R^2. The equation is very nearly equal to the equation above and is given by,

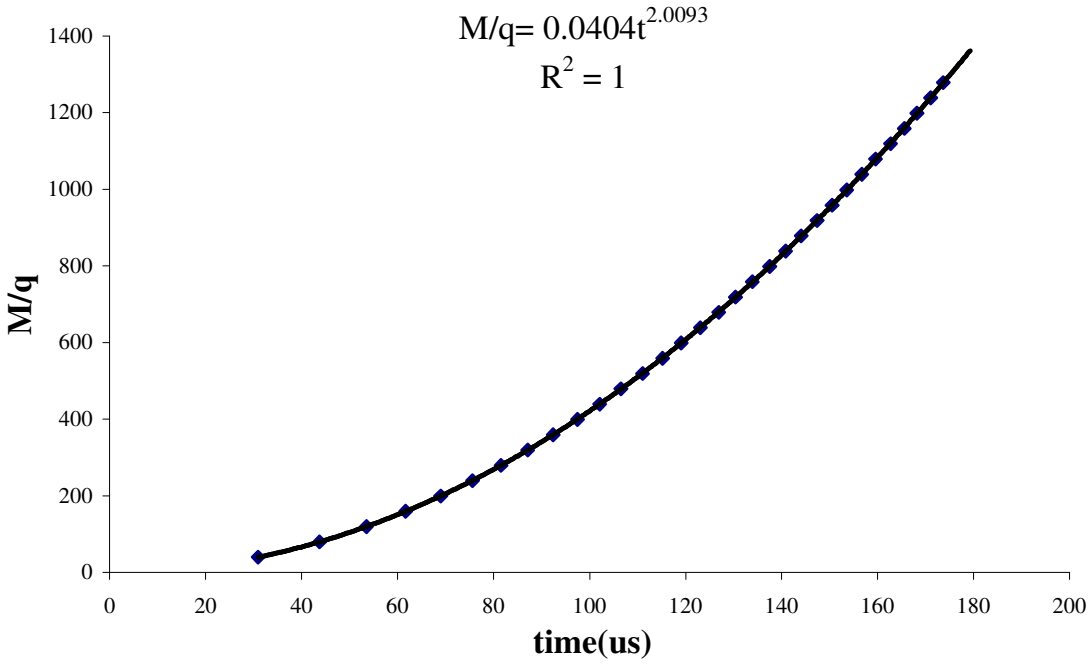

Figure 80: Calibration of the TOF using the Argon cluster series up to n=32.

The reason a power series provides a slightly better fit is as yet unclear, and as such the equation above is semi-empirical in nature. However, because of its greater accuracy this semi-empirical equation has been chosen for use in the LabVIEW program Scan_Acq, described in chapter 4, and the mass calculations referred to later in this chapter.

5.9 Pulsed valve tests

Two different pulsed valve types have been used in the course of this thesis, described in chapter 3. First there was a Series 9 solenoid valve in the system with a 0.5mm divergent nozzle (figure 39, right). A study of the gas profile from this nozzle for various skimmer-nozzle distances was performed and indicated that the valve was not functioning adequately, as shown in figure 81. The valve should be opening cleanly for 500μs, whereas the profiles indicate an initial opening peak followed by a much broader hump that lasts far too long. Profiles were obtained by pulsing the valve with argon at 2.5bar, and taking mass spectrum, as a function of the delay between the valve pulse and the electron gun pulse, $A = T_0 + X$, where T_0 is the valve pulse, and X is the variable delay. By plotting the Ar^+ yield against the delay X a profile is generated.

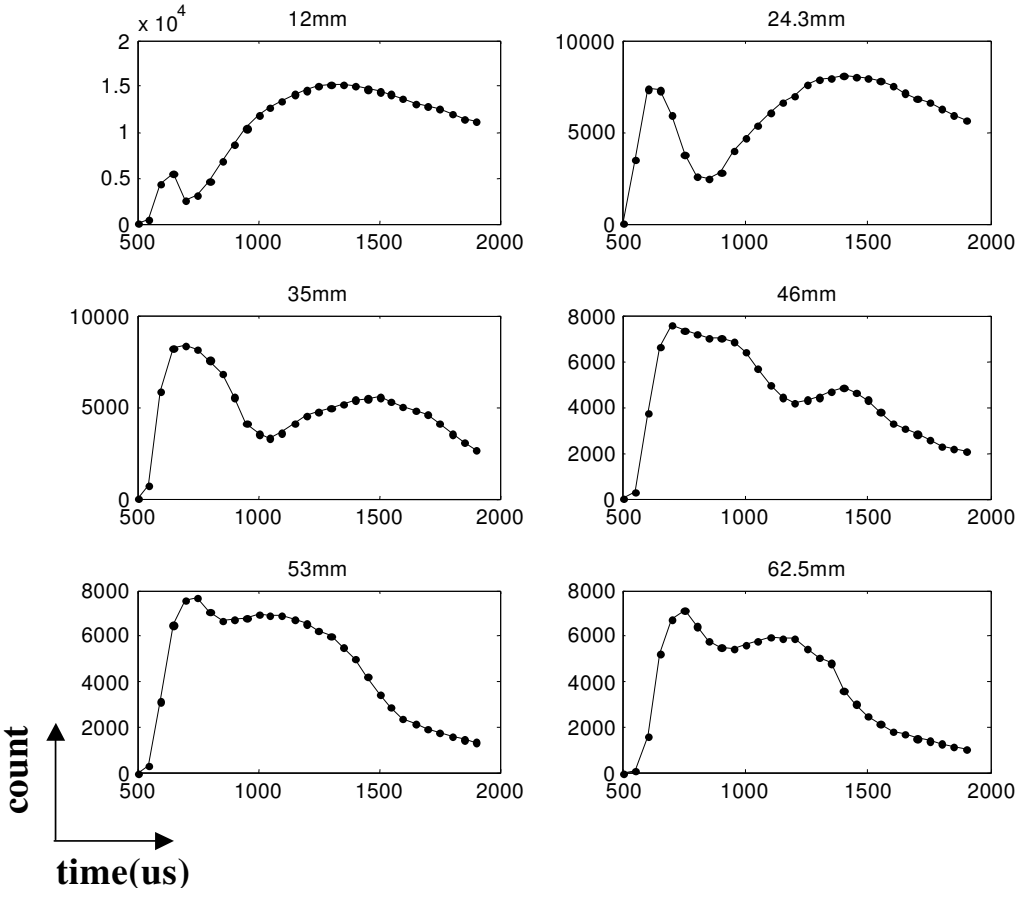

Figure 81: Series 9 pulse profile evolution with skimmer-nozzle separation, for 2.5 bar of argon and a 0.5mm divergent nozzle.

The Series 9 solenoid valve failed to produce all but a trace of methanol clusters.

This valve was replaced by a similar model, except this time with a 0.3mm nozzle with 45^{o} exit cone. Tests of this arrangement did indeed produce improved profiles, figure 82, yet not ideal. The valve operated down to a lower limit of 250µs whereupon the signal would falter.

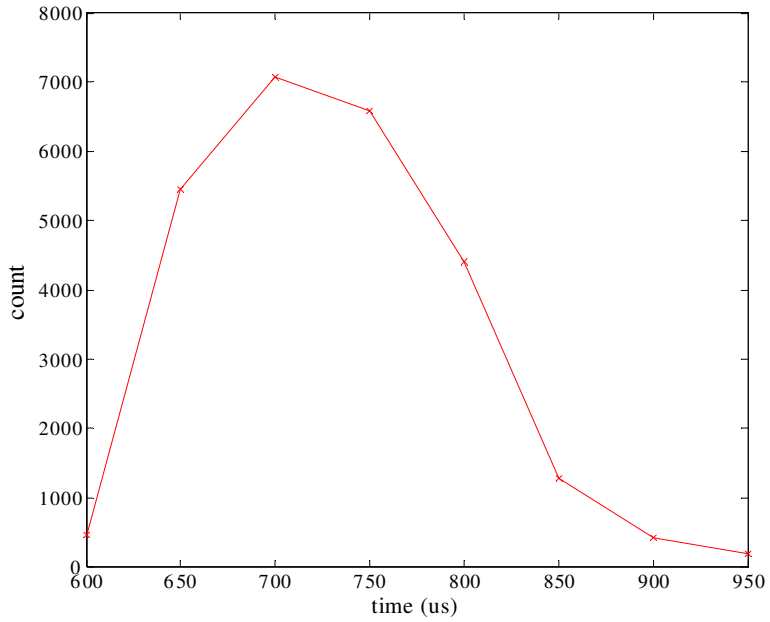

Figure 82: Pulse profile for a Series 9 solenoid valve, of 300µs width, 2.5bar argon, and with a 0.3mm divergent nozzle.

Initial tests on argon alone and methanol alone failed to produce any clustering. However, by returning to test argon, after a methanol test, clustering of methanol was observed, yet in very low quantities. This was a simple case of argon acting as a carrier gas, as described in chapter 2, on methanol that had condensed on the metal surfaces of the inlet line and valve, which had not been adequately pumped out. A best example is shown in figure 83. In this case argon was used as the carrier gas at 1.5 bar. Nitrogen is the dominant cutoff peak. The clusters observed correspond to protonated methanol clusters and are evident up to n= 13. No argon clustering was observed. Further experiment failed to produce any consistent levels of methanol clustering.

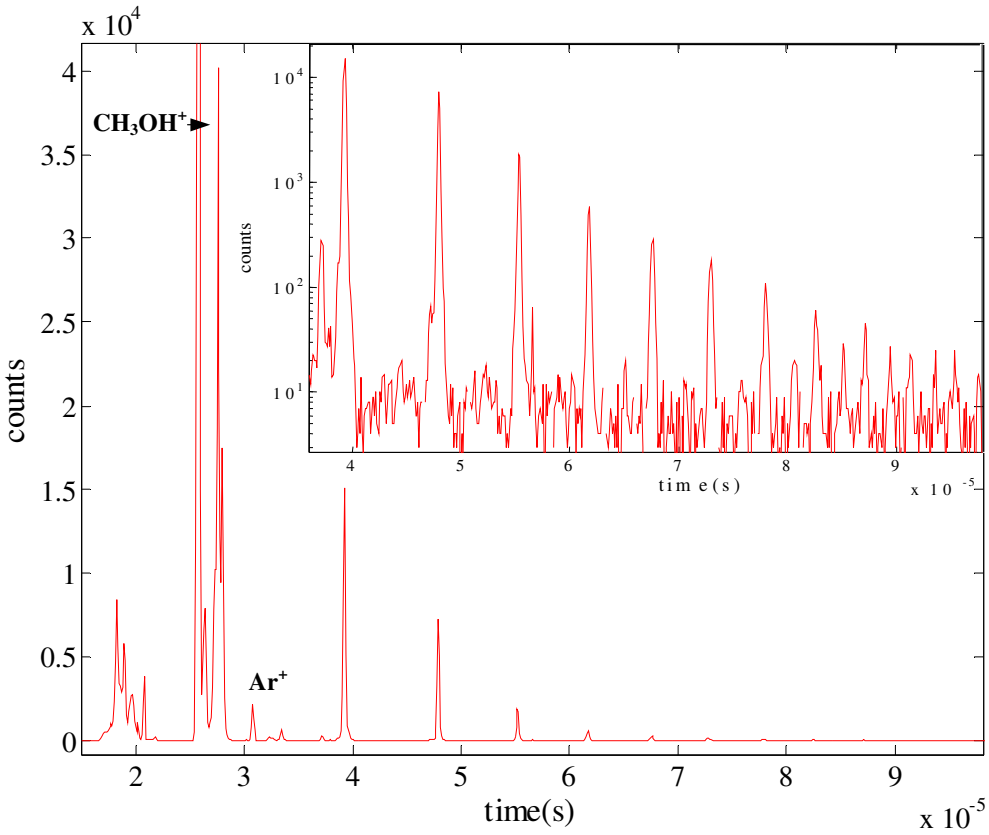

Figure 83: Best example of methanol cluster formation for the Series 9 valve, 0.3mm divergent nozzle, with argon (1.5bar) as the carrier gas. Inset – log scale enlargement of cluster region up to n=13.

A Lasertechnics LPV valve replaced the Series 9 solenoid valve. This valve has already been described in chapter 3 (figure 40). This valve has produced clusters of both argon and methanol in good yield without the need for a carrier gas in the case of methanol. It is used with a divergent nozzle of 0.2mm Agar Scientific nozzle (figure 41). A standard pulse profile of this valve is shown in figure 84. Based on this, the delay between the valve pulse and the electron beam pulse was set at 500 - 520µs. The spectra acquired will be looked at in section 5.11. The valve operates well down to 150µs. It must be noted that the tightness of the nozzle holder in the valve itself is critical to good operation. This tightness is responsible for the seal created by the valve piston against the nozzle. If it is too tight little gas is let out; this is on account of the range the bimorph can flex within the valve not being adequate to open the valve properly. Too loose and leaks will appear upon pulsing the valve in vacuum. This adjustment has proved challenging and because the conditions outside are not vacuum, it largely comes

down to a case of trial and error, with a great deal of patience required in order to find a good setting. Whenever such an adjustment is made the profile must be taken again as it has a large impact on the shape of the gas burst from the valve.

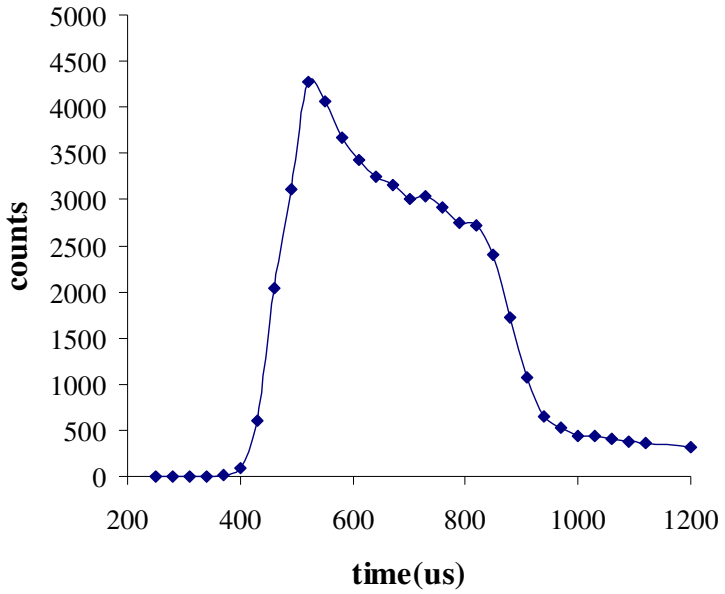

Figure 84: Pulse profile for a LPV valve, 500µs width, 2.5bar argon.

Tests have been carried out on the valve over the range of pressures from 1 to 3.5 bar argon without substantial variation in the profiles observed. Again, these profiles are generated by looking at the yield of Ar^+ for various delays of the electron beam with respect to the pulse valve. These tests indicate that the typical 2.5 bar pressure used is a suitable operating pressure. A test of cluster formation as a function of pressure is included in section 5.10.

The method of acquiring a pulse profile is quite time consuming because the delay has to be changed for each scan until the electron beam has covered the range of the pulse. Using the metastable detector an alternative method has been applied, one that requires only a single TOF scan to be taken. Essentially what occurs is the electron pulse width is set large enough to cover at minimum the time taken for the gas to reach the interaction region (400µs), and to cover the length of the pulse itself (max 550µs). The electron gun is set so that no delay exists between its pulsing and the valve opening. When the electrons interact with the gas beam photons are emitted and are detected by

the metastable detector. By allowing a spectrum to build up what we are seeing is the profile of the cluster beam or gas pulse itself. Small amounts of metastables are also detected but with a yield that is much smaller than the photon yield. A profile constructed in this way can take as little as one twentieth the time taken using the mass spectrometer method and it has total resolution in the sense that there are no gaps between delays in the profile. A set of tests for various valve pulse widths is shown in figure 85. Here the valve is operated at 20 Hz and the electron beam width is 2 ms. The voltage on the channeltron detector is +3.2 kV. Notice that the beam intensity maximum is constant for all widths and the secondary peaks that indicate bouncing of the valve. This is not a major concern, as it should not affect clustering from the valve. It might be possible to eliminate the bouncing by tightening the grip on the bimorph in the valve, but this is a very subtle and difficult correction to make.

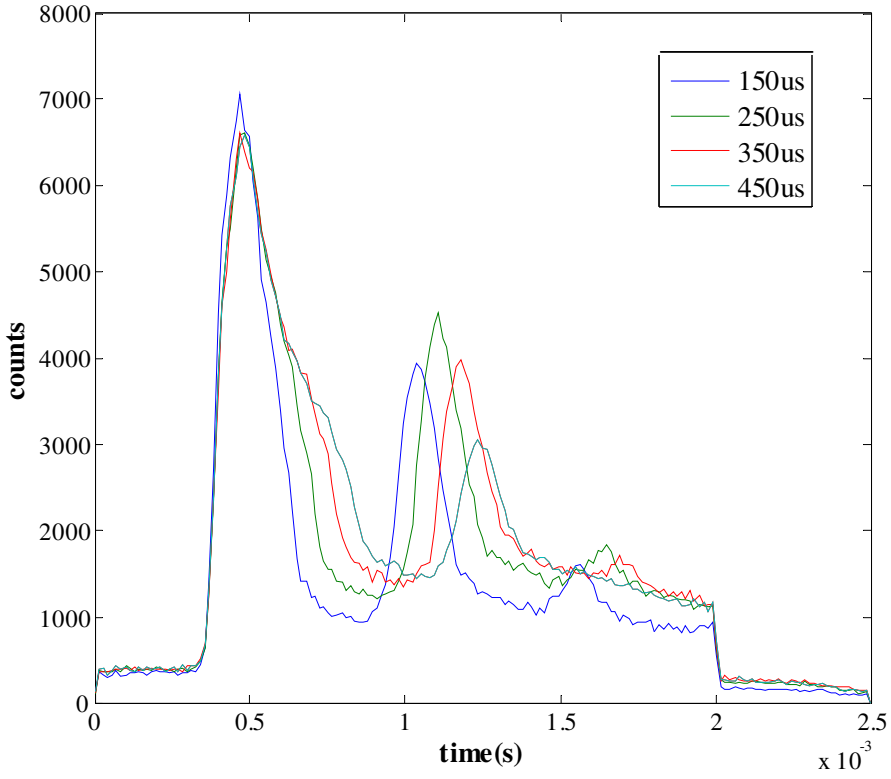

Figure 85: Pulse profiles of LPV valve as a function of valve pulse width. Obtained using photon detection by the metastable detector with a 2ms electron gun pulse.

5.10 Clustering vs. Pressure

To discern the optimum pressure for argon cluster formation a couple of short studies were performed for a small range of pressures. The test in figure 86 shows the dimer and trimer ratios to the argon atomic ion, produced as a function of the stagnation pressure. While the statistics are relatively poor the indications from this test, performed at a delay of 600μs, indicate a sharp decrease in production below 2bar, along with a slow increase above it. They do not indicate any substantial gain in running above 2.5bar.

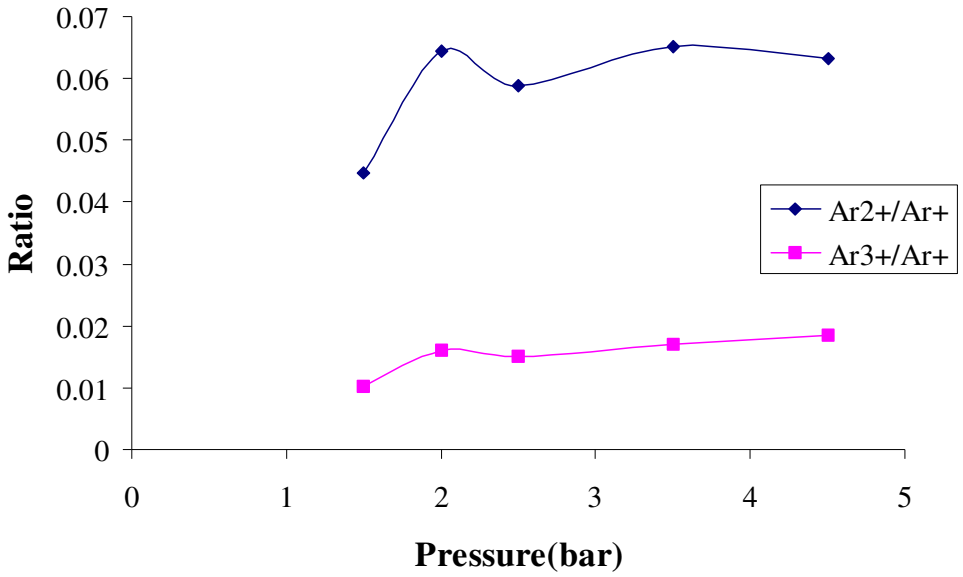

Figure 86: Cluster production ratios for argon dimer and trimer, as a function of stagnation pressure.

This test is supported by a subsequent test, shown in figure 87, that displays the dimer-monomer ratio as a function of delay for a range of pressures. Though the pressure range is not as high as above the study indicates the distribution of cluster density within the pulse, as well as an obvious increase in production with pressure. The ratio has a maximum of just under 7%, whereas later tests have produced up to 11%. This test was run for a valve pulse of 580μs, the experimental maximum limit of the valve pulse box.

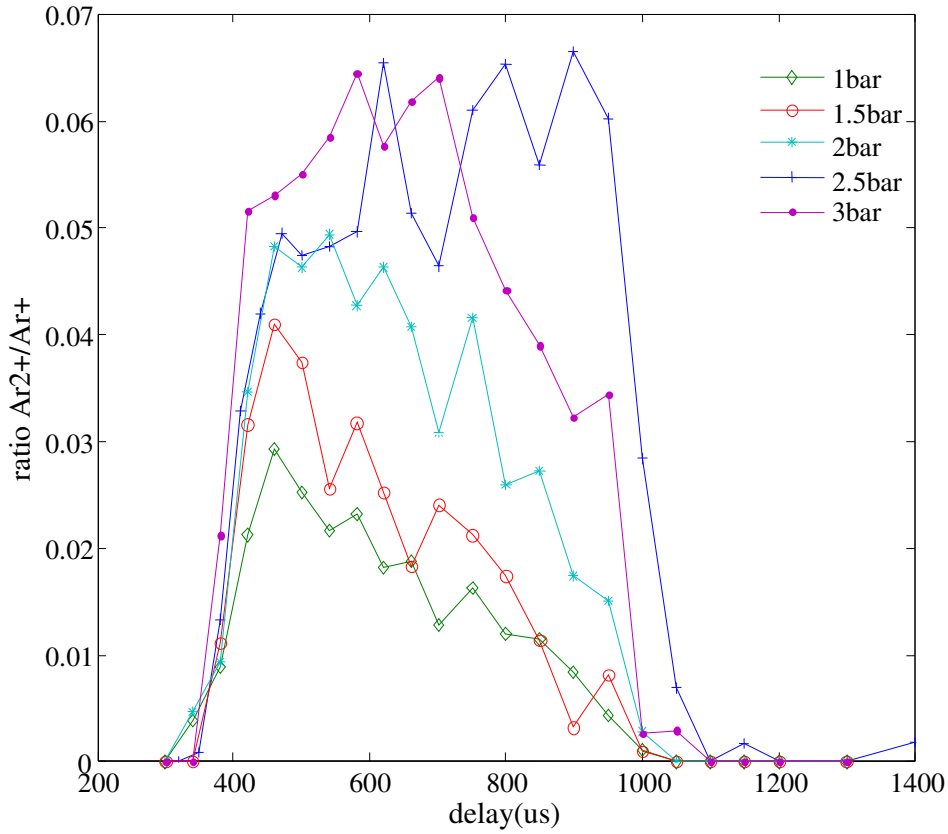

Figure 87: Argon dimer/monomer ratio as a function of the delay between the electron beam and valve pulse. The valve pulse width used was 580µs, and was pulsed at 6Hz.

Tests like the one above could prove useful for future work in the study of metastables where, in order to distinguish between the contribution to the TOF spectrum from atoms or clusters, it is useful to understand the cluster ratios involved. Also TOF spectra from metastable detection can take quite long so the system must be optimised as much as possible to improve the statistics of the contribution due to clusters detected.

5.11 Argon Mass Spectra and Excitation Functions

5.11.1 Mass Spectra

First I present a mass spectrum for argon, taken at 2bar stagnation pressure, for an electron incident energy of 100eV, and a rep. rate of 4Hz. I include two plots, figure 88 and 89, the logarithmic plot making it far easier to see the level of cluster formation.

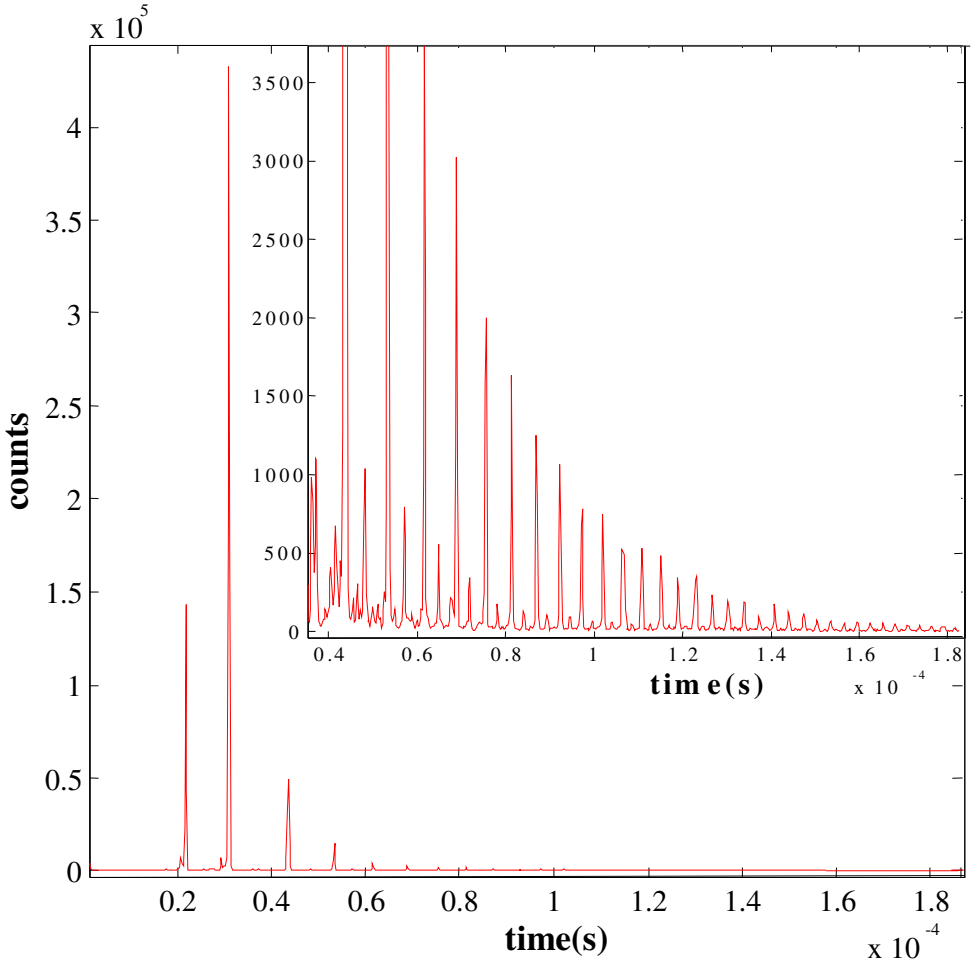

Figure 88: Argon cluster spectra for 2bar pressure and 100eV incident energy. Inset is an enlargement of the area after the Ar^+ peak.

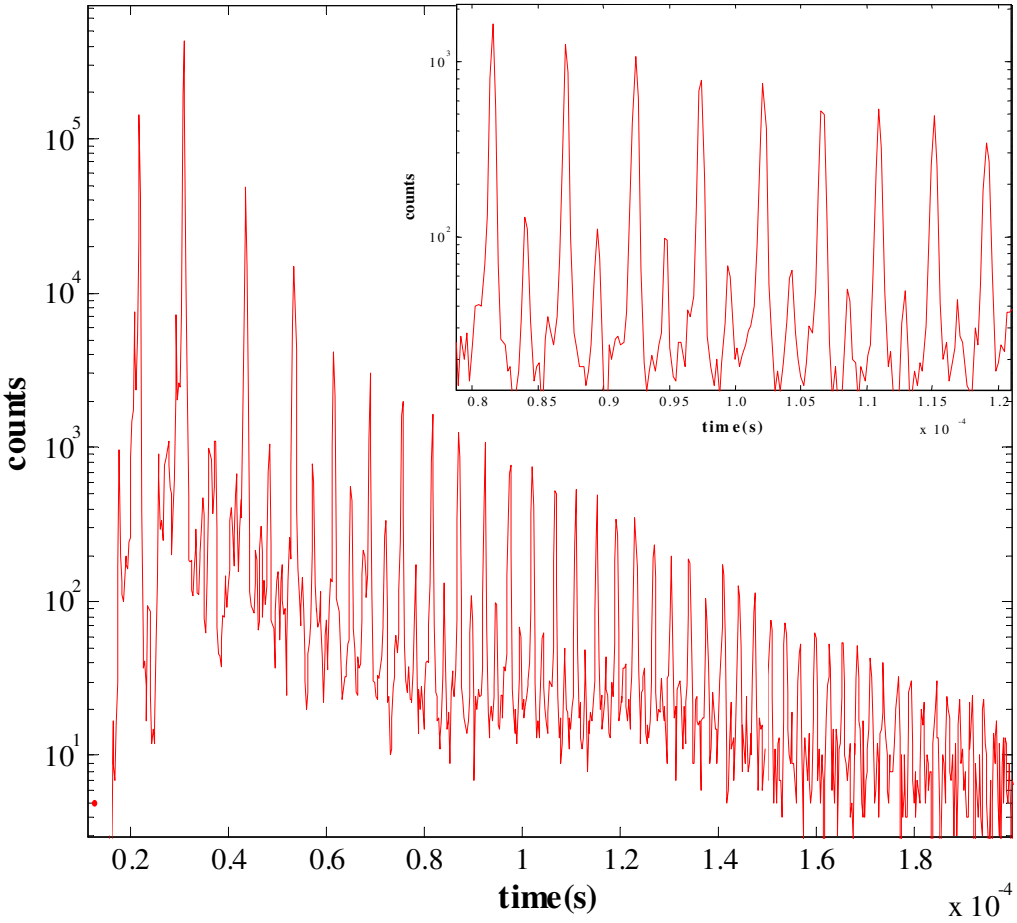

Figure 89: Logarithmic plot of argon cluster mass spectrum. Inset is a magnified portion to highlight the existence of a second series identified as $(H_2O)Ar_n^+$.

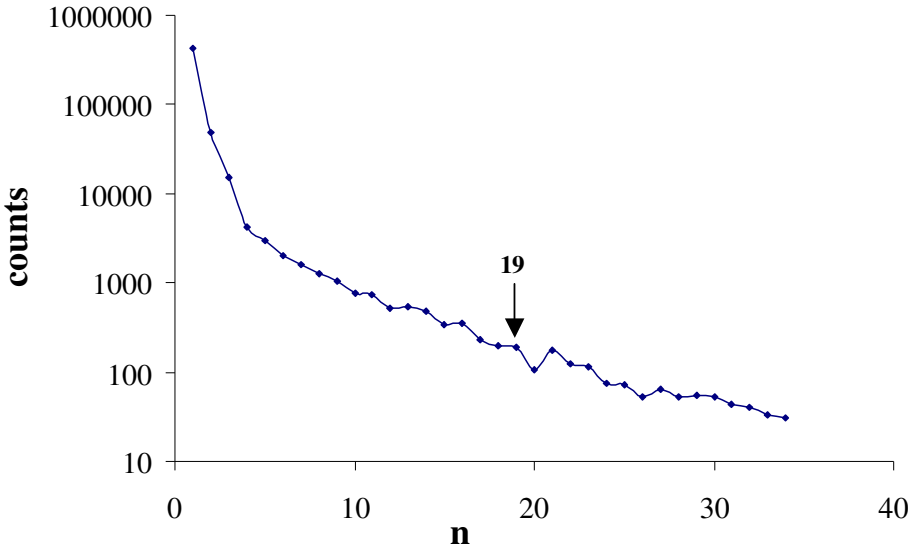

Figure 90: Cluster yield as a function of size, n, for Ar_n^+.

As can be observed there is the primary argon clustering series (A) that runs up to n = 40 before noise becomes too dominant to distinguish a peak. In the mass spectrum a drop in intensity can be spotted at n = 20, highlighted in figure 90. This corresponds to a stable structure cluster of "magic number" n = 19, in agreement with previous work.[2]

There is also a secondary series of smaller magnitude (B) that can be distinguished and is enlarged in the inset of figure 89. This series is attributed to $(H_2O)Ar_n^+$ confirmed from figure 91, a plot of the mass to charge ratio of the these peaks as a function of *n.* The slope of the graph is the mass of argon and found to be **39.98 ± 0.05u** and the intercept is the mass of an attached water molecule and determined as **17.36 ± 0.65u**, in agreement with the assumption. This indicates water contamination of the system, which could be avoided by "baking" of the gas inlet line valve to evaporate any residual water before argon is introduced.

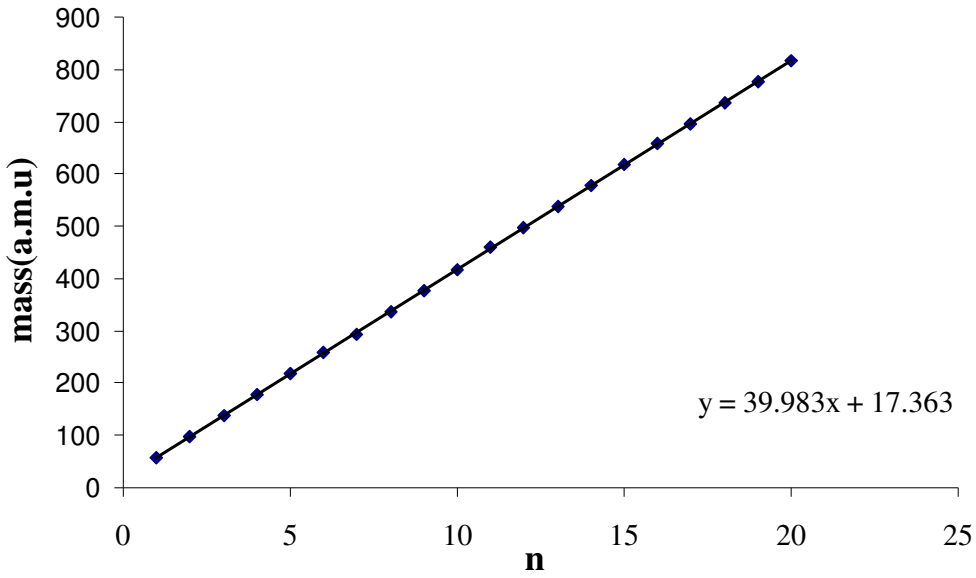

Figure 91: Atomic mass versus n for the minor series (B) in the argon spectrum.

5.11.2 Excitation Functions

Excitation functions have been taken for Argon and Methanol, singly and doubly ionised, as well as for several sizes of singly ionised clusters. These were carried out as part of testing of the program "*Scan_acq",* and though only preliminary do indeed demonstrate it is functional. The scans were not run over a long period and as such the statistics are only sufficiently good to provide excitation functions for the smallest clusters. Because it known that the electron gun intensity decreases rapidly below 20eV the appearance potentials below this value must be treated tentatively.

The argon excitation functions were taken by sweeping the electron energy from 10 to 120 eV in steps of 5 eV using the *"Scan_acq"* program. Each scan was run at 5 HZ over only 1000 sweeps, and the stagnation pressure was 2bar. The excitation functions produced are shown in figures 92, 93, and 94.

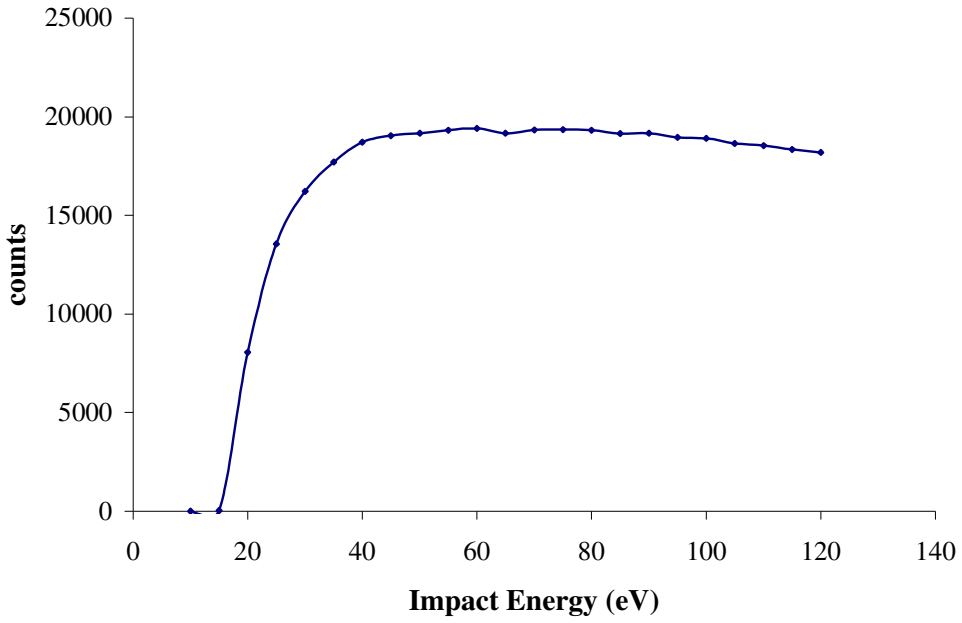

Figure 92: Excitation function of Ar^+, taken by electron impact on argon at 2 bar stagnation pressure.

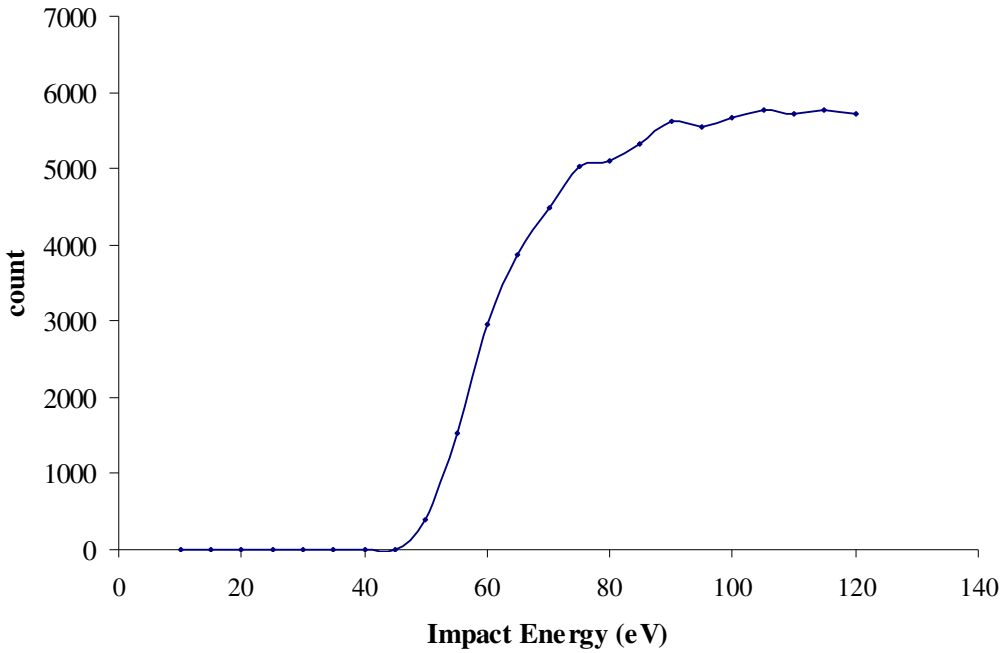

Figure 93: Excitation function of Ar^{++}, taken by electron impact on argon at 2 bar stagnation pressure.

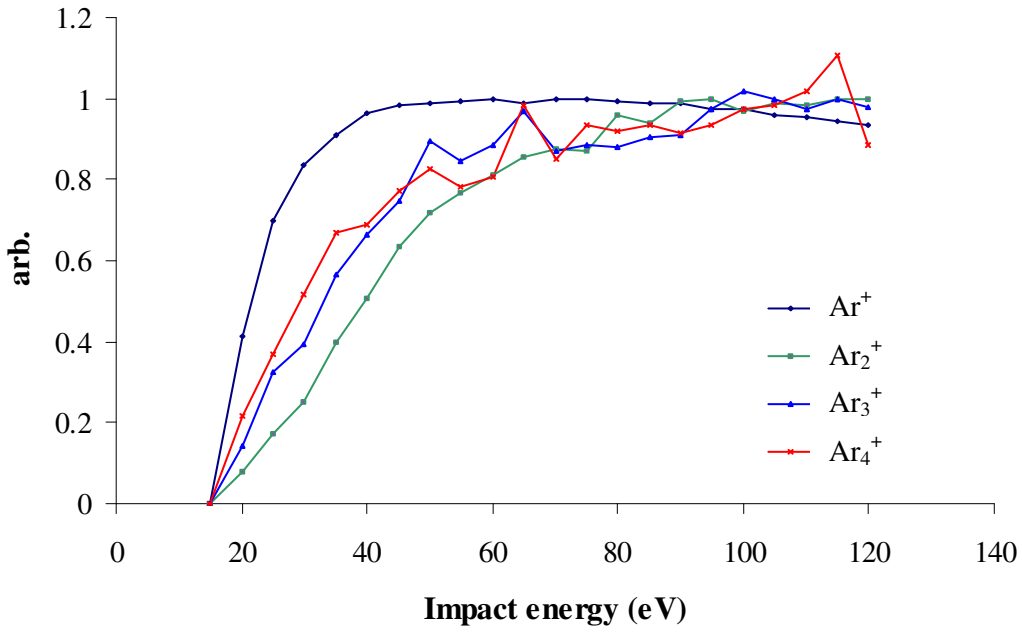

Figure 94: Excitation function of Ar^+, Ar_2^+,Ar_3^+ and Ar_4^+, taken by electron impact on argon at 2 bar stagnation pressure. Plots have been normalised.

Figure 94 contains several excitation functions that all converge to the point at 15eV. They are all zero at this point except for Ar^+, which has a very low level. This could be indicating that the appearance potential for Ar^+ is near this point and if repeated with more data points this could be determined more accurately. This would agree with the accepted value for the appearance potential of 15.73eV.[3] The zero level at this point for the clusters is an experimental factor, longer scans for more energies would allow more precise determination.

For onset for doubly ionised argon occurs in a region where the electron gun is stable. The appearance potential is evident just below 45eV. The accepted value is 43.4eV.[4]

Apart from telling us when the onset of a particular species occurs, the appearance potentials can be used to calibrate the electron impact energy by comparison with known values. From these preliminary tests the indications are that the electron gun is as operating close to its indicated value (45 eV versus 43.4 eV). Future tests over longer scans and a greater number of energies will improve upon this.

5.12 Argon Metastable TOF Spectra

The metastable detector and its method of operation have been described earlier in chapters 3 and 4. Initial tests on the output signal from the detector were observed using the HP 54520 oscilloscope and indicated that the pulse shapes out were fine; these tests were conducted by pulsing air into the system and crossing it with a DC electron beam. The house of the detector is held at a negative potential of –200V, to repel electrons from entering the channeltron. By decreasing this voltage stray electrons, simultaneous with the electron pulse, were observed, a further indication that the detector was functional.

In this section I present two TOF flight spectra taken for argon metastables produced via electron impact at 50 eV (figure 95) and 30 eV (figure 96). These values were chosen for easy comparison with work by van der Burgt *et al*[5], which used a similar setup and flight path length (124mm versus 195 in Maynooth), shown in figure 101 (the time-of-flight axis of our results was scaled suitably for direct comparison).

Because the initial attempts to take TOF spectra indicated a low count rate the electron pulse width was increased to 10 μs and the discriminator level set to only 9 mV. The delay value was set at 500 μs with the MCS triggered on the A pulse (1 μs before e-gun pulses) to allow observation of the initial photons produced in the interactions. The repetition rate was increased to 30 Hz and the argon was held at a stagnation pressure of 3bar.

The scan times are different for the two spectra, the 50 eV scan taken over 2 hours, and the 30 eV taken over 8 hours. These scans show good correlation in shape to those of van der Burgt *et al*. With more fine tuning of the system and longer scan times better scans will be produced.

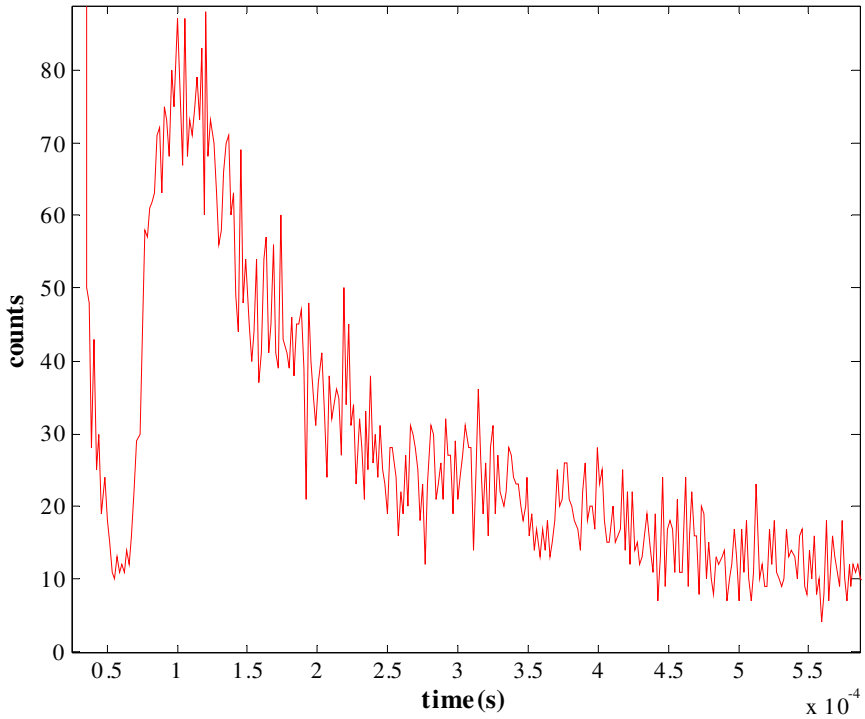

Figure 95: Neutral metastable TOF spectrum for argon, via electron impact at 50eV.

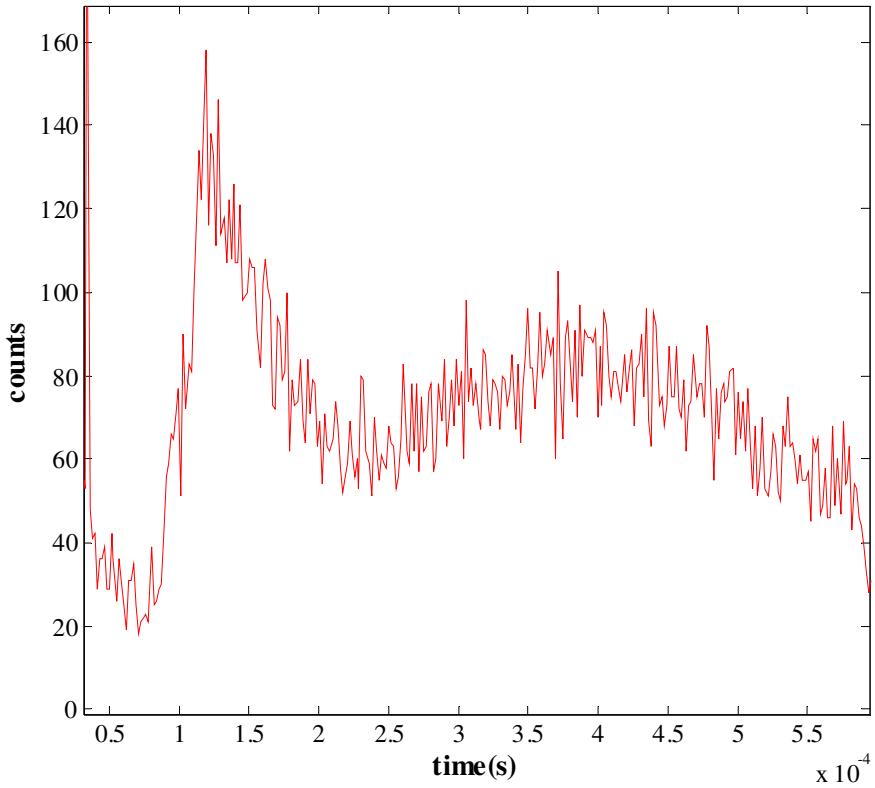

Figure 96: Neutral metastable TOF spectrum for argon, via electron impact at 30eV.

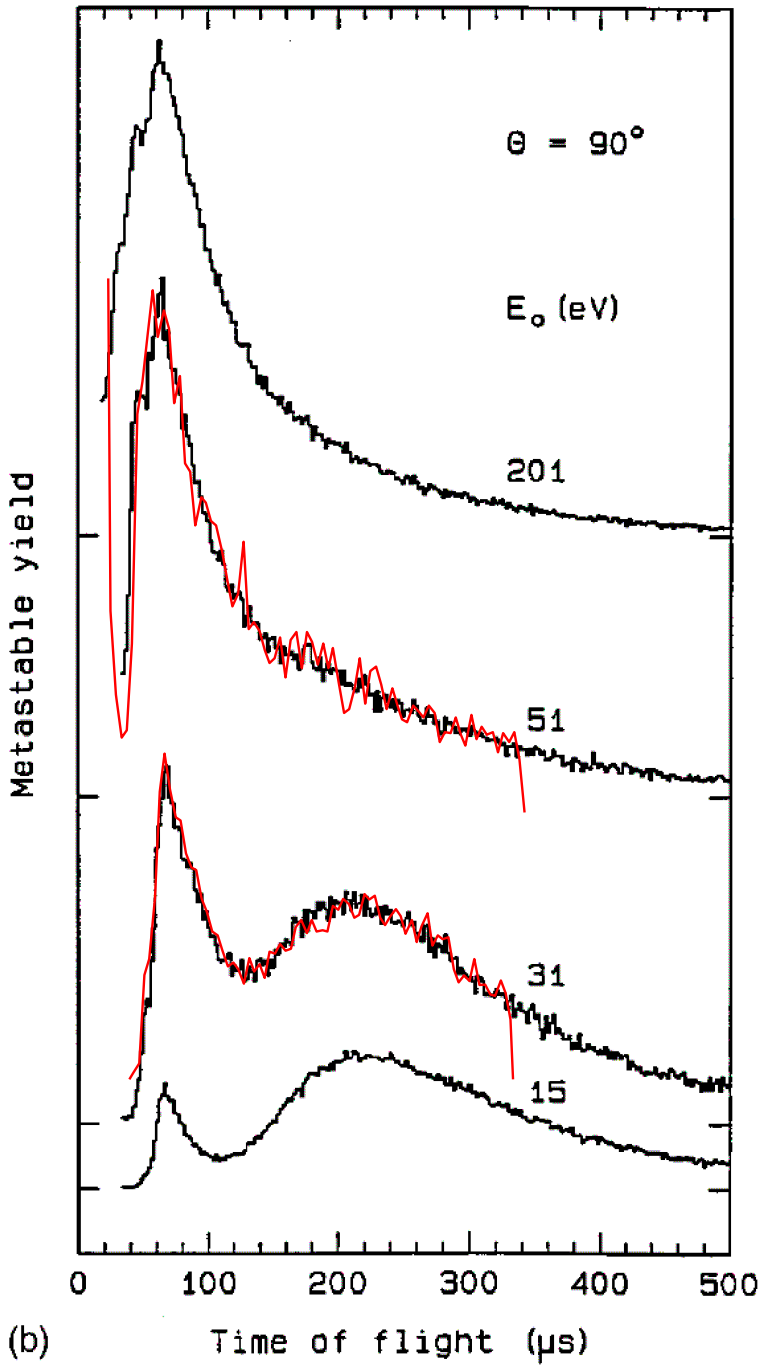

Figure 97: Neutral metastable TOF spectra by van der Burgt *et al.*[5] Red line –spectra obtained in this work overlaid for comparison of shape.

5.13 Methanol Mass Spectra and Excitation Functions

5.13.1 Mass Spectra

The methanol clusters shown in this section were formed from a reservoir at room temperature, without any carrier gas. The scans, shown in figures 102 and 103, were produced for a valve operating at 4Hz and an incident energy of 100eV.

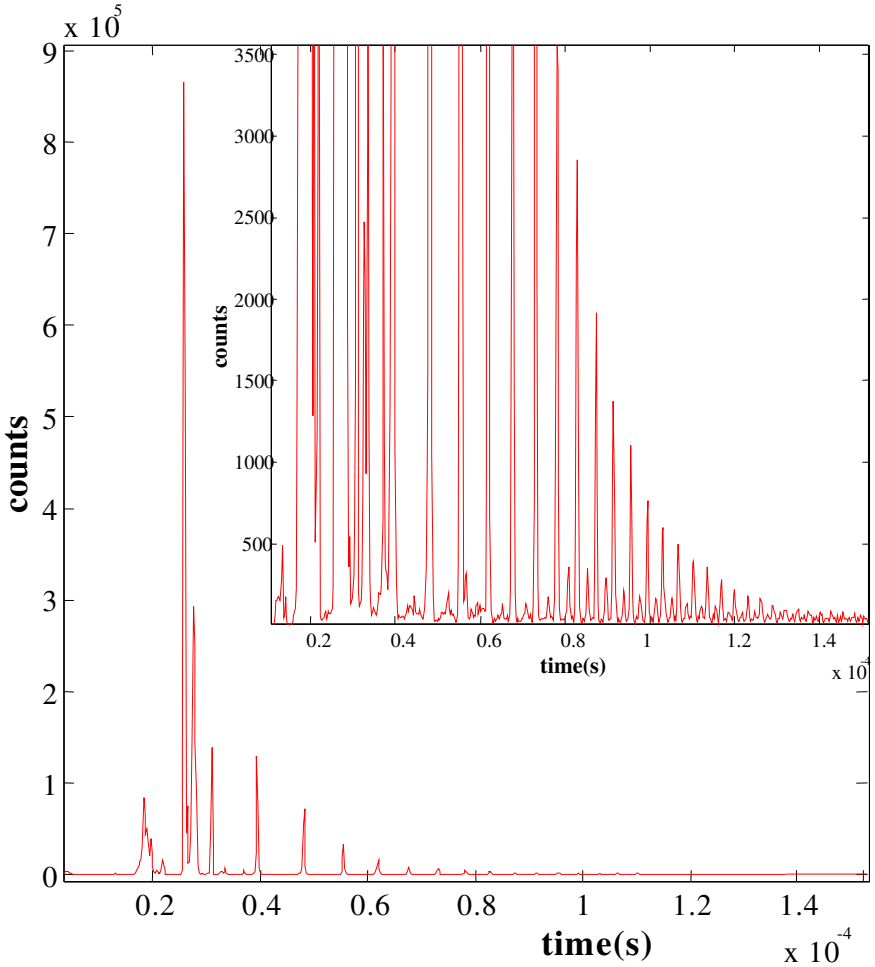

Figure 98: Mass spectrum of methanol vapor, at room temperature, without a carrier gas. Inset is an enlargement of the protonated clusters, about the 80μs mark a second series is evident.

Beside the dominant nitrogen peak (largest peak) is the methanol ion peak, and next to that is a peak corresponding to some argon still in the system.

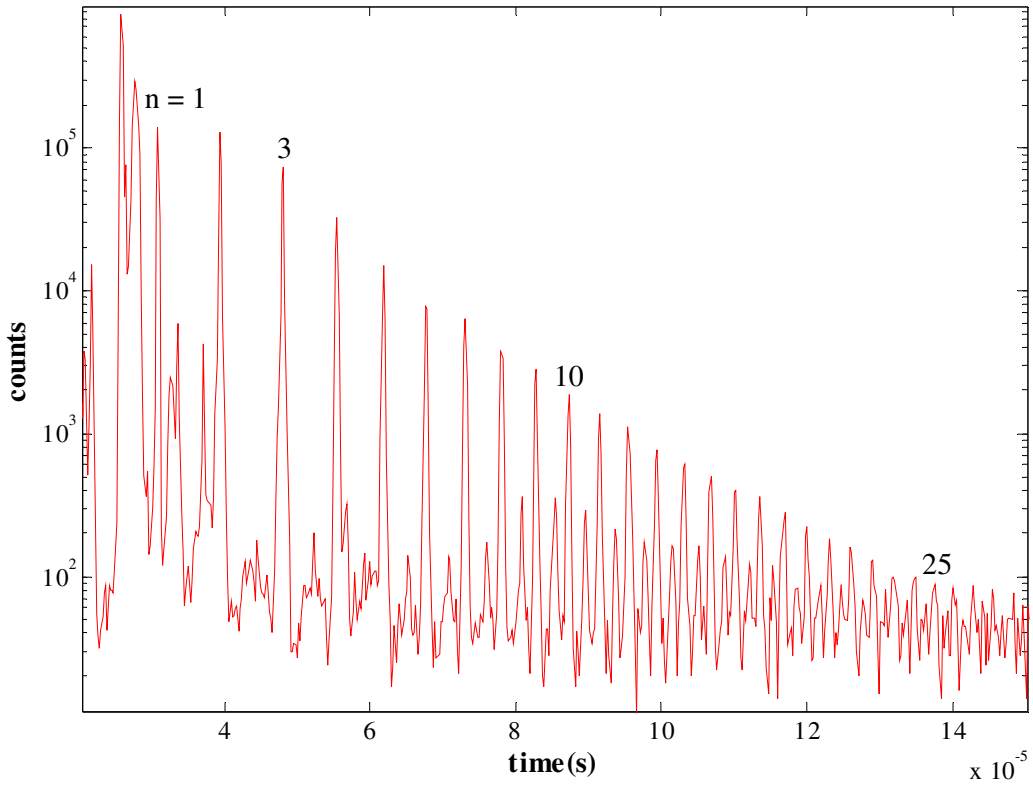

Figure 99: Enlarged logarithmic portion of figure 102. Protonated methanol clusters up to n=28 are observable in the major series. The minor series is that of hydrated clusters.

From the two figures can be seen two series, the larger one is that of protonated clusters $(CH_3OH)_nH^+$ in agreement with the work conducted and discussed in chapter 1. Also in agreement is the smaller series that is evident in the middle-right of figure 99. This corresponds to hydrated protonated methanol clusters $(CH_3OH)_n(H_2O)H^+$. These are known to occur only above $n = 7$.

Two graphs are included that support the larger series being protonated methanol clusters, figure 100, and the smaller series being hydrated protonated clusters, figure 101. In each graph the mass corresponding to the peaks in the series was plotted against n under the assumption being tested, that of the aforementioned products being responsible.

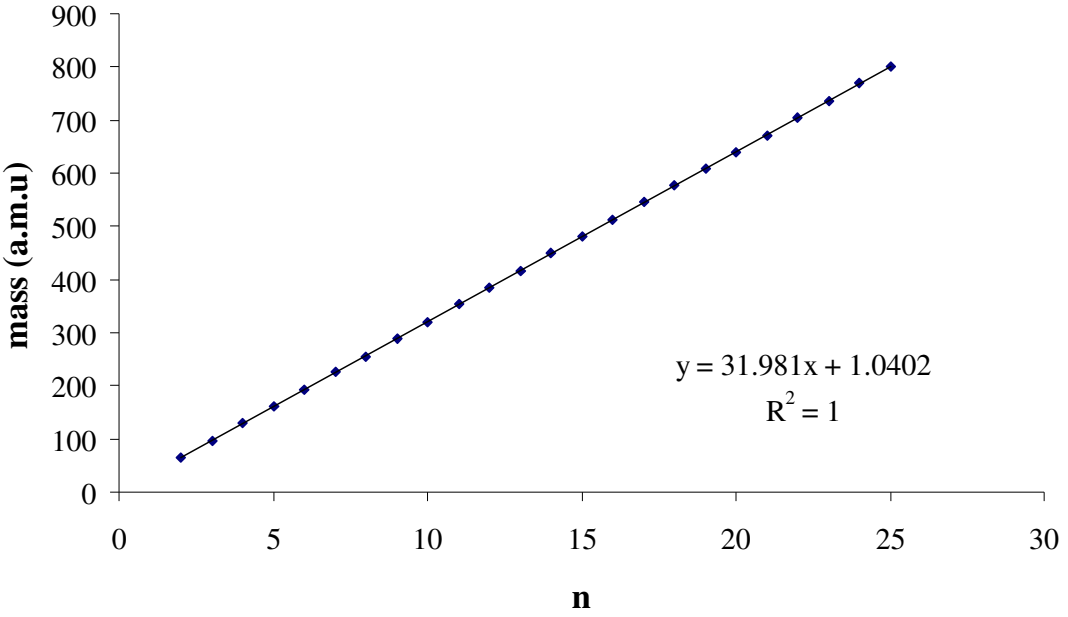

Figure 100: Plot of mass, of major series peaks in figure 102, against proposed n corresponding to the species $(CH_3OH)_nH^+$.

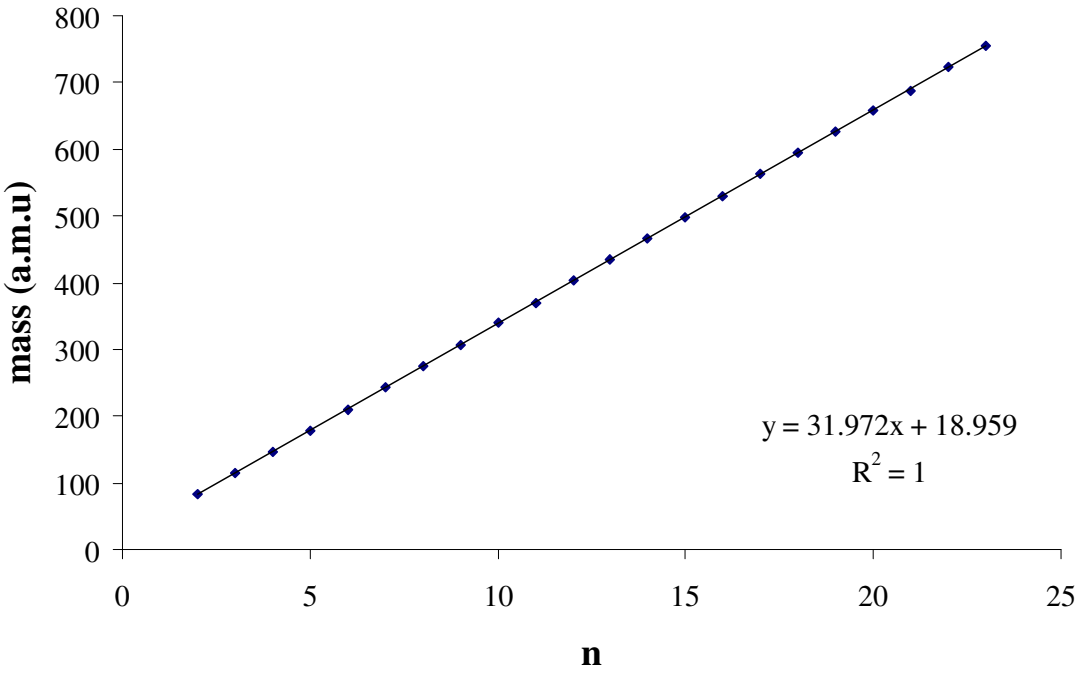

Figure 101: Plot of mass, of minor series peaks in figure 98, against proposed n corresponding to the species $(CH_3OH)_n (H_2O) H^+$.

For the protonated series $(CH_3OH)_nH^+$ we get a slope of 31.98 ± 0.02u, corresponding to the methanol clusters, and an intercept of 1.04 ±. 32, that corresponds to the attached hydrogen ion.

For the hydrated protonated series $(CH_3OH)_n(H_2O)H^+$ we get a slope of 31.97 ± .04, again corresponding to the mass of methanol, and a slope intercept this time of 18.96 ± .49, clearly the mass of a water molecule plus an additional hydrogen.

The mass spectra obtained display good cluster formation. With better pumping down and evaporation of the inlet valve, as well as an improved method for inputting methanol into the system even better spectra could be produced. The objective of the above tests is merely to show that the system is now functional, and I believe they display this. In the end much depends on the operating conditions of the nozzle and valve, which have proven very difficult to setup correctly, yet now appear to work quite well.

5.13.2 Excitation Functions

The excitation functions below in figure 102 and figure 103, were obtained for methanol vapour held in a reservoir at room temperature. Scans were taken from 10 to 130 eV in steps of 3 eV and with each scan taking 3000 sweeps. Two cycles were run through at 5Hz repetition rate pulsing condition. The source was contaminated with air so the excitation function of doubly ionised methanol has been omitted.

The appearance potential for singly ionised methanol via electron impact is 10.5eV,[6] and this seems to be in agreement with the onset region observed in figure 102.

In figure 103, for protonated methanol clusters up to $n = 4$, an expected decrease in the appearance potential with increased cluster size is also slightly discernible. Due to the instability of the gun at energies below 20 eV the excitation functions perhaps appear more similar in shape than is the actual case.

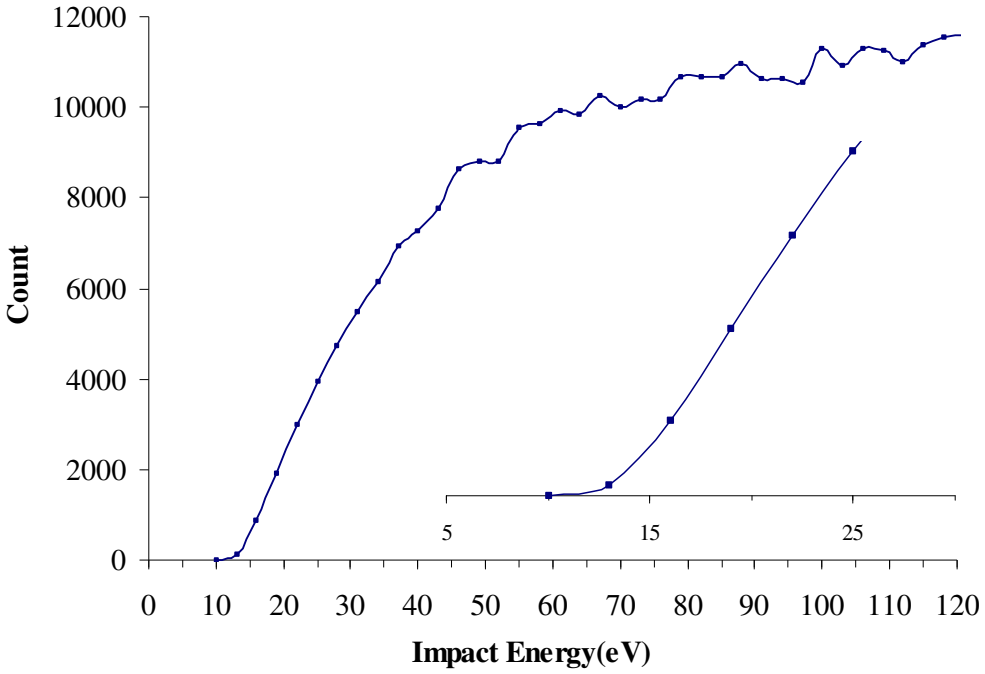

Figure 102: Excitation function of singly ionised methanol, CH_3OH^+, produced via electron impact. Inset – enlarged onset region.

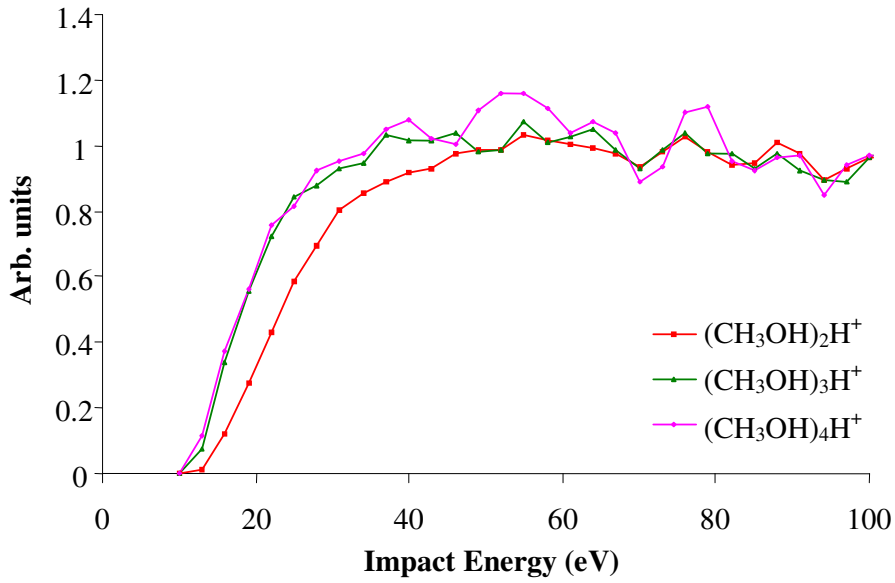

Figure 103: Excitation function of singly ionised protonated methanol clusters for n = 2, 3, 4, produced via electron impact.

5.14 References

[1] J. Lynch, *M. Sc. Thesis,* (2001) N.U.I. Maynooth

[2] W. Miehle, O. Kandler, T. Leisner, *J. Chem. Phys.* **91** (1989) 5940

[3] I. Torres, R. Martinez, M. N. Sanchez Rayo and F. Castaño, *J. Phys. B.* **33** (2000) 3615

[4] S. L. Carter and H. P. Kelly, *J. Phys. B: Atom. Molec. Phys.,* **9** (1976) L565

[5] P. J. M. van der Burgt and J. W. McConkey, *J. Chem. Phys.,* **102** (1995) 8414

[6] G. Vikor and M. V. Kurepa, *J. Serb. Chem. Soc.* **61** (1996) 437

CHAPTER 6

Conclusion

The work described in this thesis involved the development of an apparatus for the study of electron impact fragmentation of molecular clusters, at the National University of Ireland Maynooth. Work included the implementation and development of an operational cluster source, the design, construction, implementation and validation of a neutral metastable detector, enhancement of the electron gun by the implementation of a deflection system, and a series of other tests, enhancements, and modifications to ensure the experiment is optimised. The work also involved the writing of several LabView programs, for controlling the electron impact energy, acquisition of data and excitation functions, and for fast analysis of the time-of-flight spectra recorded.

As part of the development of an operational cluster source two valve types were tested, a Series 9 solenoid valve from General Valve Corporation, and a Lasertechnics model LPV pulsed valve (section 3.2). For tests conducted using argon or methanol, very little clustering was observed from the Series 9 valve (section 5.9). Attempts were also made to generate water clusters at this stage without success. The LPV valve, however, produces a strong yield of both argon and methanol clusters (section 5.11 and 5.13). The nozzle of this valve was modified to include a 0.2 mm divergent nozzle from Agar Scientific; it is the smaller nozzle size that is believed to be largely responsible for the improved cluster production.

A neutral metastable detector was designed, constructed and implemented (section 3.6). The detector utilises a channeltron and is mounted in the interaction region, at 90 degrees to the electron beam and cluster beam, for the observation of neutral metastables produced in the low energy interaction of electrons with clusters. Tests using argon have resulted in the time-of-flight spectra shown in section 5.12. The shape of these spectra is in agreement with previous work and indicates that the detector is functional. Signal rates during the test were somewhat low, but this can be improved by optimising the settings and conditions of operation.

A deflection system was incorporated into the electron gun (section 3.4) to provide steering of the beam. The electron gun is mounted above, and at 90 degrees to the direction of the cluster beam. The deflection lens element, consisting of four orthogonal aluminium elements, allows two-dimensional steering of the beam. Tests of the electron gun are shown in section 5.6 with the electron gun showing good stability down to 20 eV. A future improvement could be provided by increasing the range over which the electron beam can be steered; at present its range is not enough to cross the entire width of the cluster beam.

Two LabVIEW computer programs were developed as part of this thesis, V_Inc_Cont and Scan_Acq.vi. V_Inc_Cont.vi provides a user interface for easy control of the electron impact energy (section 4.5.1). It does so by interfacing with a programmable power supply that provides the relevant voltage to the electron gun. Scan_Acq.vi consists of two "pages", each a program unto itself. *Page 1* was developed to replace the older data acquisition software, which was not very flexible, and to allow the user to take excitation functions (section 4.5.2). This program interfaces with the multi-channel scaler and is used to acquire a single time-of-flight scan, or to acquire time-of-flight spectra as a function of the electron impact energy for some time range, energy range, and initial set of conditions. It displays the time-of-flight spectrum in real time. This program works reasonably well and was used to compile the excitation functions, of argon and methanol, presented in section 5.11 and 5.13 respectively. Modifications are planned to improve the manner of saving the data - to provide a better safeguard should the acquisition fail during a measurement. *Page 2* is a simple program used for a quick analysis of a recorded spectrum. It displays the data, providing various plotting tools for enlargement of regions, zooming in and out, scaling, selection of peaks, and for conversion from time-of-flight to mass-to-charge. This is a useful program for swift identification of peaks.

As a result of the work conducted as part of this thesis, we now have a fully operational cluster source at the National University of Ireland Maynooth, which produces very nice mass spectra. We also have a functional neutral metastable detector from which early time-of-flight scans show promising results. The system has been further improved and optimised by modifications and implementations, such as the electron gun deflection

system. Computer programs have been written for control of the electron gun, data acquisition, taking excitation functions, and analysis. All in all the work conducted has achieved its goals and the apparatus is now much closer to being ready to study the effects of low energy electron impact fragmentation of molecular clusters.

The long-term objective of the work conducted here at the National University of Ireland Maynooth is the development of an experiment that will allow us to solvate biomolecules into water or methanol clusters, for subsequent low-energy electron impact studies. This experiment will consist of a cluster source, and oven for the evaporation of biomolecules into clusters, an electron gun for the low-energy interaction, and will employ the reflectron time-of-flight mass spectrometer to study the ions produced, and the metastable detector to observe neutral metastable fragments produced. Presently, an oven is being tested for the future evaporation of DNA bases into clusters. Other plans underway include the development of a magnetic field arrangement that allows the electron gun to go to lower energies, and the design of a more controlled system for feeding methanol, or another target species, into the pulsed valve without unnecessary contamination. Once these elements are in place and operational the apparatus will finally be in position to carry out some very exciting studies on the fragmentation channels that result from low energy electrons impacting on molecular clusters, on DNA bases, and on DNA bases solvated in water clusters.

APPENDIX A

Library Code for MCS

```
#include <userint.h>
#include “test.h”
#include <utility.h>
#include “lw7887.h”


static unsigned short int fifo0, fifo1, fifo2, fifo3;
static unsigned int base, base1, base2, base3, base4, base5, base6,
base7, base8, base9, base10;
static unsigned char creg, fcreg, fscreg


void cardreset()
{
creg = 0x00;
fcreg = 0xf0;
outportb(base3,fcreg);
outportb(base1,creg); /* /RES=0, OUT=0 */
creg = 0x10; outportb(base1,creg); /* /RES=1 */
}



void fiforeset()
{
fcreg = inportb(base3);
fsreg = inportb(base5);
fcreg &= 0x0f; outportb(base3,fcreg);
/* FFRES=0 */
fcreg |= 0x01; outportb(base3,fcreg);
/* FRCLK=1 */
fcreg &= 0xfe; outportb(base3,fcreg);
/* FRCLK=0 */
fcreg |= 0x01; outportb(base3,fcreg);
/* FRCLK=1 */
fcreg &= 0xfe; outportb(base3,fcreg);
/* FRCLK=0 */
fcreg |= 0x01; outportb(base3,fcreg);
/* FRCLK=1 */
fcreg &= 0xfe; outportb(base3,fcreg);
/* FRCLK=0 */
fcreg |= 0x01; outportb(base3,fcreg);
/* FRCLK=1 */
fcreg &= 0xfe; outportb(base3,fcreg);
/* FRCLK=0 */
fifo0 = inport(base);
fifo1 = inport(base2);
fifo2 = inport(base4);
fifo3 = inport(base6);
fifo0 = inport(base);
fifo1 = inport(base2);
fifo2 = inport(base4);
fifo3 = inport(base6);
fifo0 = inport(base);
fifo1 = inport(base2);
fifo2 = inport(base4);
fifo3 = inport(base6);
```

```
fifo0 = inport(base);
fifo1 = inport(base2);
fifo2 = inport(base4);
fifo3 = inport(base6);
fcreg |= 0xf0; outportb(base3,fcreg);
/* /FFRES=1 */
fsreg = inportb(base5);
/* printf("%02X ",fsreg); */
fcreg |= 0x01; outportb(base3,fcreg);
/* FRCLK=1 */
fcreg &= 0xfe; outportb(base3,fcreg);
/* FRCLK=0 */
fcreg |= 0x01; outportb(base3,fcreg);
/* FRCLK=1 */
fcreg &= 0xfe; outportb(base3,fcreg);
/* FRCLK=0 */
fsreg = inportb(base5);
/* printf("%02X\n",fsreg); */
}


int testcard() /* test card to check if it is present and OK */
{
unsigned int itest;
int i,k;
creg = inportb(base1);
creg &= 0xfb; /* STARTI=0 */
fcreg = inportb(base3);
fsreg = inportb(base5);
fcreg |= 0x02; outportb(base3,fcreg); /* SETA=1 */
outport(base8, 0xA5A8);
outport(base10, 0xBBBB); /* P=BBBBA5A8 */
itest = inport(base8) & 0xFFF8;
if(itest != 0xA5A8)return FALSE;
fcreg |= 0x08; outportb(base3,fcreg); /* SEV=1 */
creg |= 0x08; outportb(base1,creg); /* ENA=1 */
creg |= 0x02; outportb(base1,creg); /* ENDR=1 */
creg |= 0x04; outportb(base1,creg); /* STARTI */
creg &= 0xfb;
/* FS */
for (k=0; k<1024; k++) {
for (i=0; i<4; i++) {
fsreg = inportb(base5);
if(fsreg & 0x40)break;
fifo3 = inport(base10);
}
if(fsreg & 0x40) {
fifo3 = inport(base6);
fifo2 = inport(base4);
fifo1 = inport(base2);
fifo0 = inport(base);
if (fifo3 != 0xBBBB) return FALSE;
if (fifo2 != itest) { /* may be new firmware version */
if (fifo2==0xA5A9 && itest==0xA5A8) itest++;
else return FALSE;
}
if (fifo1 != 0xAAAA) return FALSE;
if (fifo0 != 0xAAAA) return FALSE;
}
else {
return FALSE; /* printf("geht nicht! (OR == 0)\n"); */
}
itest++;
}
return TRUE;
}
```

```
int lw7886_init(unsigned int newbase)
{
base = newbase;
base1 = base+1;
base2 = base+2;
base3 = base+3;
base4 = base+4;
base5 = base+5;
base6 = base+6;
base8 = base+8;
base10 = base+10;
cardreset();
creg = inportb(base1);
fcreg = inportb(base3);
fsreg = inportb(base5);
if (!(creg & 0x04)) return FALSE;
/* OFF != 1 -> no 7886 found! */
creg = (creg & 0xfb); /* STARTI=0 */
fiforeset();
if (!testcard()) return FALSE;
cardreset();
fiforeset();
return TRUE;
}



int lw7886_acq(unsigned int *buffer, int range, in sweeps, double
timeout)

{
      int hitim;
      unsigned int I;
      int amount;
      int range5;
      int counter=0;
      double starttime;
      unsigned int preset;

creg = inportb(base1);
creg = (creg & 0xfb); /* STARTI=0 */
fcreg = inportb(base3);
fsreg = inportb(base5);


starttime=Timer();

range &=0xffffff00;

range5=range>>5;

preset=(unsigned)-range5;


fiforeset();

creg &= 0xfe; outportb(base1,creg); /* runs("mode=0"); */
creg &= 0xfd; outportb(base1,creg); /* runs("endr=0"); */
outpw (base8, (preset & 0x0000fff8)|0x3);
outpw (base10, (preset & 0xffff0000)>>16);
creg &= 0xf7; outportb(base1,creg); /* runs("ena=0"); */
creg |= 0x02; outportb(base1,creg); /* runs("endr=1"); */
creg |= 0x08; outportb(base1,creg); /* runs("ena=1"); */

for(;;) { /*Dummy read until output ready*/

      if(inpw(base8)& 0x02){

            while(inp(base5)&0x40){
```

```
            fifo3=inpw(base6);
            fifo2=inpw(base4);
            fifo1=inpw(base2);
            fifo0=inpw(base);

            hitim=(fifo0+fifo3*65536-preset)<<5;

          if (fifo0 & 0x01) ss[hitim]++;
          if (fifo0 & 0x02) ss[1+hitim]++;
          if (fifo0 & 0x04) ss[2+hitim]++;
          if (fifo0 & 0x08) ss[3+hitim]++;
          if (fifo0 & 0x10) ss[4+hitim]++;
          if (fifo0 & 0x20) ss[5+hitim]++;
          if (fifo0 & 0x40) ss[6+hitim]++;
          if (fifo0 & 0x80) ss[7+hitim]++;
          if (fifo0 & 0x0100) ss[8+hitim]++;
          if (fifo0 & 0x0200) ss[9+hitim]++;
          if (fifo0 & 0x0400) ss[10+hitim]++;
          if (fifo0 & 0x0800) ss[11+hitim]++;
          if (fifo0 & 0x1000) ss[12+hitim]++;
          if (fifo0 & 0x2000) ss[13+hitim]++;
          if (fifo0 & 0x4000) ss[14+hitim]++;
          if (fifo0 & 0x8000) ss[15+hitim]++;
          if (fifo1 & 0x01) ss[16+hitim]++;
          if (fifo1 & 0x02) ss[17+hitim]++;
          if (fifo1 & 0x04) ss[18+hitim]++;
          if (fifo1 & 0x08) ss[19+hitim]++;
          if (fifo1 & 0x10) ss[20+hitim]++;
          if (fifo1 & 0x20) ss[21+hitim]++;
          if (fifo1 & 0x40) ss[22+hitim]++;
          if (fifo1 & 0x80) ss[23+hitim]++;
          if (fifo1 & 0x0100) ss[24+hitim]++;
          if (fifo1 & 0x0200) ss[25+hitim]++;
          if (fifo1 & 0x0400) ss[26+hitim]++;
          if (fifo1 & 0x0800) ss[27+hitim]++;
          if (fifo1 & 0x1000) ss[28+hitim]++;
          if (fifo1 & 0x2000) ss[29+hitim]++;
          if (fifo1 & 0x4000) ss[30+hitim]++;
          if (fifo1 & 0x8000) ss[31+hitim]++;


      }

      outpw(base8,inpw(base8)|0x02);

      counter++;
}

      if (counter==sweeps)
            return counter;
                  if(Timer()-starttimer>timeout)
                        return counter;
}
}
```

APPENDIX B

LabVIEW Block Diagram "Scan_Acq.vi"

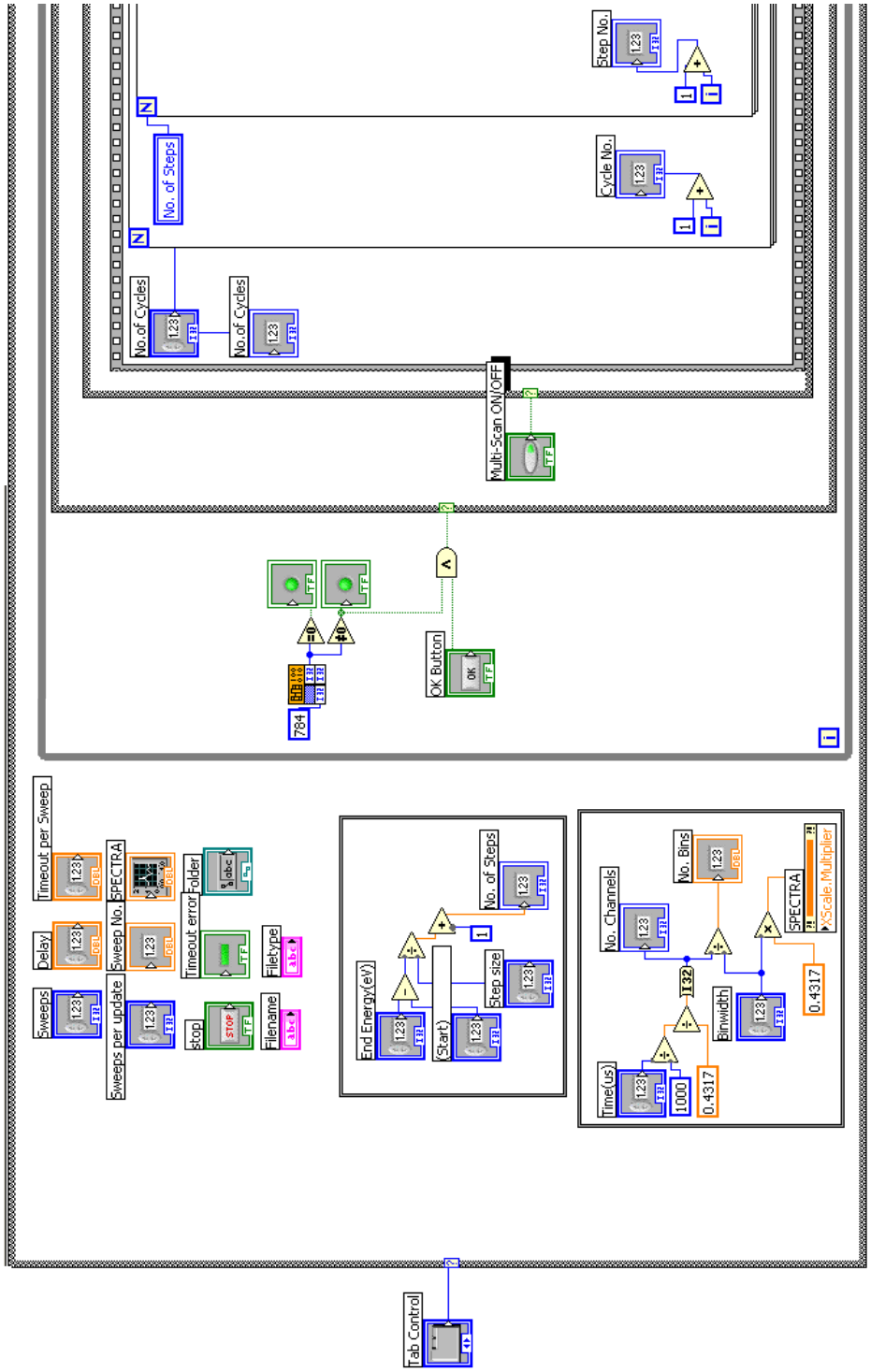

Figure B1: "Scan_Acq"-Page 1, block diagram part 1

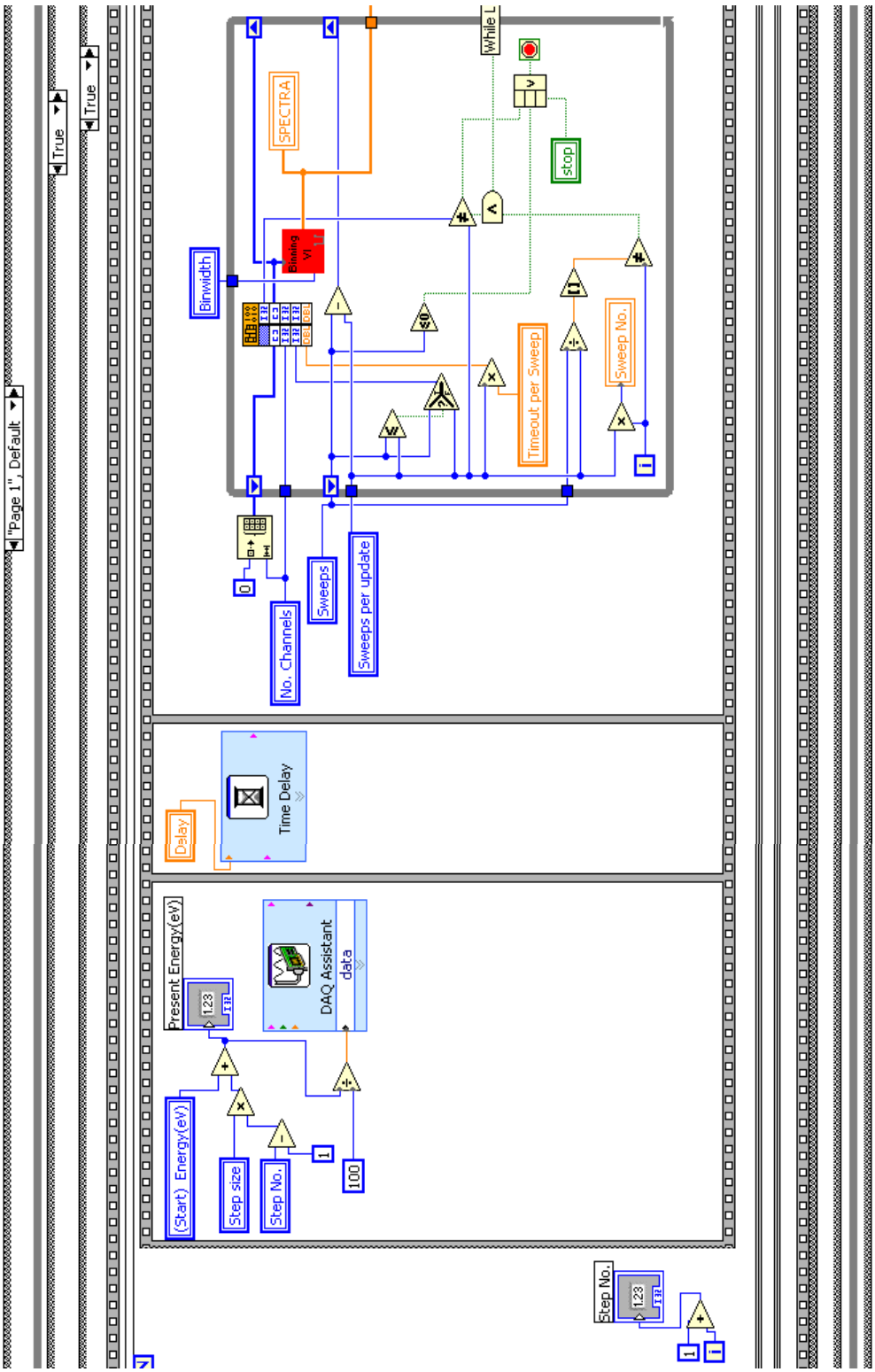

Figure B1: "Scan_Acq"-Page 1, block diagram part 2

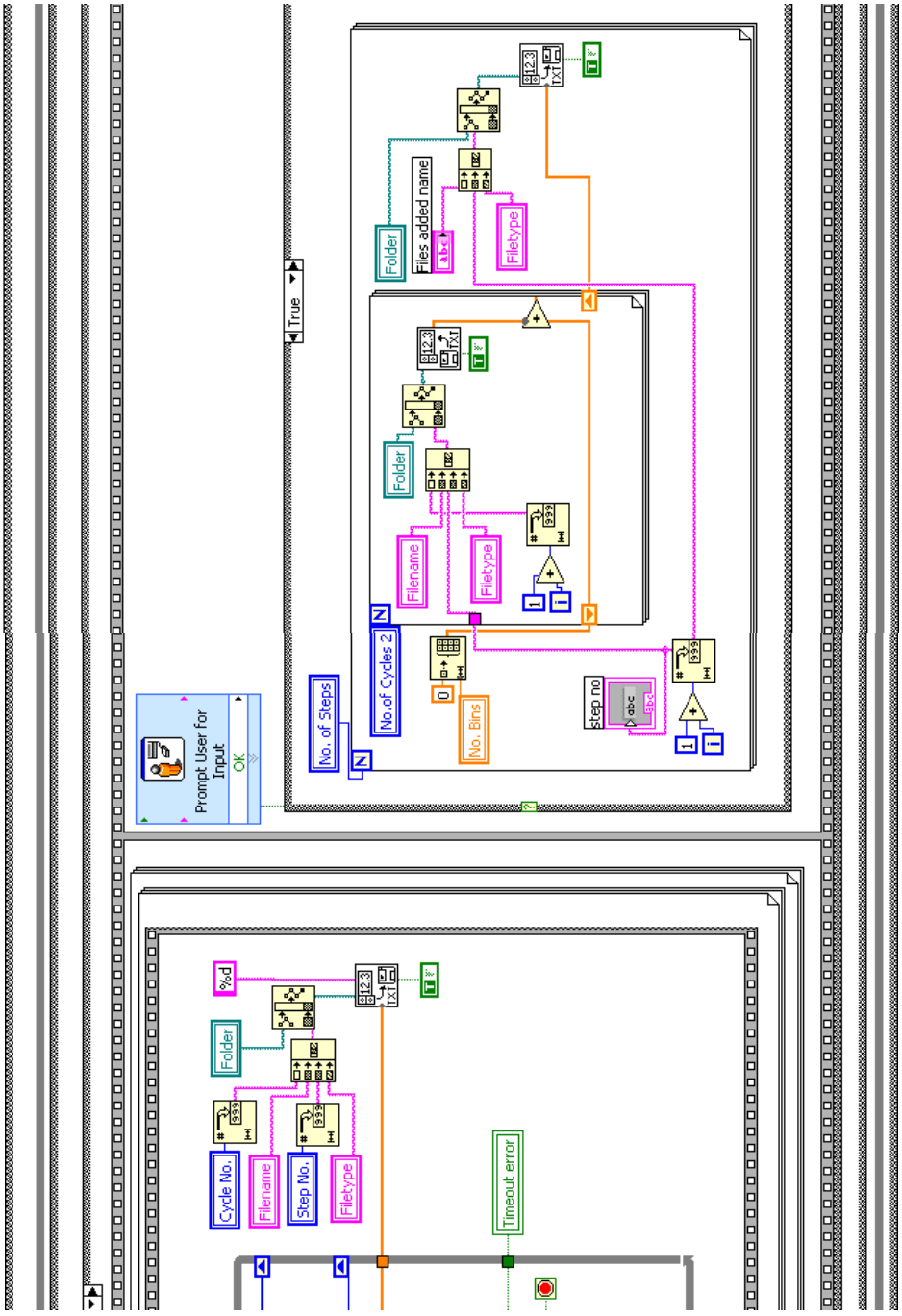

Figure B1: "Scan_Acq"-Page 1, block diagram part 3

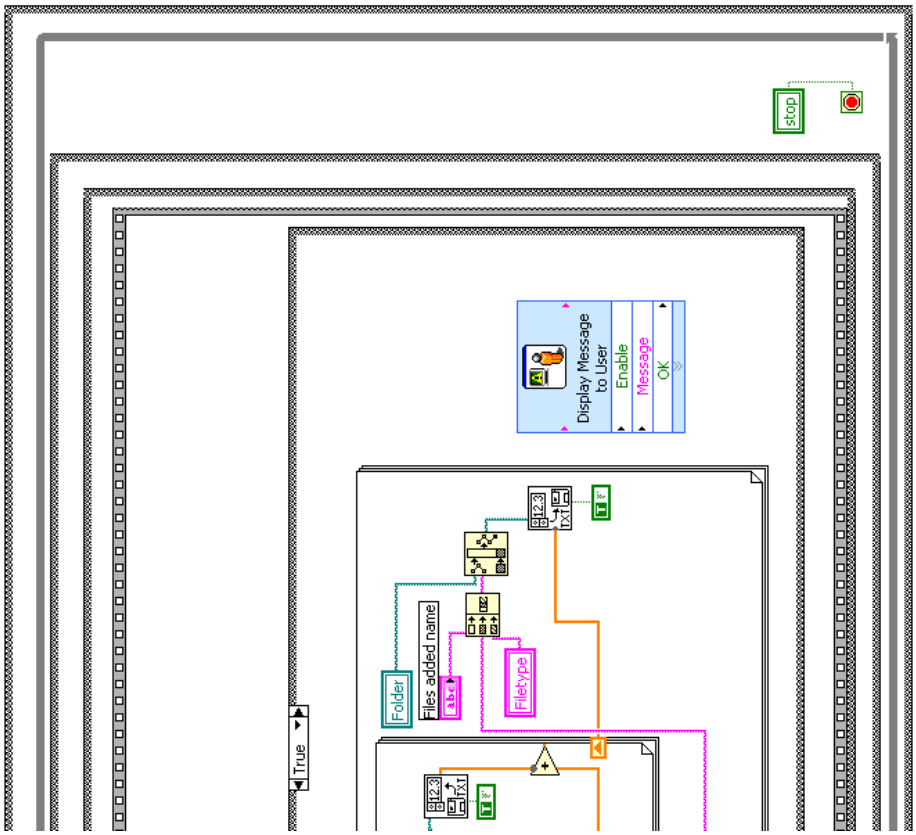

Figure B1: "Scan_Acq"-Page 1, block diagram part 4

APPENDIX C

LabVIEW Block Diagram "Binning.vi"

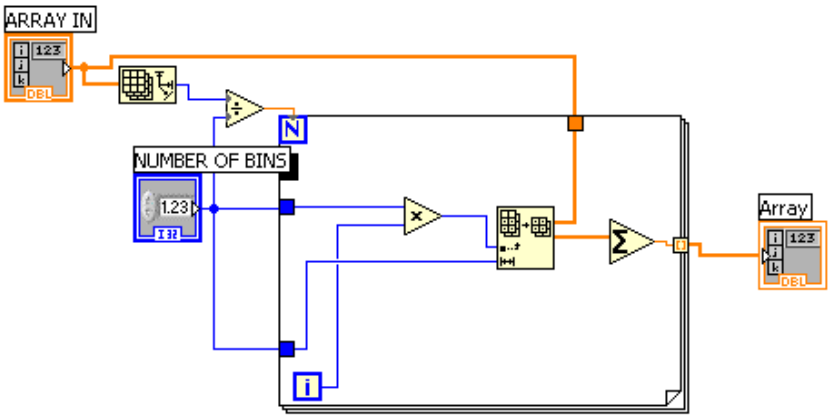

Figure C1: LabVIEW block diagram of SubVI "binning.vi"

APPENDIX D

Matlab Code

Cont16.m

```
function cont16(data)         %outputs concatenated data

close all   %closes any opened images

k=input('concatenate by(powers of 2)??'); %power of concatenation

binwidth=input('what is binwidth of spectrum?');

%requests binwidth used on acquisition

N=length(data);
binlength=(.4317*10^-9)*binwidth; %time length per data element
t=0:binlength:(N-1)*binlength;  %sets time elements of the data
n=(N/k);
squash =zeros(n,1); %initiates array to hold concatonated data

for y=1:(k/2)           %concatenation of first element in squash
    squash(1,1)= squash(1,1)+data(y,1);
end

for i=k+1:k:N   %concatenates remaining elements for squash
    s=(i-1+k)/k;
      for j=0:k-1
           squash(s,1)= squash(s,1)+data(i-(k/2)+j,1);
      end
end

L=length(squash);
binlength2=binlength*k; %establish the time elements for squash data
t2=0:binlength2:(L-1)*binlength2;
temp=data(200:N,1);
maxval=max(temp)+(max(temp)/10);    %used to plot suitably
temp2=squash(20:L,1);
maxval2=max(temp2)+(max(temp2)/10);

 figure;          %plot unconcatenated and concatenated data
subplot(2,1,1), plot(t,data)
hold on
axis([0 200*10^-6 0 maxval])
%grid on
%title(R)
xlabel('time(us)')
ylabel('count')

subplot(2,1,2), plot(t2,squash,'r-')
hold on
axis([0 200*10^-6 0 maxval2])
%grid on
%title(P)
ylabel('counts')
```

```
xlabel('time(us)')

figure;
semilogy(t2,squash)


c=input('no of sum regions?');  %sums over regions or peaks
mint = [];
maxt = [];
sumreg = [];
for v=1:c,  %range of regions to be summed over
v
mint(v)=input('start count sum region(*10^-5)? = ');
maxt(v)=input('finish count sum region(*10^-5)? = ');
end

for g=1:c   %performs the integrations
u=ceil((mint(g)*10^-5)/(k*binlength));
v=ceil((maxt(g)*10^-5)/(k*binlength));
data_count(g)=sum(squash(u:v));
end


disp('The region sums are:')
disp(data_count)

 find_peaks(squash, binlength2);  % call to find peaks


% END OF M-FILE
```

Find_peaks.m

```
function find_peaks(data, binlength2); %finds peak locations

threshold = input('Specify Threshold: '); % peak search above this

peaks = diff(data); %differentiate data finds peaks from this
%figure;
%plot(peaks)
%hold on
array_peaks = [];

N=length(peaks);
for i=1:N-1,        %looks for where gradient is zero and above
threshold
    if ( peaks(i)>0 & peaks(i+1)<0 )& ( data(i+1) > threshold)
                                array_peaks = [array_peaks i+1];
    end
end

N_data=length(data);
t=0:binlength2:(N_data-1)*binlength2;
size(t);
size(data);

figure;
plot(t, data, 'k');
hold on

N2=length(array_peaks);

for i=1:N2,             %plots a symbol on top of where peak is
    ind = array_peaks(i);
    plot(t(ind), data(ind), 'ro');
end

figure;
semilogy(t,data, 'k');
hold on

for i=1:N2,
    ind = array_peaks(i);
    semilogy(t(ind), data(ind), 'ro');
end

disp('The Peak Values are: ') %displays the peak values
disp(t(array_peaks))

peak_time=(1*t(array_peaks));  %calib factor to equate theor & expt.

%comptime(peak_time); %call to alternative theoretical function motof
                     to calculate mass/q values
massperq(peak_time);    %call to empirical equation to calculate
mass/q values
```

Massperq.m

```
function [masstocharge] = massperq(time) %calculate the mass to charge
                                          ratios
 p=length(time);
masstocharge=[];

for i=1:p
    mass=.0404*((time(i)*1000000)^2.0093);
      masstocharge(i)=mass;
end

masstocharge;

disp('Evident Mass to charge ratio peaks at')
disp(masstocharge)

end
```